

Coherence as a Measure of Body-Wave Signal to Noise Ratio in the Northeastern United States and Southeastern Canada

Ian Philip Cooper

A thesis submitted to the Faculty of
the department of Earth and Environmental Sciences
in partial fulfillment
of the requirements for the degree of
Master of Science

Boston College
Morrissey College of Arts and Sciences
Graduate School

August 2021

Coherence as a Measure of Body-Wave Signal to Noise Ratio in the Northeastern United States and Southeastern Canada

Ian Philip Cooper

Advisor: John E. Ebel, Ph.D.

Determination of the source parameters of a local earthquake from full seismic waveforms requires seismograms with clear body-wave signals from the earthquake source. Coherence of the earthquake body-wave seismograms recorded at two different receivers can be used to estimate the signal-to-noise ratio (SNR) of the body-wave energy radiated by the source. In this study, the coherence of earthquake body waves recorded in the Northeastern United States and Southeastern Canada (NEUSSEC) is measured as a function of frequency, interstation distance, and ambient SNR, and then used as an estimate of body-wave SNR. Seismograms from the CN, IU, LD, N4, NE, TA, and US arrays were used to measure coherence between stations with a mean separation of 70 km. Seismograms from the Acton Littleton Seismic Array (ALSA) were used to measure coherence at 5 km mean station separation. Coherence is measured at frequencies between 0.05-10 Hz for Pn and Sn phases from NEUSSEC earthquakes with magnitudes (M) between 0.0 and 4.7 at epicentral distances between 180-1800 km as well as at frequencies between 0.05-10 Hz for the first arrivals of P and S waves from earthquakes $M > 6$ at distances > 2500 km. The teleseismic P waves display values of coherence greater than 0.9 out to interstation distances of 1500 km at frequencies < 0.8 Hz, but as frequency increases, the interstation distance at which coherence falls below 0.9 decreases. Teleseismic S and regional Pn and Sn waves display coherence values around 0.5, suggesting the amplitudes of the body-waves are smaller than those of the noise, which likely is the result of converted and reflected or refracted P waves and/or smaller signal amplitudes. These coherence values are compared to the coherence values of ambient noise. For any two P, S, Pn or Sn waveforms recorded in the NEUSSEC at 3-5 Hz there is a 50% or greater chance of those two waveforms containing coherent energy that is not ambient noise; these frequencies are where this percent chance is greatest for all seismic phases. At frequencies between 3-5 Hz the effects of scattering are most pronounced on the coherence values of regional seismic phases, suggesting that most scattering in the crust of the NEUSSEC takes place at these frequencies. Teleseismic seismic phases do not include as much scattered energy as the regional seismic phases at 3-5 Hz, and must therefore encounter fewer scattering heterogeneities along their travel path than the regional seismic phases.

TABLE OF CONTENTS

Table of Contents.....	iv
List of Figures.....	v
List of Tables.....	vii
Acknowledgements	viii
Introduction.....	1
Body-Wave Signal and Noise.....	3
Coherence as a Proxy for SNR.....	8
Data and Methods.....	13
Results	29
Discussion	38
Conclusions	42
References	43
Figures.....	45
Tables.....	71

LIST OF FIGURES

- Figure 1. Power Spectrum of Vertical Noise
- Figure 2. Map of Study Region and Regional and Local Array Stations
- Figure 3. Body-Wave Windowing of a Seismogram
- Figure 4. TX Diagram
- Figure 5. Normalized Crosscorrelation
- Figure 6. Expected Coherence Value Methodology
- Figure 7. Coherence of Teleseismic P Waves on the Regional Array
- Figure 8. Coherence of Teleseismic S Waves on the Regional Array
- Figure 9. Coherence of Regional Pn Waves on the Regional Array
- Figure 10. Coherence of Regional Sn Waves on the Regional Array
- Figure 11. Coherence of Teleseismic P Waves on the ALSA
- Figure 12. Coherence of Teleseismic S Waves on the ALSA
- Figure 13. Coherence of Regional Pn Waves on the ALSA
- Figure 14. Coherence of Regional Sn Waves on the ALSA
- Figure 15. Coherence of Ambient Noise on the Regional Array
- Figure 16. Coherence of Ambient Noise on the ALSA
- Figure 17. Coherent Body-Wave Percentage Methodology
- Figure 18. CBPs of Teleseismic P Waves on the Regional Array

Figure 19. CBPs of Teleseismic S Waves on the Regional Array

Figure 20. CBPs of Regional Pn Waves on the Regional Array

Figure 21. CBPs of Regional Sn Waves on the Regional Array

Figure 22. CBPs of Teleseismic P Waves on the ALSA

Figure 23. CBPs of Teleseismic S Waves on the ALSA

Figure 24. CBPs of Regional Pn Waves on the ALSA

Figure 25. CBPs of Regional Sn Waves on the ALSA

Figure 26. CBPs versus Frequency and Ambient SNR

LIST OF TABLES

Table 1. Earthquake Signal Distance Limits from Atkinson [2004]

Table 2. Regional Array Stations

Table 3. ALSA Stations

Table 4. Regional Earthquakes Recorded by the Regional Array

Table 5. Teleseismic Earthquakes Recorded by the Regional Array

Table 6. Regional Earthquakes Recorded by the ALSA

Table 7. Teleseismic Earthquakes Recorded by the ALSA

ACKNOWLEDGEMENTS

I am thankful to the Department of Earth and Environmental Sciences at Boston College for providing financial support for this research and to the faculty of the same department for providing assistance and guidance throughout the project.

INTRODUCTION

Determining the signal-to-noise ratio (SNR) of seismograms across a region over different frequency bands for earthquakes of different magnitudes can demonstrate where the SNR is sufficiently high for the various methods of earthquake source parameter modeling [Dreger & Helmberger, 1990; Dahal & Ebel, 2019]. A body-wave SNR is typically calculated by splitting the waveform into two segments, one before and one after the arrival of the seismic phase (the presignal noise and the postsignal waveform of interest) and then taking the ratio of the peak postsignal amplitude over the peak presignal amplitude to get the signal-to-noise ratio (SNR) or

$$SNR = \frac{\max(A_{post})}{\max(A_{pre})} \quad (1)$$

where A_{post} is the average postsignal amplitude and A_{pre} is the average presignal amplitude. However, as body waves travel through the earth, they encounter velocity heterogeneities that cause scattering; this scattered energy arrives after the wavefront and is recorded by seismometers after the body-wave first arrival. These scattered energy arrivals are called coda waves or simply coda [Aki, 1969, Mack, 1969, Aki & Chouet, 1975].

The coda is not present in the presignal and is therefore not accounted for in calculations of SNR made using equation (1). This ratio method of calculating SNR only includes the ambient microseismic noise in its calculation. I therefore refer to it as the ambient SNR. What I refer to as just the SNR includes both the noise from ambient microseismic sources and the noise from scattered source energy. Methods exist for measuring the amount of energy that body waves lose to scattering and the packing density of heterogeneities present in the crust [*Aki*, 1973, *Aki & Chouet* 1975, *Langston*, 1989, *Hock et al.*, 2004], but these methods do not address the presence of scattered energy within body-wave recordings, which can interfere with the body-wave signals [*Mack*, 1969, *Ebel*, 1989].

In this thesis, I outline a method that describes the measurement of the SNR of earthquake body waves that includes scattered source energy as noise. I do this by assuming that body-wave signals from a given earthquake will be coherent between different recording stations, while both ambient and scattered noise will be incoherent between stations, therefore allowing me to use the coherence of a body wave recorded at two different stations as a proxy for the SNR. I present the coherence of P, S, Pn and Sn seismic phases as functions of frequency, interstation distance, and ambient SNR. I describe the method and present the results for the body-wave SNR calculated using coherence for a regional array covering the Northeastern United States and Southeastern Canada (NEUSSEC) (57°W to 83°W and 37°N to 50°N) and a smaller, local array covering approximately 50 km² within that regional array.

BODY-WAVE SIGNAL AND NOISE

What is referred to as noise in this thesis has two main causes: (1) random scattering of earthquake source energy not explained by major crustal and mantle boundaries, called in this thesis “scattered noise”; and (2) energy from microseismic sources other than the earthquake that generate seismic waves, called in this thesis “ambient noise.” The amplitudes of the seismic waves, of both the body-wave signal and of these two types of noise, can vary with frequency, earthquake magnitude, source-receiver distance, receiver location and time.

The strengths of body waves, scattered noise and ambient noise are all dependent on frequency. Earthquakes release energy across all frequencies, but most of the body-wave energy from earthquakes of all magnitudes is detected with the largest ground motions at frequencies below 10 Hz [*Brune, 1970, Aki, 1967*], thus making the amplitudes of body waves dependent on frequency. Scattered noise is energy that was originally emitted by a source (in this thesis, the earthquake of interest) and encounters a velocity heterogeneity between the source and the receiver at which it is recorded. The velocity heterogeneity can generate new, secondary waves (scattered energy) upon incidence of the primary wave from the original source by processes such as reflection, refraction, and P or S conversions [*Aki, 1967, Stein & Wysession, 2003*]. The scattered noise will therefore contain only frequencies originally present in the source energy.

The interaction of the energy being scattered by the heterogeneity is dependent on the frequency of the incident energy because the greatest scattering occurs when the sizes of the heterogeneities are similar to or larger than the wavelengths of the incident energy; given the sizes of the heterogeneities in the crust, most energy with wavelengths greater than tens of kilometers, or frequencies below roughly 1 Hz, does not undergo significant scattering and does not appear as scattered noise [Vernon et al., 1998, Stein & Wysession, 2003]. This effect that the size of the heterogeneities has and the fact that scattered energy was originally source energy before undergoing any scattering makes the amplitude of scattered noise recorded dependent on frequency. Ambient microseismic noise originates from sources other than the earthquake of interest and may include energy from other earthquakes, wind, ocean tides, atmospheric pressure and temperature changes and anthropogenic sources such as vehicles on roads [Gutenberg, 1936, Stein & Wysession, 2003]. This ambient noise is strongest at frequencies ranging between 0.1-0.2 Hz where it is mostly thought to originate from ocean waves; the strength of this noise generated by ocean waves can be great enough that it becomes difficult to record small earthquake signals at these low frequencies [Gutenberg, 1936, Stein & Wysession, 2003]. Figure 1 displays the ambient noise spectra from a station within the NEUSSEC, and similar amplitudes were seen in previous studies [Powell, 1992, Stein & Wysession, 2003]

The strength of earthquake body-wave signals and scattered noise also depends on the source magnitude. The larger the magnitude of an earthquake, the more energy is emitted across all frequencies, resulting in greater signal amplitudes at all frequencies [Aki, 1967, Stein & Wysession, 2003]. However, the increase in energy released with

increased magnitude is not uniform across all frequencies, and as the strength of a seismic source increases, the most significant increase in energy released is at frequencies below 0.1 Hz [Aki, 1967]. Ambient noise is, of course, independent of the earthquake source magnitude because that noise originates elsewhere, but the energy that becomes scattered noise does originate from the earthquake source. Therefore, if more energy is emitted by the earthquake source at a frequency associated with heterogeneities of a size that will result in that energy being scattered, then the amplitude of the scattered energy recorded at that frequency by a receiver will increase. Conversely, if less energy is emitted by the earthquake source at frequencies that undergo scattering, then the amplitude of the scattered energy recorded at those frequencies by a receiver will decrease.

The distance of the seismic station from the event, or the source-receiver distance, also affects the strength of the signal and the scattered noise. Seismic waves interact with the rocks that they travel through, which changes their time-domain waveshapes through various attenuation processes that include geometric spreading, anelastic attenuation, and dispersion, as well as through reflections, refractions and conversions [Stein & Wysession, 2003]. These attenuation processes all contribute to lowering the amplitudes of the energy as it travels through the earth [Stein & Wysession, 2003, Atkinson, 2004]. Energy at certain frequencies attenuates more than at other frequencies, and studies of earthquake wave attenuation have been able to describe the maximum distances at which different frequency energy is detectable from different magnitude sources [Atkinson, 2004]. Atkinson [2004] described how in the NEUSSEC earthquake body-wave signals

gradually reduced in amplitude with distance until becoming undetectable by regional seismic network instruments, as displayed in Table 1 (from Atkinson [2004] Table 1).

Ambient noise also undergoes the same attenuation processes that the signal does as it travels, but because ambient noise is the sum of recorded energy from many different sources, it is easier to consider the amplitude of the ambient noise as a function of location and time based on a receiver's proximity to and the intensity of microseismic sources at a given time. For example, the strength of microseismic noise coming from water movements in the oceans decreases the farther a receiver is from the coast, but a large tropical storm occurring at the time of recording would increase the energy of the microseismic source (the ocean waves) and thus increase the strength of the ambient noise produced by ocean waves [Gutenberg, 1936]. Differences in location of a receiver will also mean differences in the crust and upper mantle at that location which can affect the attenuation processes that seismic waves undergo as they travel, thus altering the energy's amplitudes when it ultimately arrives at a receiver. For example, the concentration and size of heterogeneities in the crust that lead to the scattering of seismic energy and the recording of scattered noise could vary across a region and lead to differences in the strength of scattered noise recorded at different receivers and frequencies as well as causing differences in the signal strength due to differences the amount of energy lost to scattering [Langston, 1989, Stein & Wysession, 2003, Hock et al., 2004].

Together, all of these effects determine the strengths of earthquake body-wave signals, scattered noise and ambient microseismic noise. In this thesis, I will be examining the different effects that the ambient noise and the scattered noise each have

on the earthquake body-wave SNR at different frequencies by measuring that SNR in a way that allows me to separate the two sources of noise.

COHERENCE AS A PROXY FOR SNR

Coherence is a measure of the similarity between two waveforms; the more coherent two waveforms are, the closer to identical they are in amplitude, phase and frequency content. In array seismology it is often assumed that body-wave signals do not change shape within the array, or if they change, the change is in a predictable manner [Mack, 1969, Rost & Thomas, 2002]. These changes can be modeled using a Green's Function which describes the effects of propagation from a source to a receiver where the source is described by a delta function in space and time; convolving an earthquake source time function with the correct Green's Function results in the seismogram that would be recorded by a station located relative to the source as described by the Green's Function [Saikia & Herrmann, 1985, Stein & Wysession, 2003]. For an event like an earthquake, where two receivers might have a small interstation distance relative to the wavelengths of the source energy, the source time functions and the Green's Functions for the wave propagation from the source to those two stations should be similar and thus should produce highly coherent body waves [Toksöz, 1991, Rost & Thomas, 2002]. In contrast, the scattered noise contained in earthquake seismograms has a random shape to it [Stein & Wysession, 2003], and this will result in incoherent noise waveforms at the two stations [Rost & Thomas, 2002]. Most sources of ambient noise such as from vehicles are also spatially and temporally random and would result in incoherent

waveforms at two different receivers, but there are some instances where ambient noise can produce coherent waveforms at two different receivers [*Campillo, 2006, Seydoux, et al., 2016*]. Ocean waves and swells for example, are capable of producing coherent ambient noise at frequencies between 0.09 and 0.2 Hz [*Seydoux, et al., 2016*], the same frequencies where noise is strongest in the NEUSSEC (Figure 1). Therefore, I assume that given two seismograms of the same seismic body-wave phase from the same earthquake, most of the coherent energy just following the first P and S arrivals will be body-wave energy and any incoherent energy will be energy from ambient and scattered noise. Some of that coherent energy may be the result of ambient noise, but an analysis of the coherence of ambient noise will allow me to determine the chance that a single coherence value is the result of coherent body-wave energy or just ambient noise. Thus, coherent waveforms that are not the result of coherent ambient noise should have high body-wave SNRs, while incoherent waveforms are the result of low body-wave SNRs.

As explained previously, the SNR is a function that varies depending on frequency, earthquake magnitude, source-receiver distance, location and time; for coherence to be used as a proxy for the SNR it must be proportional to the SNR. A change in one of those variables that brings about an increase in SNR by either strengthening the signal or weakening the noise, such as larger magnitudes, shorter source-receiver distances, and locations and times where the ambient noise is weaker, would also bring about an increase in the coherence. This is because these conditions cause an increase in the coherent energy of the signal and/or a decrease in the incoherent energy of the noise. The same is true for the opposite case where signal amplitudes are smaller and the noise amplitudes are larger. Coherence therefore increases when a

variable causes an increase in the SNR and coherence decreases when a variable causes a decrease in the SNR. Thus, the underlying principle for this study is that coherence can be used as a proxy for SNR.

Two waveforms, x and y , which are both earthquake body-wave recordings of the same seismic phase produced by the same earthquake and recorded at different locations should contain coherent energy in the form of the earthquake body waves and possibly some ambient noise and incoherent energy in the form of scattered and ambient noise. I therefore propose that the coherence of x and y , C_{xy} , is proportional to some unknown function, f of the SNR of waveforms x and y ,

$$C_{xy} \propto f(SNR(x), SNR(y)) \quad (2)$$

An increase in the SNR of waveform x would result in an increase in the coherence because a greater percentage of the energy present in waveform x would be coherent body-wave signal; if instead the SNR of waveform x decreased then the coherence would also decrease for the same reason. The same is also true of waveform y . If there were coherent ambient noise present in x and y , then C_{xy} would be greater than if there was only coherent body-wave energy, but an increase in the SNR of either waveform would still result in an increase in C_{xy} and a decrease in either SNR would also still result in a decrease in C_{xy} regardless of whether there is coherent ambient noise in the two waveforms.

Based on the formulation of the problem presented above, I describe the coherence of body waves recorded across the arrays used in this thesis as a function of three variables: frequency, interstation distance, and the ambient SNR, the measurement of which was defined by Equation (1). As mentioned earlier, it is assumed that where interstation distances are sufficiently small the difference in the source time functions and Green's Functions of the two receivers will be small. Examining how coherence changes with interstation distance will let me determine what effect a difference in travel path has on the coherence at different frequencies and the interstation distances out to which this assumption might be true at those different frequencies. The ambient SNR is easily measured using Equation (1), and an increase in the ambient SNR should bring about an increase in the coherence by reducing the presence of incoherent noise. Where ambient SNRs are sufficiently high the majority of noise present in a seismogram should be scattered noise instead of ambient noise, and therefore any incoherence should primarily be the result of scattered energy. This allows me to determine the effect of scattered noise on the SNR at different frequencies, independent of ambient noise.

In this thesis, the P, S, Pn and Sn earthquake body-wave phases recorded in the NEUSSEC are analyzed to determine their coherence as a function of frequency, interstation distance, and ambient SNR. This measurement of coherence is used as a proxy for the SNR of those waveforms. I describe the effect frequency has on coherence and therefore the SNR and what can be inferred about the strength of earthquake body-wave signals and noise at different frequencies in the region. By analyzing the effect that the ambient SNR has on coherence, I am also able to describe the strength of scattered

noise at different frequencies where the scattered energy results from body wave scattering off heterogeneities in the crust and upper mantle.

DATA AND METHODS

In this thesis, I use seismograms from two seismic arrays, one that covered the entire surface of the NEUSSEC and another that covered roughly 50 km² within the US state of Massachusetts (Figure 2); I refer to these two arrays as the “regional array” and the “local array”, respectively. The regional array is comprised of the 2013-2016 deployment of the Earthscope Transportable Array (TA) [*IRIS Transportable Array*, 2003] along with permanent stations throughout the region from the LD, NE, N4, CN, IU and US networks (Figure 2). The regional array consists of 305 stations, the largest contribution to that count (138 stations) comes from the TA, whose stations are distributed across the entire NEUSSEC (a maximum interstation distance of roughly 1500 km) with an average station spacing of approximately 70 km [*IRIS Transportable Array*, 2003]. All of these stations are listed in Table 2, along with their network, latitude, longitude, elevation, dates of operation and digitization rate. The local array is the Acton Littleton Seismic Array (ALSA), which consists of four temporary stations run by Boston College’s Weston Observatory and the IU HRV station, all of which are distributed in the Acton and Littleton, Massachusetts area (Figure 2). These stations represent the local array used in this study with interstation distances ranging from 2-10 km. The ALSA stations are listed in Table 3 with their latitudes, longitudes, elevations, dates of operation, and digitization rates.

The seismograms I use in this study were produced by two types of earthquake sources, ones that originate within the study region, which I refer to as regional earthquakes or events, and those that originate outside the region, which I refer to as teleseismic earthquakes or events. Regional earthquakes in the NEUSSEC are usually smaller than M5 [Ebel, 1984] and body waves from most earthquakes in this region larger than M1.7 are detectable by several stations across the NEUSSEC with an ambient SNR greater than 2 at frequencies greater than 1 Hz [Atkinson, 2004, Zhao & Ebel, 1991, Ebel, 1984]. There is rarely much teleseismic signal at frequencies greater than 1 Hz [Vernon, 1998]. For the regional array, I therefore chose to use seismograms from regional earthquakes between M2.0 and M4.7 and seismograms from teleseismic earthquakes between M6.5 and M8.3 that occurred during the 2013-2016 time period (when the TA stations were active in the region). These earthquakes are listed in Tables 4 and 5. Data recorded by the local array contained much more ambient noise than the data from the regional array. Therefore, any earthquake (regional or teleseismic) that produced a seismogram that could be detected by visual inspection on multiple of the stations operated by Weston Observatory was used. This resulted in seismograms from regional earthquakes between M0.0 and M4.6 and teleseismic earthquakes between M4.6 and M8.2 being used in the analysis. These events are listed in Tables 6 and 7.

For each event and station that recorded an event, station metadata and velocity data were downloaded from the Incorporated Research Institutions for Seismology (IRIS) database using the MATLAB function `irisFetch.m` provided by IRIS. Information on earthquake times, locations, depths and magnitudes are available for regional earthquakes recorded by the regional array (Table 4), teleseismic earthquakes recorded by the regional

array (Table 5), regional earthquakes recorded by the ALSA (Table 6) and teleseismic earthquakes recorded by the ALSA (Table 7).

Coherence analysis requires that two waveforms have the same sample rate, so any recordings that were not made at 100 Hz were resampled up to 100 Hz, which was the highest frequency of data recordings available. Next, seismograms from regional earthquakes were filtered using a zero-phase digital band-pass filter into different frequency bands between 0.8-10 Hz, where signal amplitudes are expected to be greatest [Atkinson, 2004, Toksöz, 1991, Zhao & Ebel, 1991], while seismograms from teleseismic earthquakes were filtered using the same method into frequency bands between 0.05-3 Hz where the signal amplitudes should be measurable [Langston, 2014, Vernon et al., 1998]. Between these Teleseismic and Regional sources, I describe the coherence of earthquake body waves over frequencies between 0.05-10 Hz.

Once the waveforms are filtered, they are then windowed around each seismic phase and grouped into what I call a data subset, which includes every seismogram of the same seismic phase (teleseismic P or S or regional Pn or Sn), filter band and array (regional or local). An example data subset would be all teleseismic P waves filtered at 0.1-0.2 Hz recorded by the regional array. Windowing is designed to select only the teleseismic P or S phases or the regional Pn or Sn phases and remove as much energy as possible from other sources such as the coda and the arrivals of other seismic phases, which would be considered noise in this study (Figure 3). The arrival times for the seismic phases are selected manually by visual inspection on a T-X diagram (Figure 4). To window each phase for each data subset, the seismogram is split into two parts around the phase arrival, the presignal being any data prior to the phase arrival and the postsignal

being any data after the arrival. The mean frequency of the filter band is used to determine the mean period of the waveform. This mean period is used to window the data around the phase arrival time by selecting 3 periods of presignal and 5 periods of postsignal to be used for the coherence analysis. For each waveform the ambient SNR is calculated as in Equation (1) using the amplitudes from the 3 periods of presignal and 5 periods of postsignal.

Coherence is measured using normalized crosscorrelation, which produces a vector of values between -1 and 1. The normalized crosscorrelation of two vectors x and y is calculated as

$$r_{xy}(\tau) = \frac{\sum_n x_n y_{n+\tau}}{\sqrt{\sum_n x_n x_n^* \sum_n y_n y_n}} \quad (3)$$

where τ is the time shift applied to one vector relative to the other, or the shift in index, and n is the index [Sheriff, 1995, Schilling & Harris, 2011]. Each value in the vector $r_{xy}(\tau)$ corresponds to the similarity of the two vectors being crosscorrelated at the given time shift τ (Figure 5). Two identical vectors, or a vector that is equal to the other vector when multiplied by a scalar, with no time shift ($\tau = 0$) have a normalized crosscorrelation value of 1. A normalized crosscorrelation value of -1 at some value of τ is the result of an anticorrelation, where one vector is a negative multiple of the other at that value of τ . Normalized crosscorrelation values between -1 and 1 mean that vector y is not equal to vector x multiplied by some scalar at that value of τ , but instead varies independently from vector x with time or the index. The more independently vectors x

and y vary with time or the index, the closer the normalized crosscorrelation value will be to 0 [Schilling & Harris, 2011, Bungum *et al.*, 1971, Toksöz, 1991, Langston, 2014].

In this thesis, the vectors x and y are vector time series recordings of ground motions from the same data subset produced by the same event and recorded at two different stations. I call these waveforms x and y . I limit τ to values between ± 1 s because the waveforms should be most similar where the difference in phase arrival times between waveforms x and y is small. The normalized crosscorrelation $r_{xy}(\tau)$ is used to determine the coherence C_{xy} , which is calculated as

$$C_{xy} = \max(|r_{xy}(\tau)|) \quad (4)$$

where $-N \leq \tau \leq N$ and $N = 100$, or 1 second at the 100 Hz sample rate of waveforms x and y (Figure 4). Waveforms x and y might be recorded by stations that record differences in the first motion polarity based on the stations' locations and the earthquake's epicenter and focal mechanism. Therefore, the absolute value of $r_{xy}(\tau)$ is taken to avoid measuring anticorrelations as incoherent because an anticorrelation may result from a difference in first motion polarity. The maximum value of $|r_{xy}(\tau)|$ is taken to ensure coherence is the measure of the crosscorrelation at the value of τ where the two waveforms are most similar. The result is a coherence value C_{xy} that ranges between 0 and 1. The closer a coherence value is to 1, the more similar the two waveforms were that produced that coherence value and the closer a coherence value is to 0, the less similar waveforms were.

Within a data subset, C_{xy} is calculated for every pair of waveforms x and y that were produced by the same event. Coherence values produced by waveforms from different earthquakes are not addressed in this thesis and therefore any mention of C_{xy} implies that waveforms x and y were of the same seismic phase produced by the same earthquake, recorded on the same array, filtered to the same frequencies and windowed to the same size. Each pair of waveforms x and y has the interstation distance measured between the two stations that recorded them and the ambient SNR is found for each waveform as in Equation (1) where the 3 periods of data before the phase arrival is the presignal and the 5 periods of data after the phase arrival is the postsignal. For each data subset (same phase, filter and array), all values of C_{xy} (data available from multiple earthquakes) are plotted against interstation distance $d(x, y)$ and the lower of the two ambient SNRs for the station pair (Figures 7-14).

The plots (Figures 7-14) of coherence versus interstation distance are used to find the expected coherence value C_e for two P, S, Pn or Sn recordings with a given frequency and interstation distance. C_e is a simplification of the coherence data that attempts to empirically describe the average values of C_{xy} as a function of interstation distance, frequency and ambient SNR for each seismic phase. Values of C_e are found for each data subset by first separating all the values of C_{xy} within that data subset into 10 equally spaced bins of interstation distance, d_i where i is the bin number, an integer between 1 and 10. This results in a vector of coherence values $\overline{C_{xy}_i}$, where

$$\overline{C_{xy}_i} = [C_{xy_1}, \dots, C_{xy_n}, \dots, C_{xy_N}] \quad (5)$$

such that N is the number of waveform pairs, x and y , within that data subset that can be used to calculate a value of C_{xy} and where the interstation distance between the two receivers $d(x, y)$, is such that

$$d(x, y) \in d_i \quad (6)$$

As a result of it being produced by a data subset with limitations on interstation distance, $\overline{C_{xy_i}}$ is the set of all coherence values that were produced by the same seismic phase, filtered to the same frequency, recorded by the same array and that were divided into one of 10 equally sized interstation distance bins, the width of which is one tenth of the maximum interstation distance for which data were available on that array.

The next step in finding the expected coherence value C_e is to produce a histogram of coherence values $\overline{C_{xy_i}}$ for each interstation distance bin i for each data subset (Figure 6). These histograms are made with 100 equally spaced coherence value bins for data subsets from the regional array and with 10 equally spaced coherence value bins for data subsets from the local array. Each coherence value bin is defined by upper and lower coherence boundary values, C_m and C_{m+1} respectively, where m is an integer between 1 and 100 for regional array data subsets and an integer between 1 and 10 for local array data subsets. Therefore, for a given data subset, any coherence value C_{xy} within that data subset can be placed into an interstation distance bin, d_i as in Equation

(6) and then into a vector, $\overline{b_{m_i}}$, that contains all the coherence values within that coherence bin, where

$$\forall C_{xy} \in \overline{b_{m_i}} \quad (7.1)$$

$$C_m \leq (C_{xy} \in \overline{C_{xy_i}}) < C_{m+1} \quad (7.2)$$

Therefore,

$$\overline{b_{m_i}} = [C_{xy_1}, \dots, C_{xy_n}, \dots, C_{xy_M}] \quad (8)$$

where M is the number of coherence values made with waveform pairs, x and y , which are defined to be within the same interstation distance bin as in Equation (6) and produce a coherence value C_{xy} that falls within the same coherence bin as defined by Equations (7.1) and (7.2).

One bin number k corresponds to the coherence bin that contains the greatest number of $\overline{C_{xy_i}}$ points between coherence bin boundary values C_k and C_{k+1} as defined by Equation (7.2). I refer to the number of $\overline{C_{xy_i}}$ points within that bin as K , where

$$\overline{b_{k_i}} = [C_{xy_1}, \dots, C_{xy_n}, \dots, C_{xy_K}] \quad (9.1)$$

And $\overline{b_{k_i}}$ is defined such that for any other coherence bin, $\overline{b_{m_i}}$ defined as

$$\overline{b_{m_i}} = [C_{xy_1}, \dots, C_{xy_n}, \dots, C_{xy_M}] \quad (9.2)$$

$$K > M \quad (9.3)$$

k represents the peak of the coherence value histogram for the interstation distance bin, d_i for that data subset. The coherence value on which bin k is centered is what I refer to as the peak coherence value, C_{peak_i} for the vector, $\overline{C_{xy_i}}$ (Figure 6) and is defined as

$$C_{peak_i}(\overline{C_{xy_i}}) = \frac{C_k + C_{k+1}}{2} \quad (10)$$

where k corresponds to the vector of coherence values $\overline{b_{k_i}}$ as in Equations (9.1), (9.2) and (9.3).

In addition to the peak coherence value defined above, I also calculate what I call the two half peak coherence values, $C_{half\ peak\ 1_i}$ and $C_{half\ peak\ 2_i}$. These half peak coherence values are defined by the coherence bins $h1$ and $h2$ that each contain approximately half as many values of $\overline{C_{xy_i}}$ as the peak coherence bin on either side of C_{peak} (Figure 6). The vectors that contain all the coherence values in these two bins are defined as

$$\overline{b_{h1_i}} = [C_{xy_1}, \dots, C_{xy_n}, \dots, C_{xy_{H1}}] \quad (11.1)$$

$$\overline{b_{h2_i}} = [C_{xy_1}, \dots, C_{xy_n}, \dots, C_{xy_{H2}}] \quad (11.2)$$

where

$$H1 \cong H2 \cong \frac{K}{2} \quad (11.3)$$

$$h1 > k > h2 \quad (11.4)$$

$\overline{b_{h1_i}}$ is defined such that for any other coherence bin, $\overline{b_{m_i}}$ where $m > k$

$$\overline{b_{m_i}} = [C_{xy_1}, \dots, C_{xy_n}, \dots, C_{xy_M}] \quad (11.5)$$

and

$$|M - \frac{K}{2}| \leq |H1 - \frac{K}{2}| \quad (11.6)$$

$\overline{b_{h2_i}}$ is defined such that for any other coherence bin, $\overline{b_{m_i}}$ where $m < k$

$$\overline{b_{m_i}} = [C_{xy_1}, \dots, C_{xy_n}, \dots, C_{xy_M}] \quad (11.7)$$

and

$$|M - \frac{K}{2}| \leq |H2 - \frac{K}{2}| \quad (11.8)$$

The two half peak coherence values are defined as

$$C_{half\ peak\ 1_i}(\overline{C_{xy_i}}) = \frac{C_{h1} + C_{h1+1}}{2} \quad (12.1)$$

where

$$C_{half\ peak\ 1_i}(\overline{C_{xy_i}}) > C_{peak_i}(\overline{C_{xy_i}}) \quad (12.2)$$

and

$$C_{half\ peak\ 2_i}(\overline{C_{xy_i}}) = \frac{C_{h2} + C_{h2+1}}{2} \quad (13.1)$$

where

$$C_{half\ peak\ 2_i}(\overline{C_{xy_i}}) < C_{peak_i}(\overline{C_{xy_i}}) \quad (13.2)$$

For each interstation distance bin, these peak and half peak coherence values serve as a range of expected coherence values and are displayed as error bars on Figures 7-14 (see Figure 6 as an example). For a data subset the peak coherence value for each interstation distance bin is what I refer to as the expected coherence value, C_e . C_e is derived from my data, and I use it as the empirical relationship between coherence and interstation distance by writing it as

$$C_{e_i}(\nu, p, d(x, y)) = C_{peak_i}(\overline{C_{xy_i}}(\nu, p, d_i)) \quad (14)$$

For every interstation distance bin, d_i C_e is defined for that bin as C_{e_i} where ν is the filter frequency of the two different waveforms, p is the seismic phase, d is the interstation distance, and $\overline{C_{xy_i}}$ was determined using a data subset of the same seismic phase and frequency and had boundaries on the interstation distance bin d_i as defined in Equation (6). Values of C_{peak_i} are calculated for all 10 interstation distance bins within each data subset (Figures 7-14). Therefore, a given seismic phase p , frequency ν , and interstation

distance $d(x, y)$ will have an expected coherence value C_{e_i} that corresponds to the calculated value C_{peak_i} .

As explained previously, the coherent energy in a single value of C_{xy} might be the result of body waves or ambient noise. To determine whether the coherence values of a data subset are the result of coherent ambient noise or earthquake body waves, I performed the same type of coherence analysis as seen in Figures 7-14 on data that contains no body-wave signal. To do this, I simply windowed the data from the teleseismic earthquakes around the first P arrival to include 8 periods of presignal and 0 periods of postsignal. Performing the same steps to calculate coherence values on these waveforms containing only ambient noise produced expected coherence values, C_{e_i} for ambient noise (Figures 15-16).

Once the coherence values from each data subset are computed, they are then compared to the coherence values of ambient noise. For each data subset, every interstation distance bin has a histogram of the coherence values (Figures 7-14). The same is true of the coherence values of ambient noise (Figures 15-16). The histogram of coherence values from one interstation distance bin from one data subset, or the earthquake histogram, is compared to the histogram of the ambient noise for the corresponding frequency band and interstation distance bin. The noise histogram is first normalized to the earthquake histogram such that it contains the same number of points (Figure 17). The normalized noise histogram is then subtracted from the earthquake histogram to produce a histogram of the difference between earthquake coherence and ambient noise coherence for that data subset and interstation distance bin (Figure 17). Where there is a positive difference between the two histograms, there is earthquake

coherence data that were not the result of ambient noise. I am interested in the positive differences between the coherence histograms that had coherence values greater than the peak coherence value of the ambient noise histogram (Figure 17). The positive differences where the coherence was greater than the peak ambient noise coherence value indicate the number of coherence values in the data subset for this interstation distance bin that could not be the result of coherent ambient noise, but must contain coherent body-wave energy. Therefore, by comparing the size of the positive differences that were greater than the peak coherence value of the ambient noise to the number of data points in the interstation distance bin, I can get a percentage of the points in that interstation distance bin and data subset that definitely contain some coherent energy from earthquake body waves (Figure 17). This percentage represents the chance that the coherence seen between two random waveforms in that interstation distance bin and data subset is not the result of coherent ambient noise, but must be the result of coherent body-wave energy. I call this percentage the Coherent Body-Wave Percentage (CBP).

Before I produced CBPs for every interstation distance bin in every data subset, I limited the data such that only coherence values produced by waveforms with ambient SNRs between 1-3, 3-6, 6-10 and 10+ are used. This way, for each data subset and each interstation distance bin, I produce 4 different CBPs, one for each range of ambient SNRs (Figures 18-25). The plots display the percent chance that measured coherence must be the result of coherent body-wave energy within two waveforms at different frequencies, interstation distances, and ambient SNRs for a seismic phase. I am therefore able to describe how the coherence of different seismic phases vary as functions of frequency, interstation distance, and ambient SNR.

I summarize the results of Figures 18-25 by plotting the normalized mean CBP across all interstation distance bins vs the frequency band (Figure 26). The CBP is normalized by multiplying the CBP in each interstation distance bin by the number of coherence values in that interstation distance bin, summing these values together and then dividing the sum by the total number of coherence values across all interstation distance bins. This process is repeated for each of the four CBP limited to different ambient SNRs and produces a plot of CBP vs frequency (Figure 26). The results from the regional array and the ALSA are combined by taking the normalized mean CBP of the 20 interstation distance bins available between the two arrays. The result is 4 subplots of different ambient SNR limited CBPs vs frequency, one subplot for each of the seismic phases, teleseismic P and S waves and regional Pn and Sn waves (Figure 26). This allows me to describe the SNR of earthquake body waves as a function of frequency and ambient SNR. Larger CBPs correspond to a more coherent body-wave energy and therefore larger CBPs also correspond to larger earthquake body-wave SNRs. Frequencies where the CBP peaks for a given seismic phase are the frequencies where the SNR for that seismic phase peaks.

Comparing the CBP for different ambient SNRs for each seismic phase allows me to describe the amount of scattered noise present at different frequencies. An increase in the body-wave SNR could be the result of an increase in signal strength, or a decrease in either the ambient or scattered noise. Therefore, an increase in the CBP would be the result of either an increase in signal strength or a decrease in the strength of the ambient and/or scattered noise. For two different CBPs to be the same, there must be an equal body-wave SNR. An increase in ambient SNR could only result from an increase in

signal strength or a decrease in ambient noise. Therefore, if increasing the ambient SNR at a certain frequency does not increase the CBP, the body-wave SNR must be equal and the majority of the noise must be in the form of scattered noise rather than ambient noise. I am able to describe the frequencies where scattered noise is strongest by examining the effect larger ambient SNRs have on the CBPs at different frequencies.

I use the CBPs as a proxy for the SNR of earthquake body waves, and by comparing the CBP for different seismic phases and different ambient SNRs at different frequencies, I am able to draw conclusions about the amount of scattered noise present in earthquake body-wave recordings at different frequencies.

RESULTS

The coherence values for teleseismic P and S waves and regional Pn and Sn waves recorded on the regional array at various frequency bands between 0.05-10 Hz are shown in Figures 7-10. For a given seismic phase, frequency band, and interstation distance, the expected coherence C_e is determined by finding the peak coherence value (displayed as error bars on the plots along with the half peak coherence values) that corresponds to that phase, frequency, and interstation distance. Coherence increases with decreasing frequency and increasing ambient SNR. The coherence values for teleseismic P waves seen in Figure 7 can be separated into two main groups based on frequency; the first group includes frequencies of 0.05-1.6 Hz in subplots 7(a)-7(e) and the second group includes frequencies of 3-10 Hz in subplots 7(g) and 7(h). In the first group peak coherence values are generally greater than 0.8 at all interstation distances, decreasing slightly with increasing frequency and interstation distance. In the second group the peak and half peak coherence values suggest that coherence is randomly distributed around the peak coherence values of 0.5, and that there is no relationship between coherence and interstation distance at these frequencies. This suggests that coherence of teleseismic P waves is greater at lower frequencies.

The coherence values of ambient noise on the regional array at 0.05-10 Hz are shown in Figure 15. Subplots 15(c)-15(h) display coherence values that are randomly

distributed around 0.5, much like subplots 7(g) and 7(h). This suggests that for coherent body-wave energy to be detected on the regional array at frequencies above 0.2 Hz, the earthquake coherence values must exceed the random distribution around 0.5 that the ambient noise displays at all interstation distances. Subplots 15(a) and 15(b) stand out from the rest of the noise coherence values because the coherence is not randomly distributed around 0.5 like it is at higher frequencies. In subplot 15(b) some of the half peak coherence values reach as high as 0.9 and while the peak coherence values remain around 0.5, the half peak coherence values suggest the distribution of coherence values is not random around the peaks, but skews towards higher values. The ambient noise at frequencies between 0.05-0.1 Hz produces coherence values greater than 0.9 across the entire array. These frequencies are the same frequencies where the ambient noise amplitudes are greatest (Figure 1) and where ocean waves and swells are known to produce coherent energy [Seydoux, et al., 2016], suggesting that highly coherent energy from ocean activity is being measured at these frequencies in the NEUSSEC. Most of the coherent energy from ambient noise is present at frequencies between 0.05-0.1Hz.

The coherence of teleseismic P waves recorded on the regional array appears to be similar to the coherence of ambient noise at frequencies below 0.1 Hz and at frequencies above 3 Hz. Figure 18 displays the CBP of teleseismic P waves for different interstation distances and frequencies. Most of the CBPs are close to 50%, and there does not appear to be much change in the CBP with increasing interstation distance. The greatest increase in CBP is seen as a result of increasing ambient SNR at frequencies below 0.2 Hz, increasing from roughly 15% for ambient SNRs between 1-3 up to roughly 70% for ambient SNRs greater than 10%.

For teleseismic P waves with ambient SNRs greater than 10, there is a pattern of decreasing CBPs with increasing frequency and little dependence on the interstation distance. This suggests that there is more coherent body-wave energy at frequencies between 0.05-0.4 Hz than there is at frequencies above 0.4 Hz, but there is also more coherent noise energy at frequencies between 0.05-0.4 Hz than there is at frequencies above 0.4 Hz. If there were less coherent noise energy at 0.05-0.4 Hz, I would expect to see higher CBPs for lower ambient SNRs at those frequencies (Figure 18). Therefore, an ambient SNR greater than 10 is needed to get CBPs above 50% between 0.05-0.4 Hz. Where the ambient SNR is lower than 10, CBPs above 70% can be found at frequencies above 3 Hz. The coherence values produced by the P waves seen in subplots 7(g) and 7(h) are not all randomly distributed like the coherence values seen in subplots 15(g) and 15(h), some values with ambient SNRs greater than 3 appear between 0.5-0.8, higher than the distribution of ambient noise coherence values. The CBPs above 70% for ambient SNRs between 3-10 and frequencies above 3 Hz suggest that highly coherent teleseismic P waves still stand out above the background noise at frequencies above 3 Hz.

Langston [2014] used normalized crosscorrelation as a measurement of coherence for teleseismic P and S waves in the Central United States, and in that region, he found results similar to those in this study, namely that the coherence values from teleseismic P waves are close to 1 out to interstation distances of 2500 km for frequencies between 0.05-0.4 Hz. Previous studies have shown waveform coherence drops with increasing frequency and interstation distance [Bungum et al., 1971, Toksöz, 1990, Langston, 2014], suggesting that teleseismic P waves behave similarly in the NEUSSEC to those in the Central United States and other regions that have been studied using similar kinds of

analyses. My results show that ambient noise produces coherence values above 0.9 at frequencies between 0.05-0.1 Hz, which suggest that some of the coherent energy seen in these other studies might be the result of coherent ambient noise energy; however, my results also show that ambient SNRs greater than 10 are sufficient to be certain that 70% of the waveforms at frequencies below 0.4 Hz contain coherent body-wave energy that can be detected above the noise.

The teleseismic S waves in Figure 8 show coherence values averaging around 0.5 at all frequencies and interstation distances except the smallest interstation distance bin for the lowest frequencies, 0.05-0.1 Hz, where peak coherence is close to 0.8. In comparison to the P waves in Figure 7, the coherence values in Figure 8 are much smaller. S-wave coherence values change with frequency, appearing similar to the distribution of ambient noise coherence (Figure 15) at frequencies between 0.4-10 Hz which includes lower frequencies than the frequencies where P-wave coherence values appear similar to noise coherence values (3-10 Hz). The ambient SNRs of the S waves range from roughly 1-4 which is lower than the 1-50+ range of the P waves which is likely the result of secondary P waves and scattered P-wave arrivals being included in my measurement of ambient noise amplitudes. At frequencies below 0.4 Hz however, S-wave phases with ambient SNRs greater than 3 generally result in coherence values greater than 0.8 across the entire array as in subplot 8(a), which are similar coherence values to what was found for the teleseismic P-waves. The coherence values around 0.8 from waveforms with ambient SNRs greater than 4 are similar to the S-wave coherence values Langston [2014] found, which remained above 0.8 out to 2500 km at frequencies below 0.2 Hz. Langston [2014] used data from 3 teleseismic earthquakes specifically

selected for ambient SNRs greater than 5, so this requirement for ambient SNRs to be greater than 4 appears to be necessary for coherence values to be greater than the random distribution around 0.5 that is seen in the coherence of ambient noise (Figure 15).

Comparing my teleseismic S-wave coherence values to the coherence of ambient noise results in CBPs lower than 50% at all frequencies other than 3-5 Hz for ambient SNRs between 1-3 (Figure 19), which is similar to the CBPs of the teleseismic P waves. This suggests that highly coherent S waves can be detected above the noise at frequencies between 3-5 Hz, just like for the case of P waves. Higher ambient SNRs result in higher CBPs which is similar to the results seen for P waves (Figure 18). The S waves produce CBPs greater than 70% at frequencies between 0.05-0.4 Hz with ambient SNRs between 6-10. The P waves required ambient SNRs greater than 10 to produce similarly high CBPs at 0.05-0.4 Hz, which suggests that there is less coherent ambient noise for the S waves at these frequencies. This is probably because my measurement of the ambient SNR of S waves includes the secondary P-wave arrivals and scattered P-wave energy in the ambient noise and I do not expect this form of ambient noise to be coherent.

Coherence values for Pn and Sn waves from regional NEUSSEC earthquakes are plotted against interstation distance and ambient SNR in Figures 9 and 10. For both Pn and Sn waves the peak coherence values are around 0.5 for all interstation distances and frequencies. These regional Pn and Sn phases have generally lower ambient SNRs than those of the teleseismic P and S waves respectively, suggesting that on average the signal strength of the regional body-waves analyzed in this study are lower than the signal strength of teleseismic body-waves that were analyzed. At frequencies greater than 1.6 Hz there are Pn and Sn waveforms with ambient SNRs greater than 6 that produce

coherence values greater than 0.7 at interstation distances less than 600 km. This observation suggests that the signal strength and therefore the coherence of regional phases is greatest at frequencies between 1.6-10 Hz. Where ambient SNRs are less than 6, the coherence values appear randomly distributed around 0.5, similar to the distribution of ambient noise coherence values (Figure 15). The CBPs for the regional Pn and Sn phases recorded on the regional array are shown in Figures 20 and 21. Both phases show CBPs below 10% at frequencies below 0.1 Hz and CBPs that increase to 50-80% at frequencies above 3 Hz. Increasing the ambient SNR of Pn waves increases the CBPs from below 10% to roughly 50% at frequencies below 3 Hz, but higher ambient SNRs do not lead to increased CBP sat 3-5 Hz, which remain constant at roughly 60% for all ambient SNRs. The CBPs for Sn waves also increase at frequencies below 3 Hz with increasing ambient SNRs, but the CBPs remain constant at around 70% at 3-5 Hz for all ambient SNRs. The CBPs for the two regional phases are greatest at 3-5 Hz, suggesting that the body-wave SNR is greatest at these same frequencies. The 3-5 Hz frequencies where the body-wave SNR is greatest also appear to be the frequencies where scattered noise is greatest because an increase in the ambient SNR at these frequencies does not result in an increase in the CBP.

The coherence values for teleseismic P and S waves and regional Pn and Sn waves recorded on the ALSA at various frequency bands between 0.05-10 Hz are shown in Figures 11-14. Teleseismic P and S waves produce coherence values close to 1.0 when the ambient SNRs are higher than 3 and the frequencies are lower than 0.8 Hz, which are similar coherence values to what was seen on the regional array at the same frequencies and ambient SNRs. At frequencies greater than 0.8 Hz the coherence values decrease

until 3 Hz for the P waves and 0.8 Hz for the S waves; above those frequencies the respective coherence values appear randomly distributed around 0.5 and similar to the distribution of ambient noise coherence values in Figure 16. The coherence values produced by regional Pn and Sn phases recorded on the ALSA are shown in Figures 13-14 and appear to be randomly distributed around 0.5 except for waveforms between 1.6-10 Hz with ambient SNRs > 4 , where coherence values are greater than 0.8 for all interstation distances. The CBPs for the ALSA are shown in Figures 22-25. There are very few coherence values produced by ALSA for either regional or teleseismic phases where the ambient SNR is greater than 3, and therefore conclusions about the coherence on ALSA can only be made for ambient SNRs between 1-3. The CBPs increase with increasing frequency, from around 30% at 0.05-0.1 Hz to around 70% at 3-5 Hz. This pattern is present for both teleseismic and regional P and S waves and would suggest that the coherence values peak at 3-5 Hz for all phases studied.

A summary of the different CBPs for different seismic phases across the two arrays is shown in Figure 26. For ambient SNRs between 1-3, teleseismic P and S waves and regional Pn and Sn waves all see a peak in the CBP around 50-60% at the 3-5 Hz frequency band. This would suggest that body-wave SNR also peaks at 3-5 Hz. The analyses of all four phases also demonstrate that a higher ambient SNR results in a higher CBP and therefore a higher body-wave SNR, but this increase in CBPs is not constant across all frequencies. At frequencies below 1 Hz CBPs for all four phases produced by waveforms with ambient SNRs between 1-3 are generally below 30%, but CBPs calculated using waveforms with ambient SNRs greater than 10 result in CBPs greater than 50% and as high as 70%. While coherence of ambient noise at frequencies below 0.1

Hz was consistently greater than 0.9, teleseismic earthquake body waves with ambient SNRs greater than 10 will still produce more coherent energy than the ambient noise would at those frequencies. Two teleseismic P waves with ambient SNRs greater than 10, for example, have a 50% chance of containing coherent energy that could not be ambient noise and must therefore be earthquake body-wave energy at frequencies between 0.05-0.1 Hz. The difference in CBPs for the same seismic phase with different ambient SNR ranges is most interesting at 3-5 Hz, particularly for the Pn phase. At these frequencies the Pn CBP appears to be around 50% regardless of the range of ambient SNR values used. This suggests that a relative increase in the signal strength compared to the strength of the ambient noise does not result in an increase in the body-wave SNR and that the strength of scattered noise energy is increasing at the same relative proportion to the signal strength as compared to the ambient noise. 3-5 Hz appears to be the frequency band where scattered noise is strongest for Pn waves because at all other frequencies I see an increase in the CBP when the ambient SNR increases. The CBPs of Sn waves produced using ambient SNRs between 1-3 are more than 10% smaller than the CBPs of Sn waves produced using ambient SNRs between 3-6 at all frequencies except 3-5 Hz. This likewise suggests that scattered energy is stronger at 3-5 Hz than other frequencies. The greatest scattering occurs when the sizes of the heterogeneities in the crust are similar to or larger than the wavelengths of the incident energy. If the scattered energy is greatest at frequencies between 3-5 Hz, this would suggest there are a large number of heterogeneities in the crust with sizes on the order of 1-5 km. The teleseismic P and S waves appear to be less affected by the increased scattering at these frequencies,

suggesting their travel paths interact with fewer of the scattering heterogeneities than the Pn and Sn waves.

In the NEUSSEC, earthquake body-wave coherence and SNR are greatest at frequencies between 3-5 Hz. At these frequencies, any two waveforms for the same P, S, Pn or Sn phase have a roughly 50% chance of containing coherent body-wave energy that is different from coherent energy in the ambient noise. 3-5 Hz is also the frequency band where scattered noise is strongest in the region. At frequencies below 3 Hz, an increase in the ambient SNR of earthquake body waves increases the body-wave SNR. At frequencies above 3 Hz, an increase in the ambient SNR of earthquake body waves might increase the body-wave SNR, but there is also an increase in the strength of scattered noise that prevents the body-wave SNR from increasing.

DISCUSSION

I used coherence as a proxy for the SNR of body waves arriving at receivers throughout the NEUSSEC. This analysis is based on the assumption that body waves from the same event produce coherent energy at different receivers, while scattered noise results in random incoherent energy at different receivers and any coherent energy from ambient noise could be accounted for. My findings for the relationship between coherence, interstation distance and frequency are consistent with previous studies [Bungum *et al.*, 1971, Toksöz, 1991, Langston, 2014] who all found coherence values decreased with increasing frequency and interstation distance. Bungum *et al.* [1971] found that teleseismic P waves produced coherence values that peaked at 0.8 for frequencies around 1 Hz for interstation distances less than 10 km. Toksöz [1991] found that the coherence values for regional S waves recorded at 2 Hz ranged between 0.6 and 1 for interstation distances below 3 km. Langston [2014] found teleseismic P and S waves produced coherence values greater than 0.9 at interstation distances up to 2500 km at frequencies below 0.2 Hz. All three of these studies found that the coherence values decreased with increasing interstation distance and increasing frequency, a pattern also seen in this thesis. If the data used in this thesis are selected such that the interstation distances, waveforms and ambient SNRs used are similar to those used in by previous studies [Bungum *et al.*, 1971, Toksöz, 1991, Langston, 2014], then similar values of

coherence for different interstation distances and frequencies would be found. Unlike previous studies, however, I was able to compare the body-wave coherence to the coherence of the ambient noise throughout the region, which demonstrated there is an increase in scattered noise at frequencies between 3-5 Hz with an increase in P and S signal amplitudes. This result is consistent with the understanding that scattering is stronger at frequencies above 1 Hz because the velocity heterogeneities in the crust that cause the scattering are usually smaller than 10 km in diameter and do not scatter energy with wavelengths larger than themselves [Vernon et al., 1998, Stein & Wysession, 2003].

All of the results seen in Figures 7-25 were combined to make summary Figure 26 that depicts the percent chance that any two waveforms would contain coherent energy that could not be ambient noise but must be earthquake body waves. Figure 26 also shows how this percent chance changes with different frequencies and ambient SNRs. Where these CBPs are large, the SNR must also be large because there is more coherent energy present in the waveforms than just the coherent energy of the ambient noise. Higher ambient SNRs usually result in an increase in these CBPs and in the body-wave SNR, but at frequencies between 3-5 Hz there is an increase in the scattered noise found in regional body-wave seismograms that limits a higher CBPs, or therefore a higher body-wave SNR. This increase in scattered noise at frequencies between 3-5 Hz is present in regional head waves that bottom out at the Moho discontinuity, but I see no evidence of an increase in scattered noise at the same frequencies for teleseismic first arrivals. This suggests that the travel paths of teleseismic P and S waves avoid most of the heterogeneities that cause scattering in the NEUSSEC.

Previous studies have found significant scattering can take place in the near surface weathered layer [Vernon *et al.*, 1998]. Toksöz [1990] found that S waves in the Lg phase from regional events contained no coherent body-wave energy at frequencies greater than 2 Hz. These results were from studies in Norway on crystalline rock exposed at the surface, therefore eliminating any possible scattering effects from the near surface weathered layer, and the coherence values were randomly distributed at frequencies above 2 Hz. Applying the methods used in this thesis to analyze data from exposed rock sites would demonstrate whether the low coherence seen by Toksöz [1990] was a result of low ambient SNRs or scattering. This would determine whether the scattering I see in the NEUSSEC is likely taking place in the near-surface weathered layer or in the deeper crust and upper mantle. Further work could be done with the NEUSSEC data to see which stations on average produce the largest coherence values and which stations have more or less coherent ambient noise than one another. When compared to the local geology of the region, this could reveal differences in the scattering as a result of the different rock types found throughout the region.

I have presented a method for predicting the amount of scattered energy present in a body-wave signal recorded in the NEUSSEC. I found that teleseismic and regional earthquake body-wave signals here are most coherent at frequencies below 1.6 Hz, but that when compared to the coherence of ambient noise, frequencies between 3-5 Hz are where these waveforms have the greatest chance of containing coherent body-wave energy. I interpret this to mean the body-wave SNR is greatest at 3-5 Hz, particularly for regional earthquakes. Also, the 3-5 Hz frequency band is where I found regional earthquake body-waves contain the most scattered energy compared to other frequencies.

Understanding the frequencies where scattering takes place and how different waveforms are affected by scattering will allow future studies to estimate which body-wave signals have the least scattered noise and ambient noise, and therefore the most coherent earthquake signals.

CONCLUSIONS

Teleseismic P and S waves and regional Pn and Sn waves recorded in the NEUSSEC produce coherence values close to 1 at frequencies below 1.6 Hz, interstation distances up to 1500 km, and ambient SNRs greater than 10, suggesting high body-wave SNRs at these frequencies. Frequencies higher than 1.6 Hz resulted in lower coherence values at all interstation distances for teleseismic P and S waves, but higher coherence values for regional Pn and Sn waves where the ambient SNRs were greater than 6. For two arbitrary P, S, Pn or Sn waveforms, the 3-5 Hz frequency band is where the two waveforms have a 50% or greater chance of containing coherent energy that is not ambient noise; these frequencies are where this percent chance is greatest. At frequencies between 3-5 Hz, the body-wave SNR of regional Pn waves was not increased by increasing the ambient SNR, indicating that most of the noise at these frequencies was in the form of scattered noise. The 3-5 Hz frequency band is where the effects of scattering were most pronounced on the coherence values of regional seismic phases, suggesting that most scattering in the crust of the NEUSSEC takes place at these frequencies. Understanding the frequencies where earthquake body-wave signals are contaminated by scattered noise will help future studies select their data if clear body-wave signals are required.

REFERENCES

- Aki, Keiiti. "Analysis of the Seismic Coda of Local Earthquakes as Scattered Waves." *Journal of Geophysical Research* 74.2 (1969): 615-31.
- Aki, Keiiti. "Scaling Law of Seismic Spectrum." *Journal of Geophysical Research* 72.4 (1967): 1217-31.
- Aki, Keiiti. "Scattering of P Waves under the Montana Lasa." *Journal of Geophysical Research* 78.8 (1973): 1334-46.
- Aki, Keiiti, and Bernard Chouet. "Origin of Coda Waves: Source, Attenuation, and Scattering Effects." *Journal of Geophysical Research* 80.23 (1975): 3322-42.
- Atkinson, Gail M. "Empirical Attenuation of Ground-Motion Spectral Amplitudes in Southeastern Canada and the Northeastern United States." *Bulletin of the Seismological Society of America* 94.3 (2004): 1079-95.
- Brune, James N. "Tectonic Stress and the Spectra of Seismic Shear Waves from Earthquakes." *Journal of Geophysical Research* 75.26 (1970): 4997-5009.
- Bungum, H., E. S. Husebye, and F. Ringdal. "The NORSAR Array and Preliminary Results of Data Analysis." *Geophysical Journal International* 25.1-3 (1971): 115-26.
- Campillo, Michel. "Phase and Correlation in 'Random' Seismic Fields and the Reconstruction of the Green Function." *Pure and applied geophysics* 163.2 (2006): 475-502
- Dahal, Nawa R., and John E. Ebel. "Method for Determination of Depths and Moment Magnitudes of Small-Magnitude Local and Regional Earthquakes Recorded by a Sparse Seismic Network." *Bulletin of the Seismological Society of America* 109.1 (2019): 124-37.
- Dreger, Douglas S., and Donald V. Helmberger. "Broadband Modeling of Local Earthquakes." *Bulletin of the Seismological Society of America* 80.5 (1990): 1162.
- Ebel, John E. "The Effect of Crustal Scattering on Observed High-Frequency Earthquake Seismograms." *Geophysical Journal International* 98.2 (1989): 329-41.
- Ebel, John E. "Statistical Aspects of New England Seismicity from 1975 to 1982 and Implications for Past and Future Earthquake Activity." *Bulletin of the Seismological Society of America* 74.4 (1984): 1311.
- Gutenberg, B. "On Microseisms." *Bulletin of the Seismological Society of America* 26.2 (1936): 111-7.
- Hock, S., et al. "Mapping Random Lithospheric Heterogeneities in Northern and Central Europe." *Geophysical journal international* 157.1 (2004): 251-64.
- IRIS Transportable Array. USArray Transportable Array: International Federation of Digital Seismograph Networks., 2003

- Langston, C. A. "Coherence of Teleseismic P and S Waves Across the Transportable Array." *Bulletin of the Seismological Society of America* 104.5 (2014): 2253-65.
- Langston, Charles A. "Scattering of Teleseismic Body Waves Under Pasadena, California." *Journal of Geophysical Research: Solid Earth* 94.B2 (1989): 1935-51.
- Mack, Harry. "Nature of Short-period P-wave Signal Variations at LASA." *Journal of Geophysical Research* 74.12 (1969): 3161-70.
- Powell, Christine A. "Seismic Noise in Northcentral North Carolina." *Bulletin of the Seismological Society of America* 82.4 (1992): 1889-909.
- Rost, Sebastian, and Christine Thomas. "Array Seismology: Methods and Applications." *Reviews of geophysics (1985)* 40.3 (2002): 1008-27.
- Saikia, Chandan K., and Robert B. Herrmann. "Application of Waveform Modeling to Determine Focal Mechanisms of Four 1982 Miramichi Aftershocks." *Bulletin of the Seismological Society of America* 75.4 (1985): 1021.
- Schilling, Robert J., and Sandra L. Harris. *Fundamentals of Digital Signal Processing using MATLAB*. 2nd ed. Boston, MA, USA: Cengage Learning, 2011.
- Seydoux, L., et al. Spatial Coherence of the Seismic Wavefield Continuously Recorded by the USArray. 43 Vol. *American Geophysical Union (AGU)*, 2016.
- Sheriff, R. E., and L. P. Geldart. *Exploration Seismology*. 2nd ed. Cambridge: Cambridge University Press, 1995. Cambridge Core.
- Stein, S., and M. Wysession. *An Introduction to Seismology, Earthquakes, and Earth Structure*. 1st ed. Malden, MA, USA: Blackwell Pub., 2003.
- Toksöz Nafi, M., Anton M. Dainty, and Edmond E. Charrette. "Coherency of Ground Motion at Regional Distances and Scattering." *Physics of the Earth and Planetary Interiors* 67.1 (1991): 162-79.
- Vernon, Frank L., et al. "Near-Surface Scattering Effects Observed with a High-Frequency Phased Array at Pinyon Flats, California." *Bulletin of the Seismological Society of America* 88.6 (1998): 1548.
- Zhao, Xiaomin, and John E. Ebel. "Radiation Pattern of Crustal Phases of New England Earthquakes." *Geophysical Journal International* 106.3 (1991): 647-55.

FIGURES

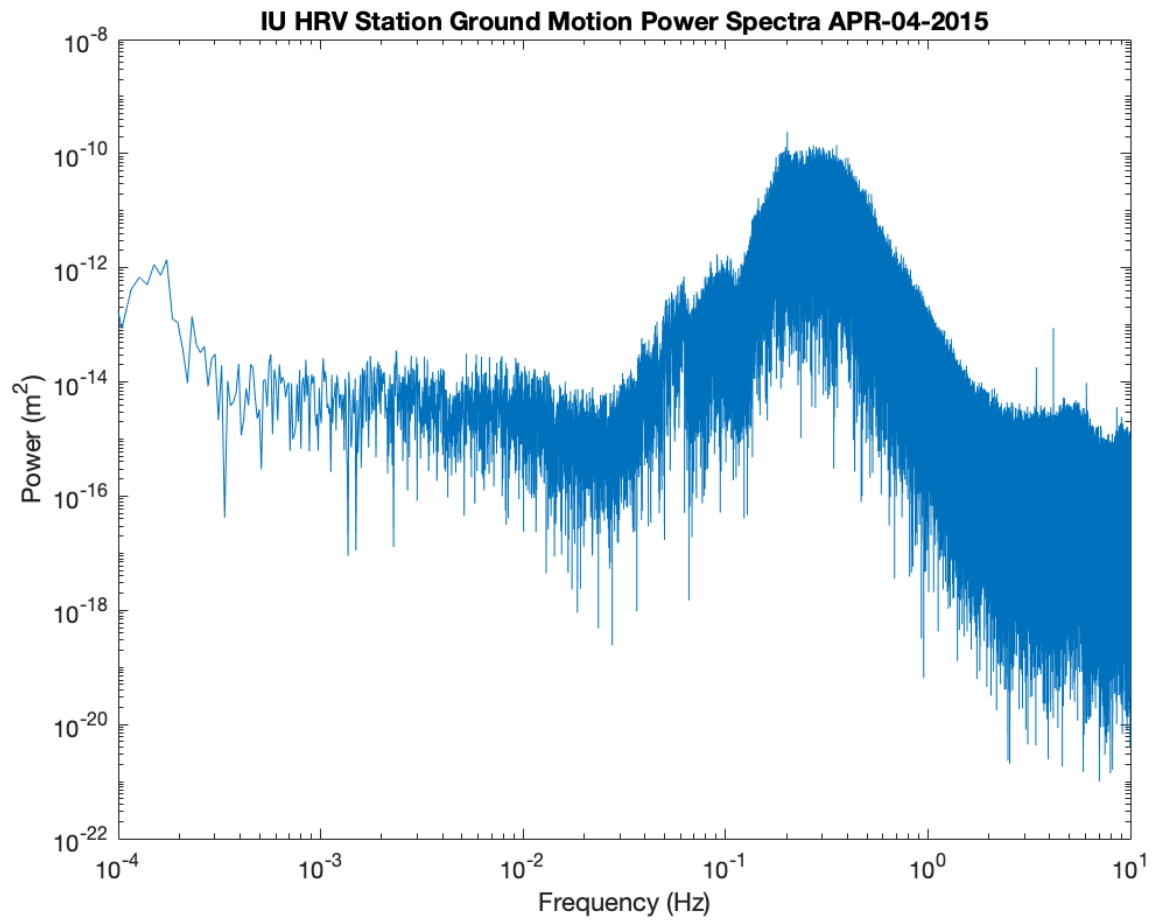


Figure 1: The power spectrum of vertical velocity noise recorded on April 4th, 2015, by IU Network's HRV station in Harvard Massachusetts. Noise energy is greatest at frequencies between 0.1-0.2 Hz.

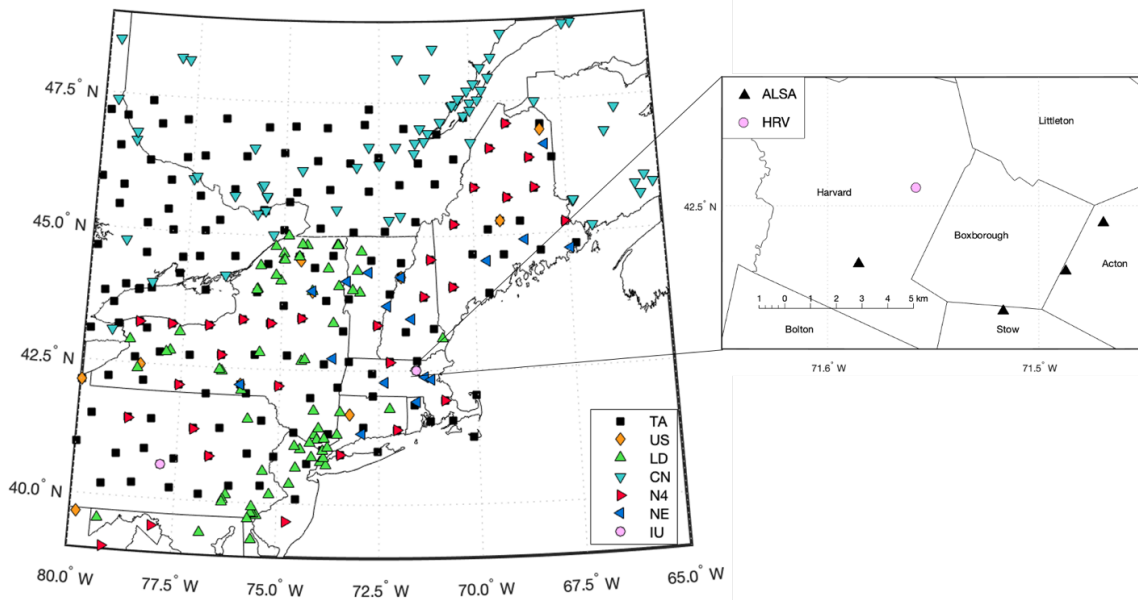


Figure 2. A map of the Northeastern United States and Southeastern Canada (NEUSSEC) showing the station locations from the 2013-2016 Transportable Array (TA) as well as stations from the US, LSCS, CN, N4, NE and IU networks. These stations represent the regional array used in the study. Of the 305 stations present 138 of them are from the TA and have an average station separation of roughly 70 km. The box in Massachusetts shows station locations of the Acton Littleton Seismic Array as of 6 September 2018. Also indicated are the Massachusetts town lines and town names.

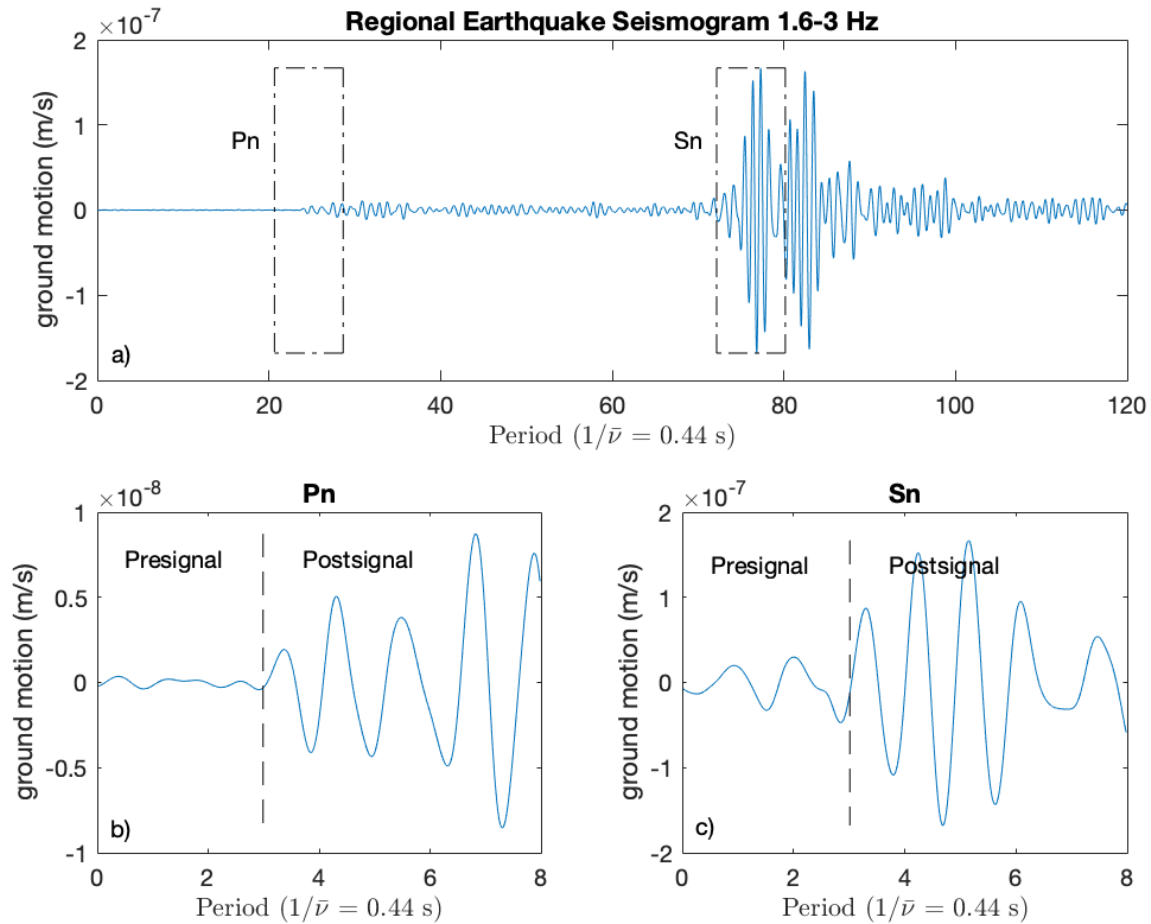


Figure 3. The seismogram from the M3.1, April 20, 2015, regional earthquake recorded on the TA station D55A, filtered at 1.6-3 Hz. The seismogram is plotted against the number of periods of the average filter frequency, $\bar{\nu}$. a) The full seismogram is plotted with boxes indicating the Pn and Sn phase windows. b) The Pn phase window as depicted in a), where the vertical line indicates the phase arrival. The window includes 3 periods of presignal data before the phase arrival and 5 periods of postsignal data after the phase arrival. c) The same as b), but for the Sn phase instead of the Pn phase.

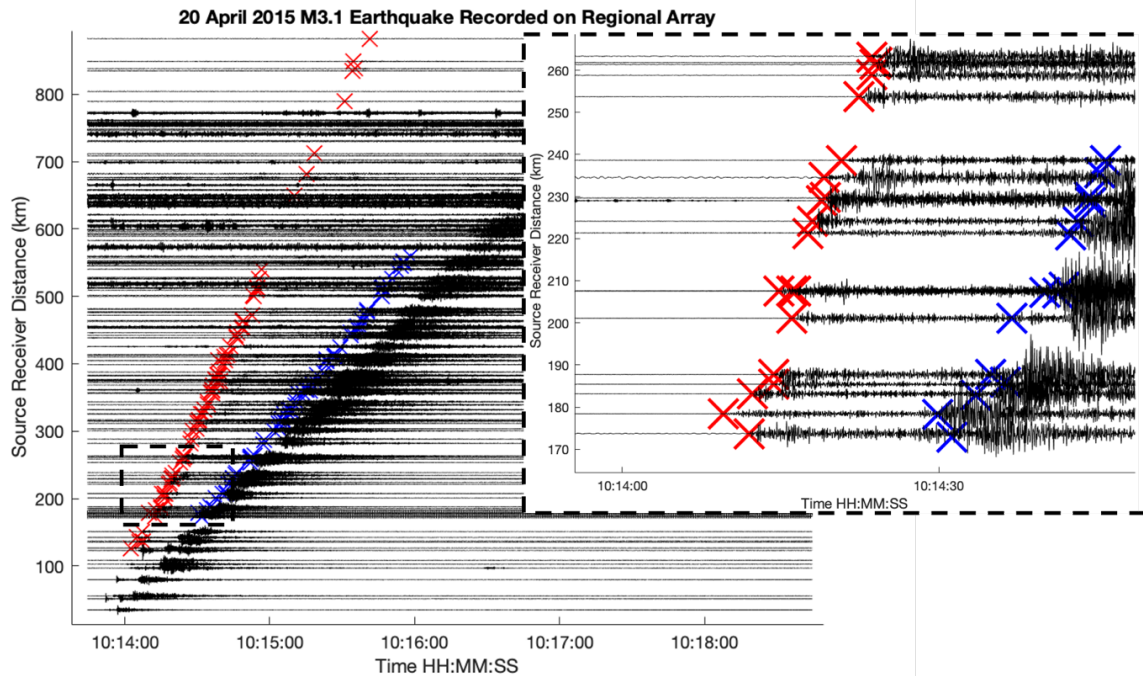


Figure 4. Vertical component seismograms recorded on the regional array and filtered between 1-15 Hz for the 20 April 2015 M3.1 earthquake located roughly 200 km north of Montreal are displayed at the epicentral distance for each station. The arrival times (x symbols) for the Pn (red) and Sn (blue) phases were picked by hand. Station recordings where no phase can be detected visually are not given a phase arrival time and are not processed for coherence, and for clarity they are removed from the plot in the cutout indicated by the dashed box.

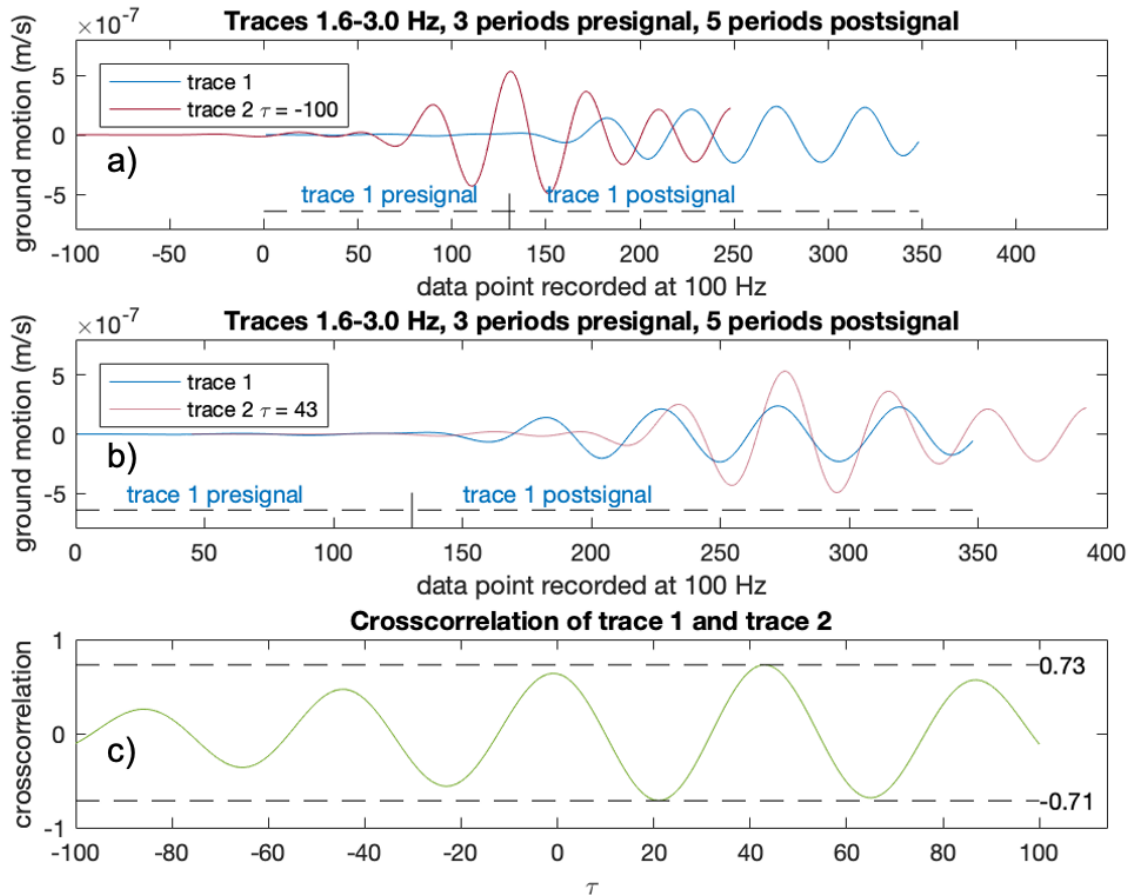


Figure 5. Coherence is calculated for two traces using Equations (2) and (3). Each trace is recorded at a sample rate of 100 Hz, and then filtered with a bandpass filter of 1.6-3 Hz. The time shift of the trace 2 relative to trace 1 is represented by τ , which ranges from -100 to 100, or -1 second to +1 second at the 100 Hz sample rate. a) trace 1 and trace 2 are displayed with a time shift of -100, such that trace 2 begins 100 samples or 1 second before trace 1 begins. b) trace 1 and trace 2 are displayed with a time shift of +43, such that trace 2 begins 43 samples after trace 1 begins. This time shift is the value of τ that produces the maximum absolute value of the crosscorrelation of the two traces. c) The normalized crosscorrelation of traces 1 and 2 as calculated by equation (3). The maximum and minimum values are displayed. The coherence value for these two traces is 0.73, the maximum of the absolute value of the crosscorrelation, which occurs at a τ value of 43 as determined by Equation (4).

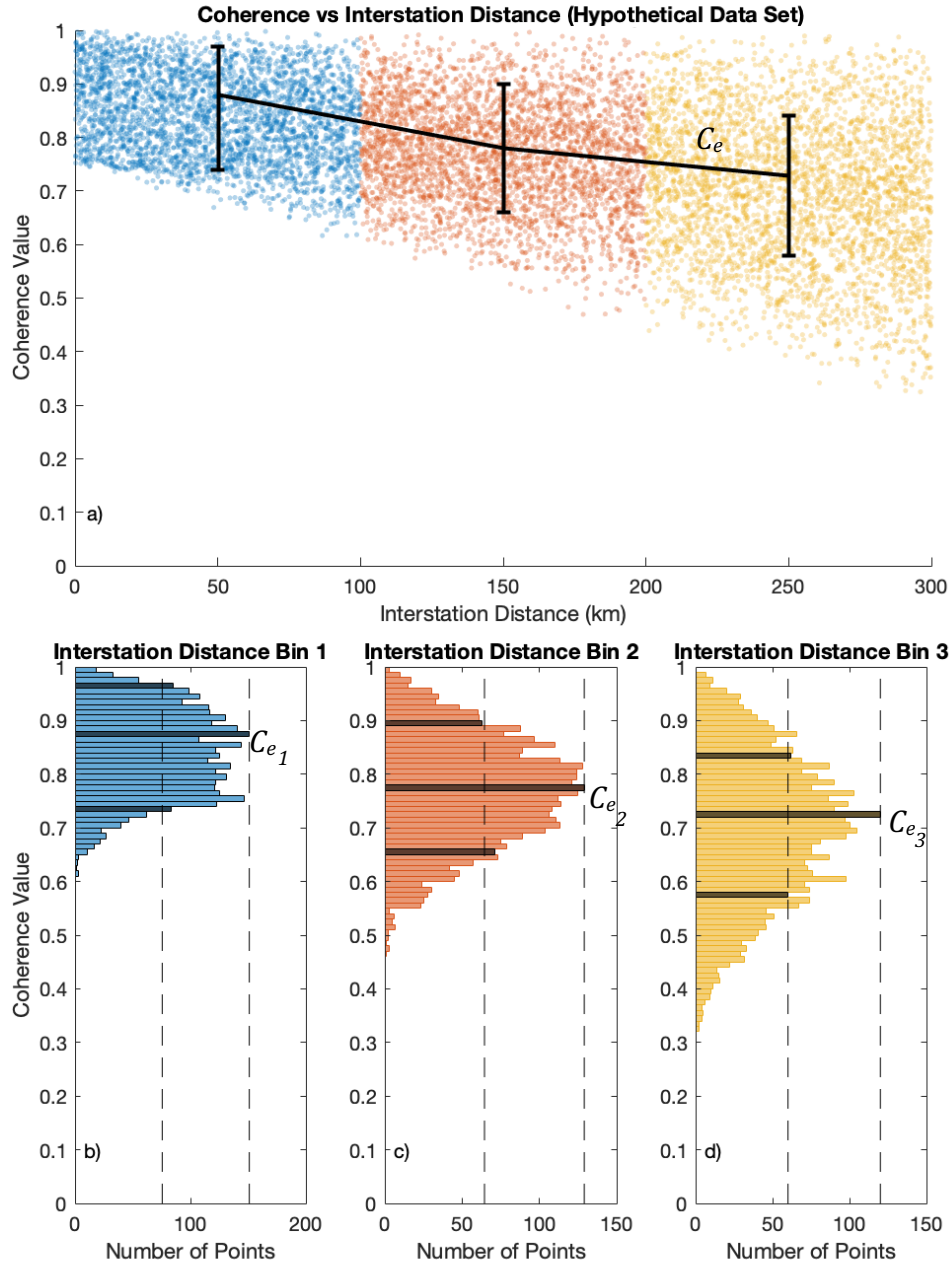


Figure 6: The methodology used to find expected coherence values C_e . The data points used here were generated solely for this figure and have no relationship to the results of this thesis. a) Coherence values C_{xy} are divided into 3 equal sized bins of interstation distance d_i (10 bins are used for the real data analyzed in this thesis). The error bars represent the peak and half peak coherence values, the calculations of which are explained by the following panels. b) c) d) A histogram of $\overline{C_{xy}}$ is produced for each d_i bin, as indicated by the color coding. The histogram peak and half peaks are marked as the black histogram bars, while the value of the peak and the half-peaks are indicated with vertical dashed lines. The coherence values that correspond to these peaks are referred to as the peak and half-peak coherence values for bin d_i . C_e is the peak coherence value for each bin d_i , displayed by the connecting line between error bars in a).

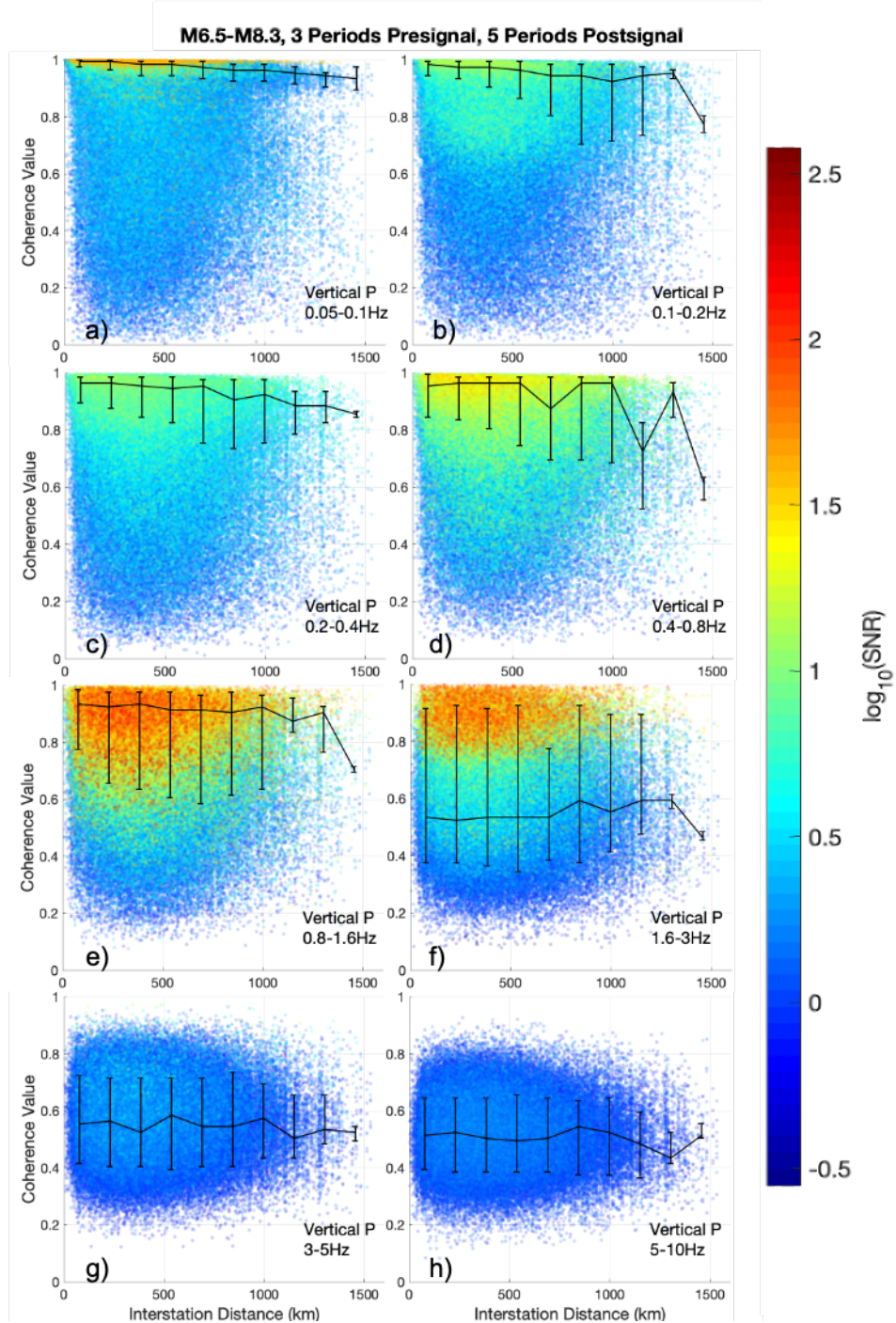


Figure 7: Coherence values produced by teleseismic vertical P waves recorded on the regional NEUSSEC array versus interstation distance and \log_{10} of the ambient SNR. Each subplot is labeled to indicate a) 0.05-0.1 Hz, b) 0.1-0.2 Hz, c) 0.2-0.4 Hz, d) 0.4-0.8 Hz, e) 0.8-1.6 Hz, f) 1.6-3 Hz, g) 3-5 Hz, h) 5-10 Hz. Indicated by error bars are the peak coherence values for each of 10 equally sized bins of interstation distance as well as the two half peak coherence values. The black line drawn through the error bars connect the peak coherence value for each interstation distance bin.

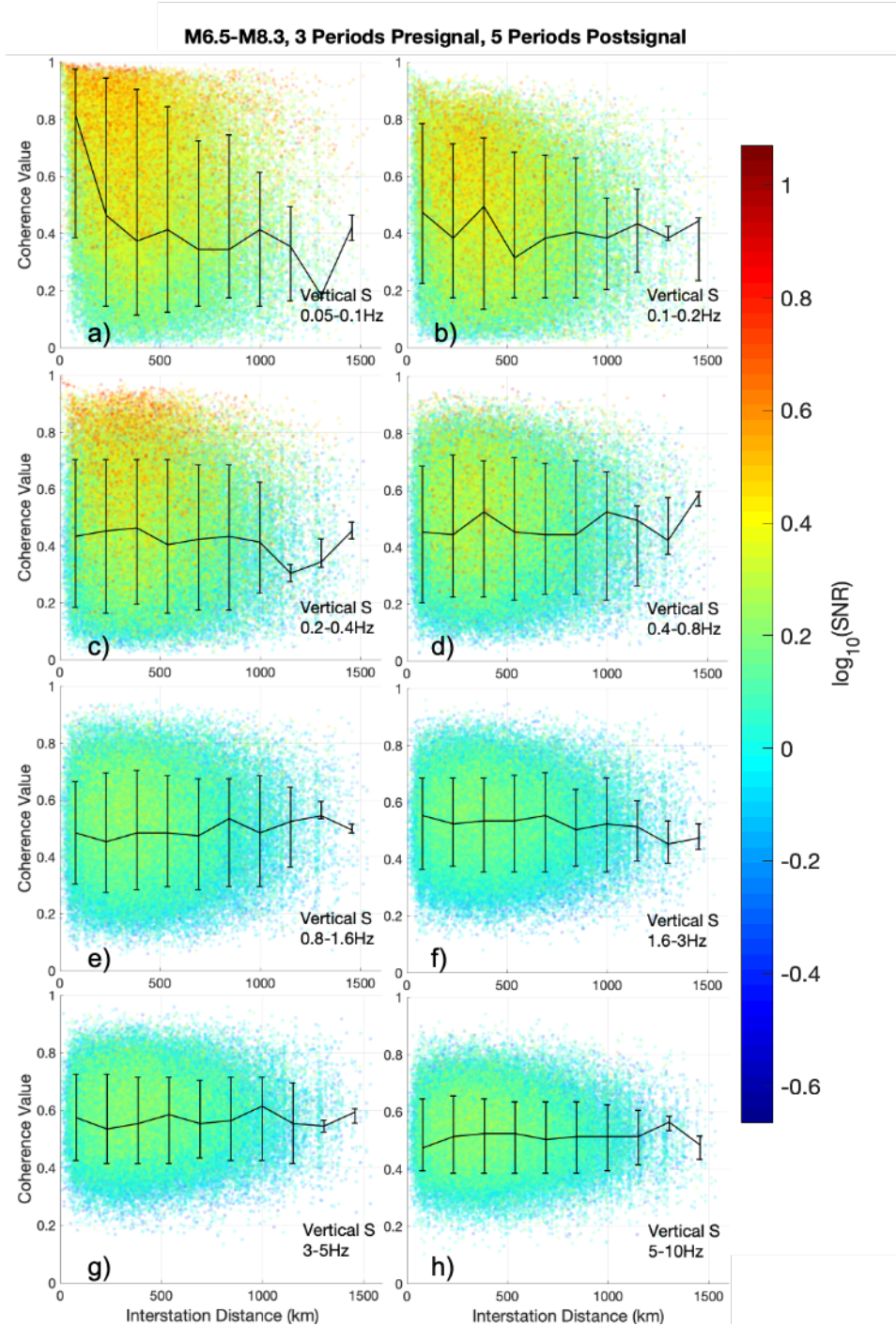


Figure 8: Coherence values produced by teleseismic vertical S waves recorded on the regional NEUSSEC array vs interstation distance and \log_{10} of the ambient SNR. Each subplot is labeled to indicate a) 0.05-0.1 Hz, b) 0.1-0.2 Hz, c) 0.2-0.4 Hz, d) 0.4-0.8 Hz, e) 0.8-1.6 Hz, f) 1.6-3 Hz, g) 3-5 Hz, h) 5-10 Hz. Indicated by error bars are the peak coherence values for each of 10 equally sized bins of interstation distance as well as the two half peak coherence values. The black line drawn through the error bars connect the peak coherence value for each interstation distance bin.

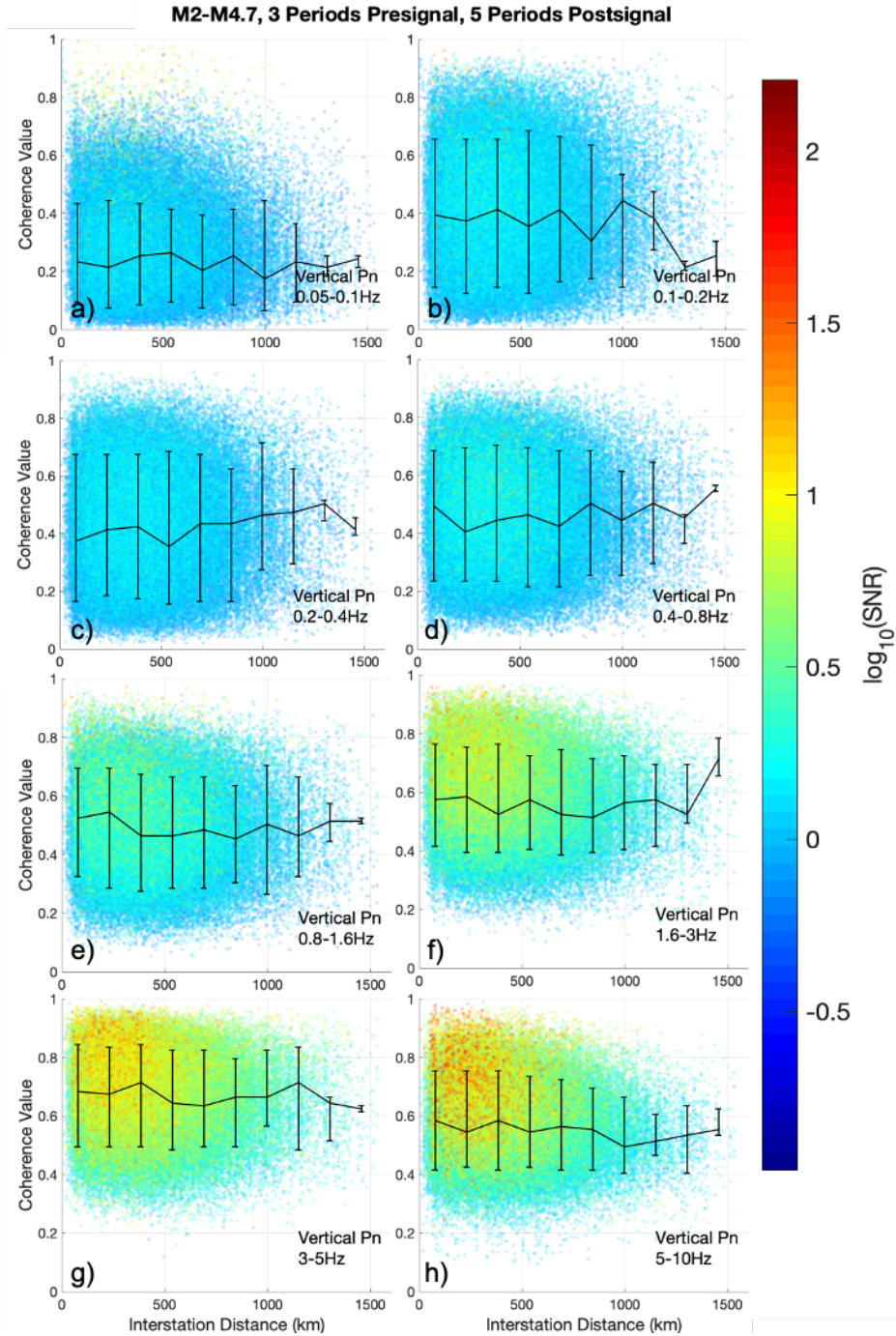


Figure 9: Coherence values produced by regional vertical Pn waves recorded on the regional NEUSSEC array vs interstation distance and \log_{10} of the ambient SNR. Each subplot is labeled to indicate a) 0.05-0.1 Hz, b) 0.1-0.2 Hz, c) 0.2-0.4 Hz, d) 0.4-0.8 Hz, e) 0.8-1.6 Hz, f) 1.6-3 Hz, g) 3-5 Hz, h) 5-10 Hz. Indicated by error bars are the peak coherence values for each of 10 equally sized bins of interstation distance as well as the two half peak coherence values. The black line drawn through the error bars connect the peak coherence value for each interstation distance bin.

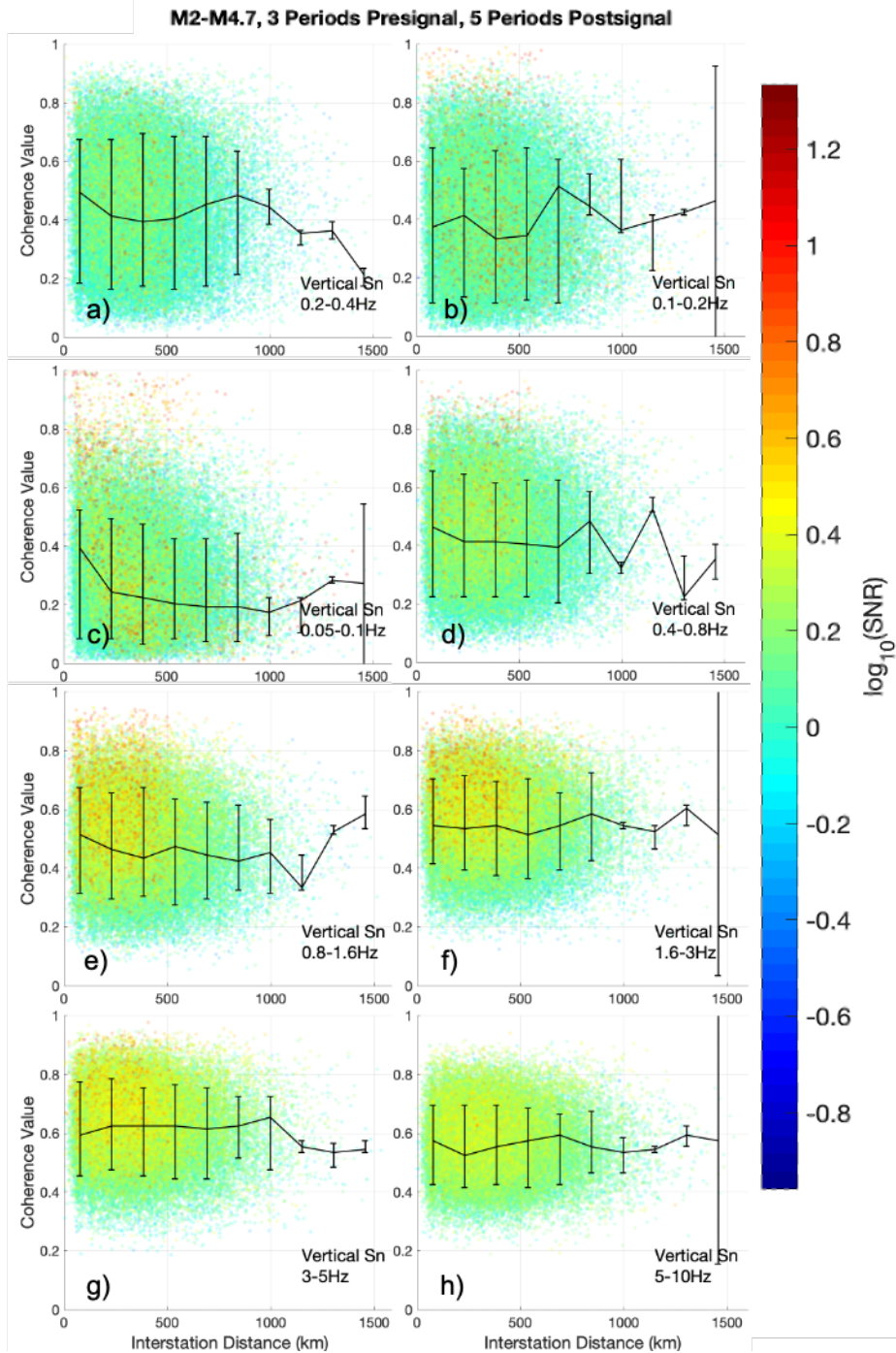


Figure 10: Coherence values produced by regional vertical Sn waves recorded on the regional NEUSSEC array vs interstation distance and \log_{10} of the ambient SNR. Each subplot is labeled to indicate a) 0.05-0.1 Hz, b) 0.1-0.2 Hz, c) 0.2-0.4 Hz, d) 0.4-0.8 Hz, e) 0.8-1.6 Hz, f) 1.6-3 Hz, g) 3-5 Hz, h) 5-10 Hz. Indicated by error bars are the peak coherence values for each of 10 equally sized bins of interstation distance as well as the two half peak coherence values. The black line drawn through the error bars connect the peak coherence value for each interstation distance bin.

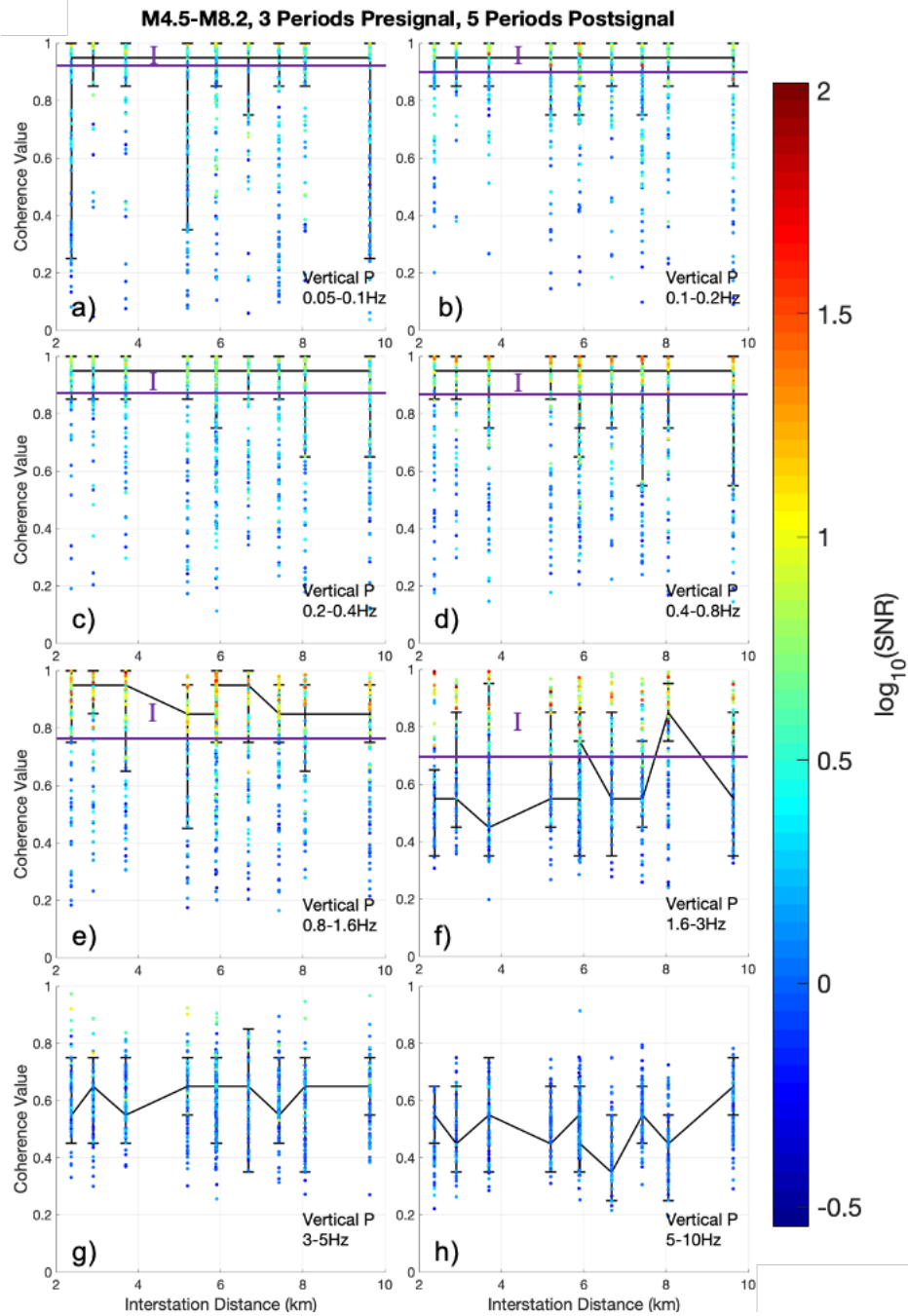


Figure 11: Coherence values produced by teleseismic vertical P waves recorded on the ALSA vs interstation distance and \log_{10} of the ambient SNR. Each subplot is labeled to indicate a) 0.05-0.1 Hz, b) 0.1-0.2 Hz, c) 0.2-0.4 Hz, d) 0.4-0.8 Hz, e) 0.8-1.6 Hz, f) 1.6-3 Hz, g) 3-5 Hz, h) 5-10 Hz. Indicated by error bars are the peak coherence values for each of the 10 interstation distances formed by the ALSA as well as the two half peak coherence values. The black line drawn through the error bars connect the peak coherence value for each interstation distance bin.

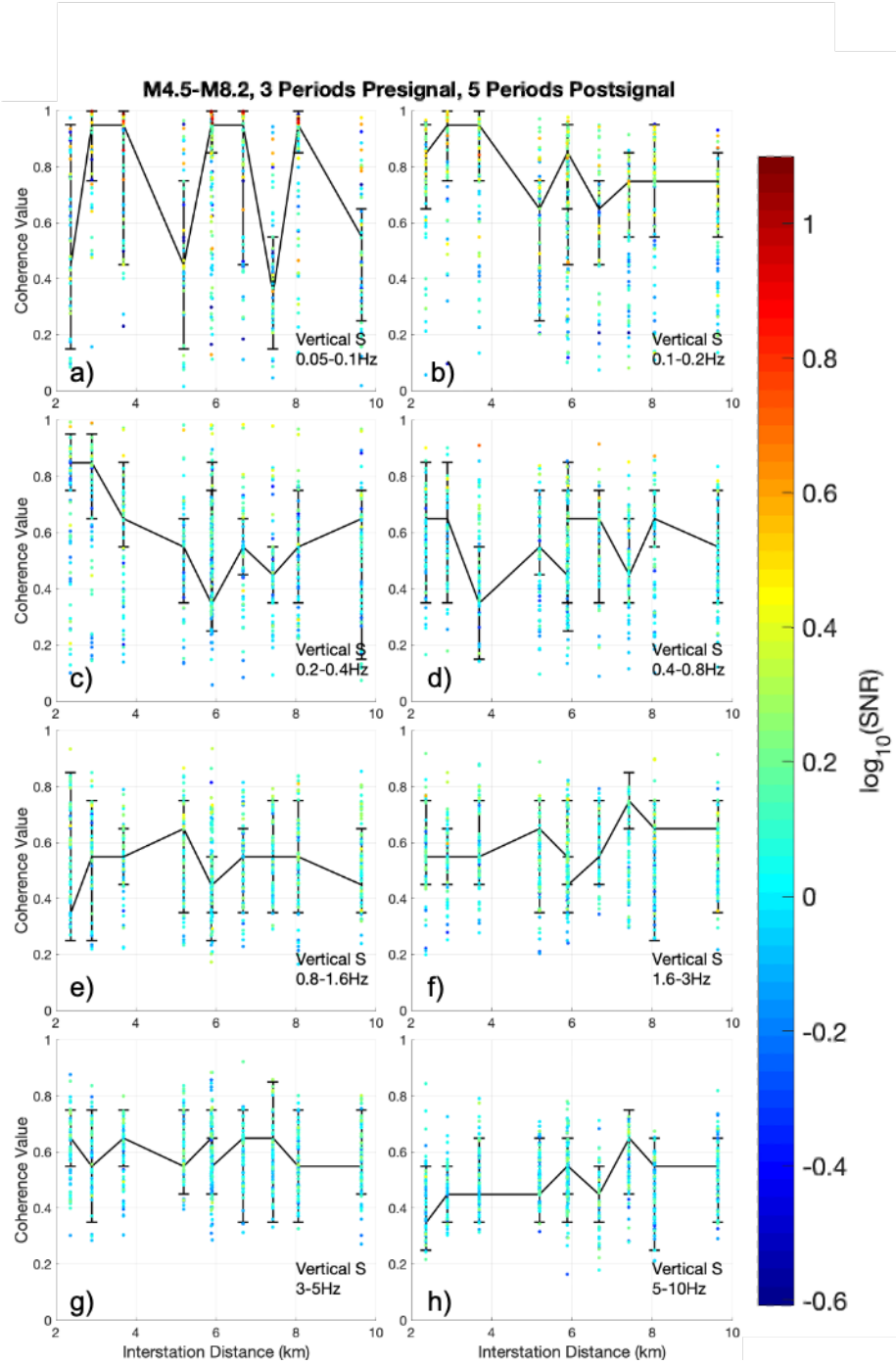


Figure 12: Coherence values produced by teleseismic vertical S waves recorded on the ALSA vs interstation distance and \log_{10} of the ambient SNR. Each subplot is labeled to indicate a) 0.05-0.1 Hz, b) 0.1-0.2 Hz, c) 0.2-0.4 Hz, d) 0.4-0.8 Hz, e) 0.8-1.6 Hz, f) 1.6-3 Hz, g) 3-5 Hz, h) 5-10 Hz. Indicated by error bars are the peak coherence values for each of the 10 interstation distances formed by the ALSA as well as the two half peak coherence values. The black line drawn through the error bars connect the peak coherence value for each interstation distance bin.

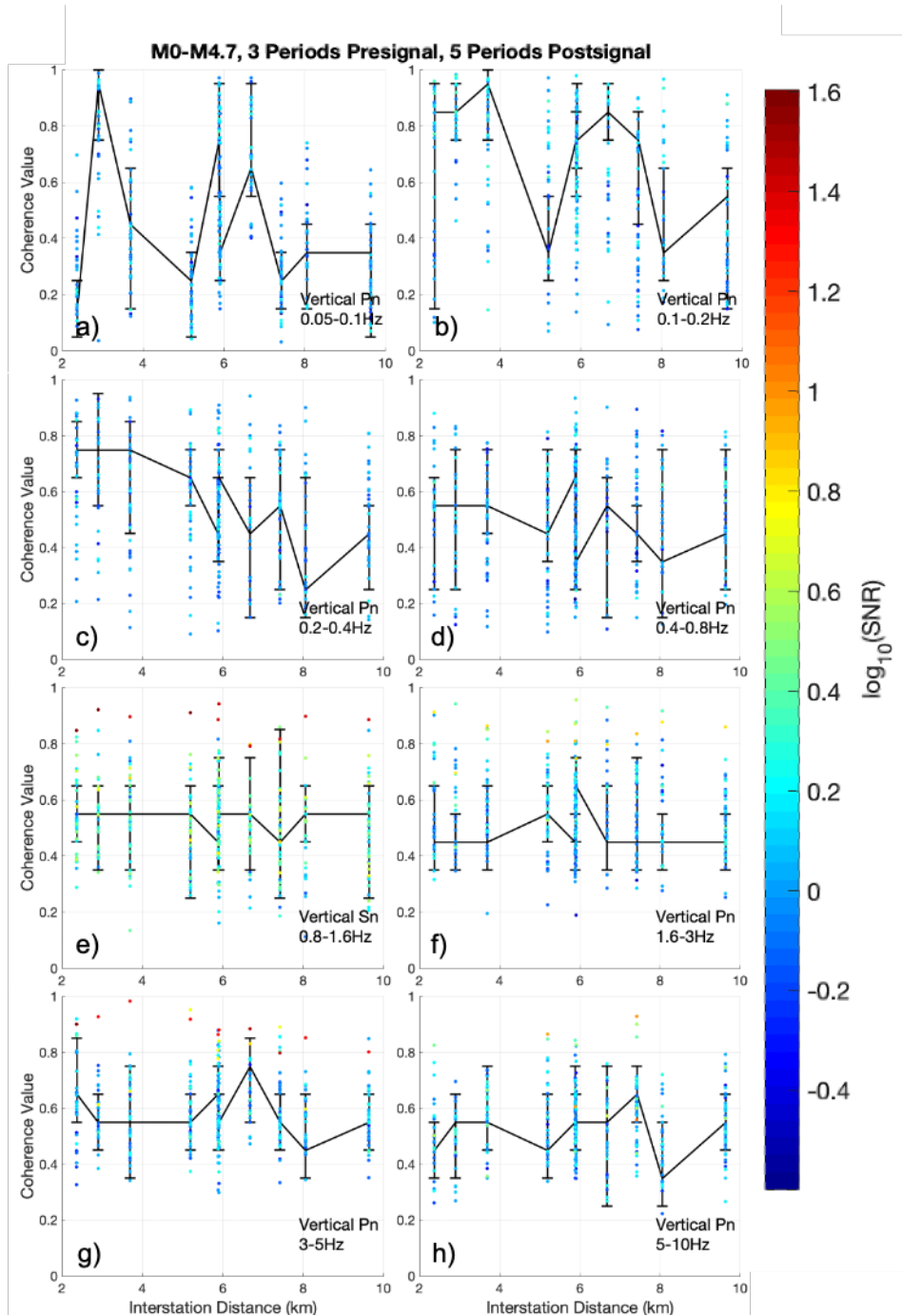


Figure 13: Coherence values produced by regional vertical Pn waves recorded on the ALSA vs interstation distance and \log_{10} of the ambient SNR. Each subplot is labeled to indicate a) 0.05-0.1 Hz, b) 0.1-0.2 Hz, c) 0.2-0.4 Hz, d) 0.4-0.8 Hz, e) 0.8-1.6 Hz, f) 1.6-3 Hz, g) 3-5 Hz, h) 5-10 Hz. Indicated by error bars are the peak coherence values for each of the 10 interstation distances formed by the ALSA as well as the two half peak coherence values. The black line drawn through the error bars connect the peak coherence value for each interstation distance bin.

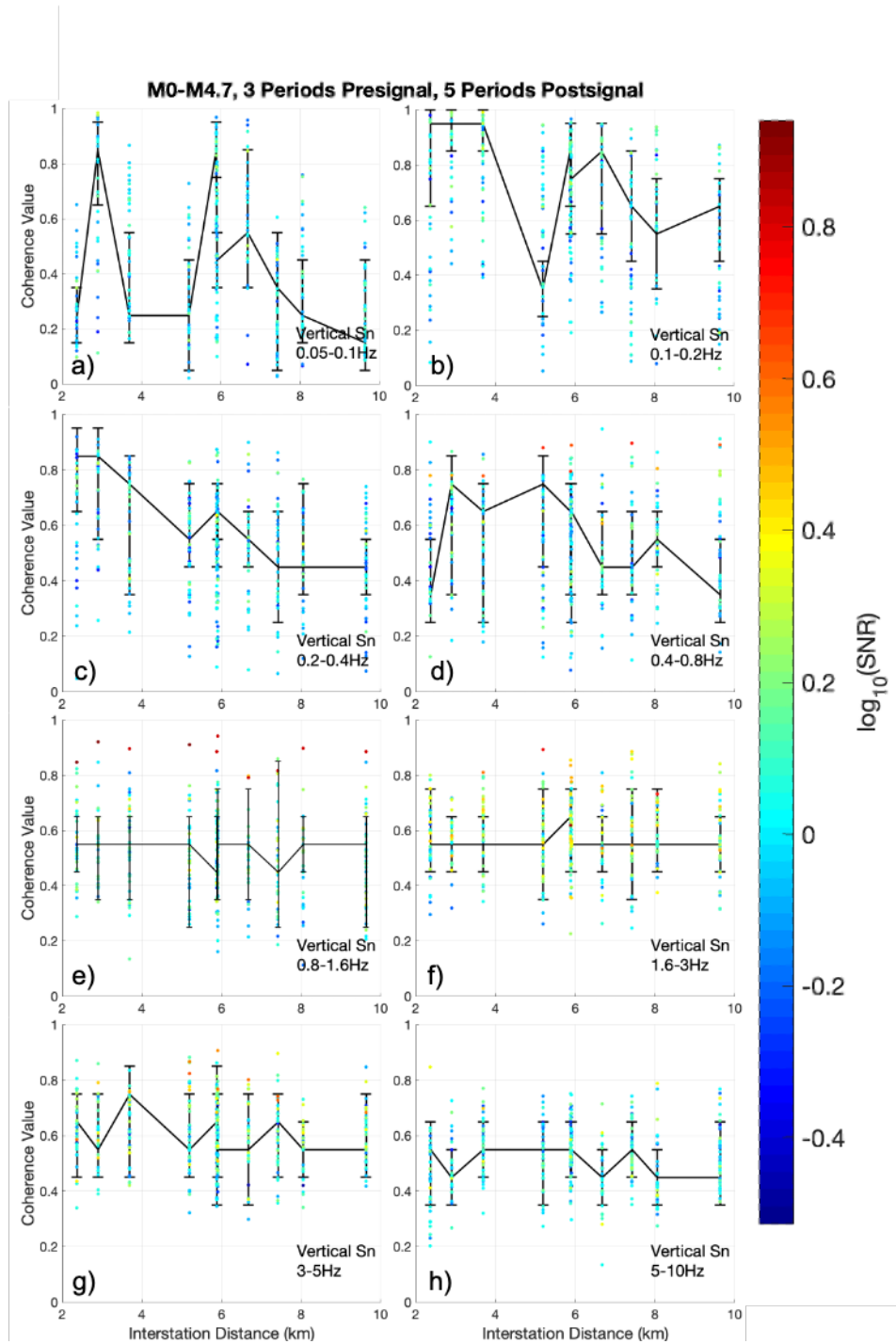


Figure 14: Coherence values produced by regional vertical Sn waves recorded on the ALSA vs interstation distance and \log_{10} of the ambient SNR. Each subplot is labeled to indicate a) 0.05-0.1 Hz, b) 0.1-0.2 Hz, c) 0.2-0.4 Hz, d) 0.4-0.8 Hz, e) 0.8-1.6 Hz, f) 1.6-3 Hz, g) 3-5 Hz, h) 5-10 Hz. Indicated by error bars are the peak coherence values for each of the 10 interstation distances formed by the ALSA as well as the two half peak coherence values. The black line drawn through the error bars connect the peak coherence value for each interstation distance bin.

8 Periods Presignal (Ambient Noise)

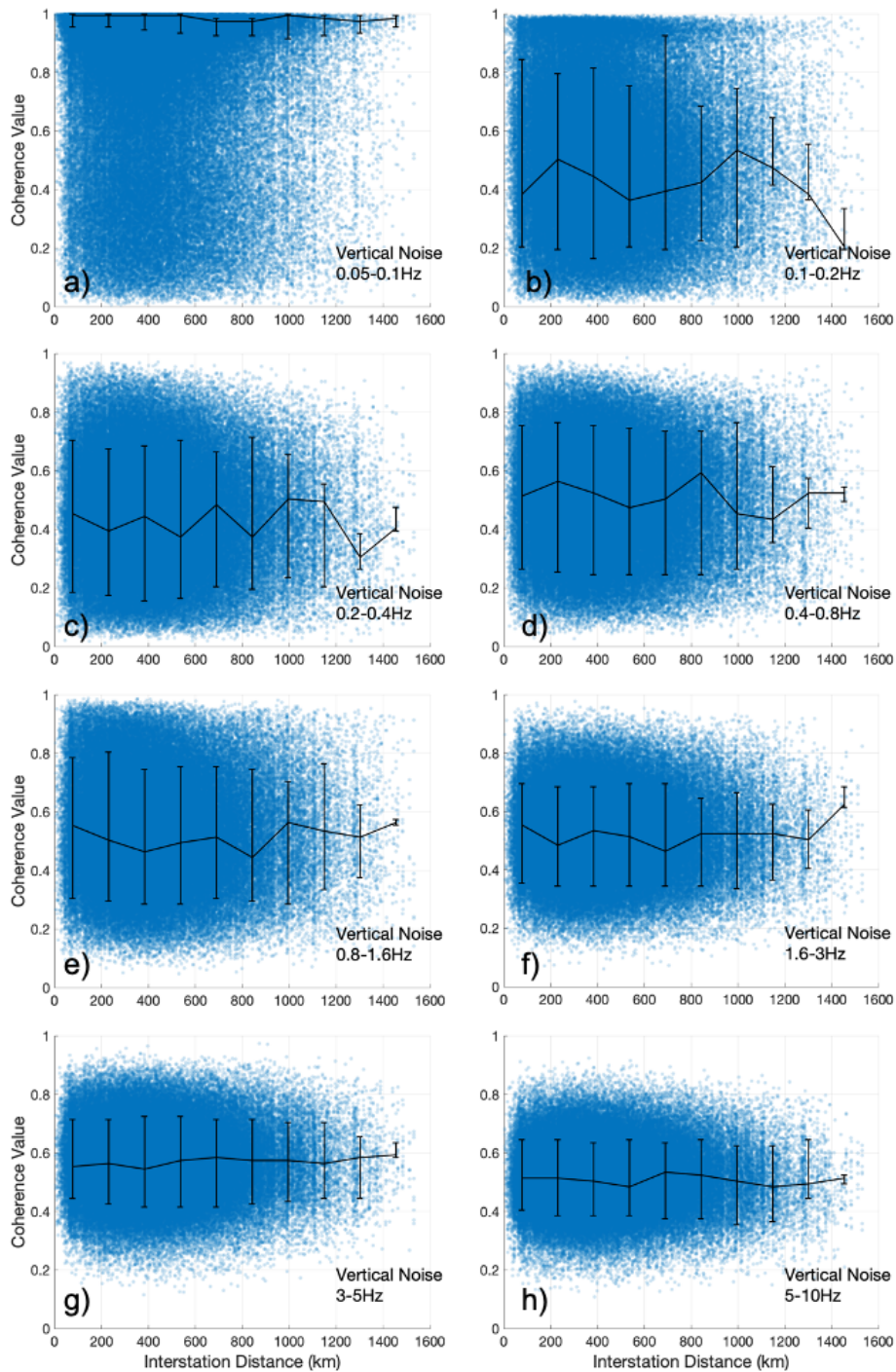


Figure 15: Coherence values produced by ambient noise recorded on the regional NEUSSEC array vs interstation distance. Each subplot is labeled to indicate a) 0.05-0.1 Hz, b) 0.1-0.2 Hz, c) 0.2-0.4 Hz, d) 0.4-0.8 Hz, e) 0.8-1.6 Hz, f) 1.6-3 Hz, g) 3-5 Hz, h) 5-10 Hz. Indicated by error bars are the peak coherence values for each of 10 equally sized bins of interstation distance as well as the two half peak coherence values. The black line drawn through the error bars connect the peak coherence value for each interstation distance bin.

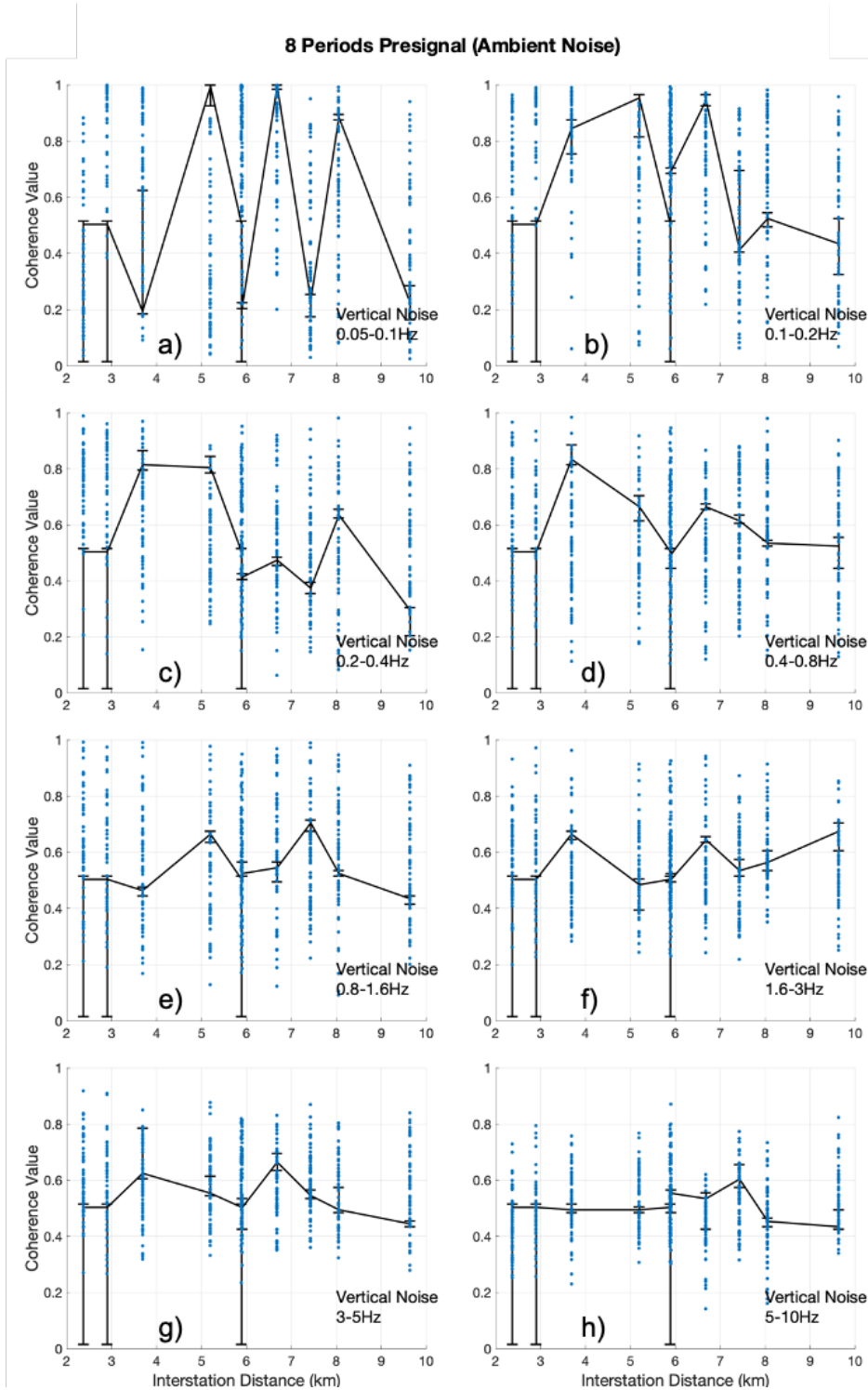


Figure 16: Coherence values produced by ambient noise recorded on the ALSA vs interstation distance. Each subplot is labeled to indicate a) 0.05-0.1 Hz, b) 0.1-0.2 Hz, c) 0.2-0.4 Hz, d) 0.4-0.8 Hz, e) 0.8-1.6 Hz, f) 1.6-3 Hz, g) 3-5 Hz, h) 5-10 Hz. Indicated by error bars are the peak coherence values for each of the 10 interstation distances formed by the ALSA as well as the two half peak coherence values. The black line drawn through the error bars connect the peak coherence value for each interstation distance bin.

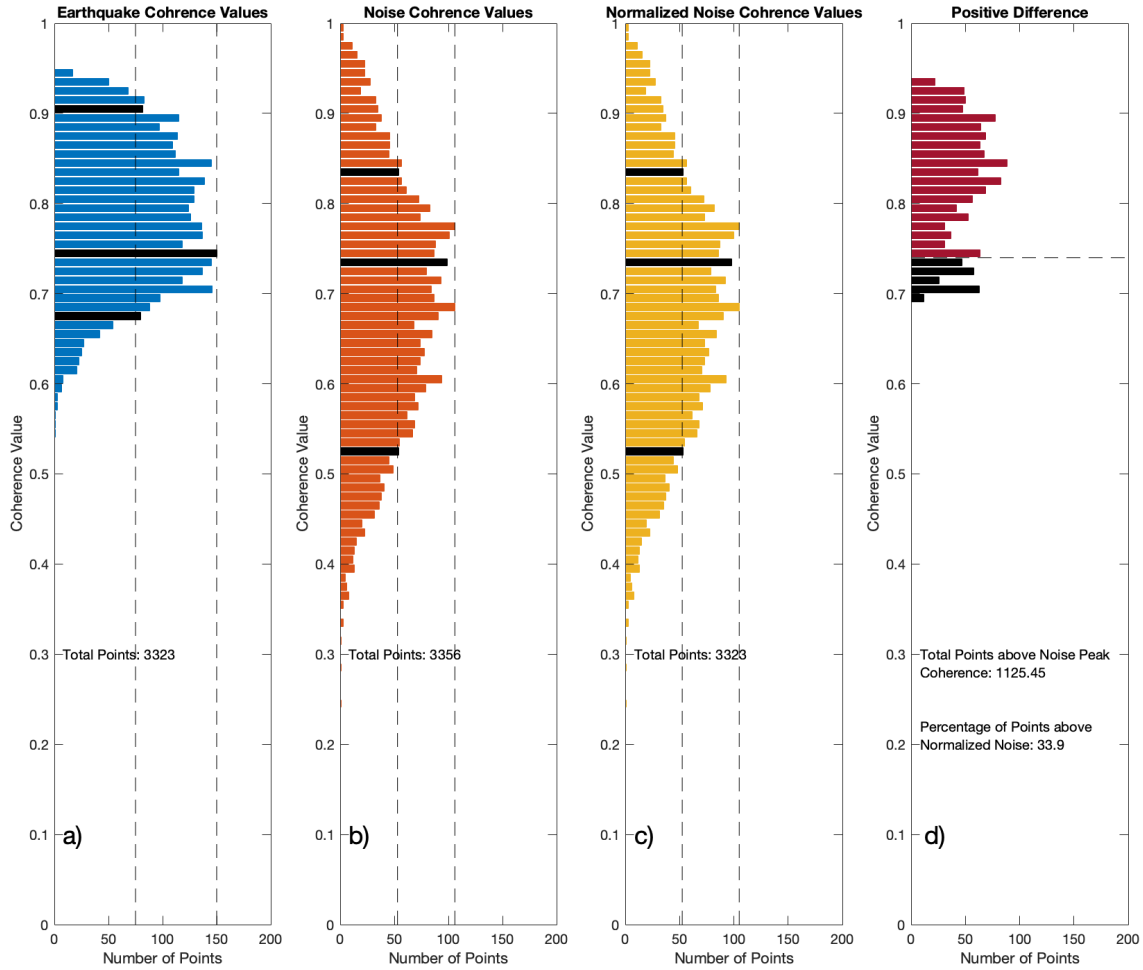


Figure 17: The methodology used to find the percent of coherence values within a single interstation distance bin for a data subset that must contain coherent body-wave energy and could not be produced purely by noise. The data points used here were generated solely for this figure and have no relationship to the results of this thesis. a) A histogram of earthquake coherence values C_{xy} for a single interstation distance bin and data subset. The peak and half peak coherence values are measured and displayed as in Figure 6. b) A histogram of noise coherence values C_{xy} produced for the same interstation distance bin as the earthquake coherence values. The peak and half peak coherence values are measured and displayed as in Figure 6. c) The histogram of noise coherence values is normalized to the earthquake coherence histogram. The number of normalized noise coherence values is equal to the number of earthquake coherence values. Each normalized noise coherence bin may contain a non-integer number of coherence values. d) The normalized histogram of noise coherence values is subtracted from the histogram of earthquake coherence values to obtain the difference. Negative values and values that fall below the peak coherence value of the noise (indicated in black) are set to 0. This number is divided by the total number of earthquake coherence values to obtain the percentage of coherence values within that data subset and interstation distance bin that must contain coherent body-wave energy.

**Percentage of Coherence Values Above Coherence Values of Noise:
Teleseismic P Waves on the Regional Array**

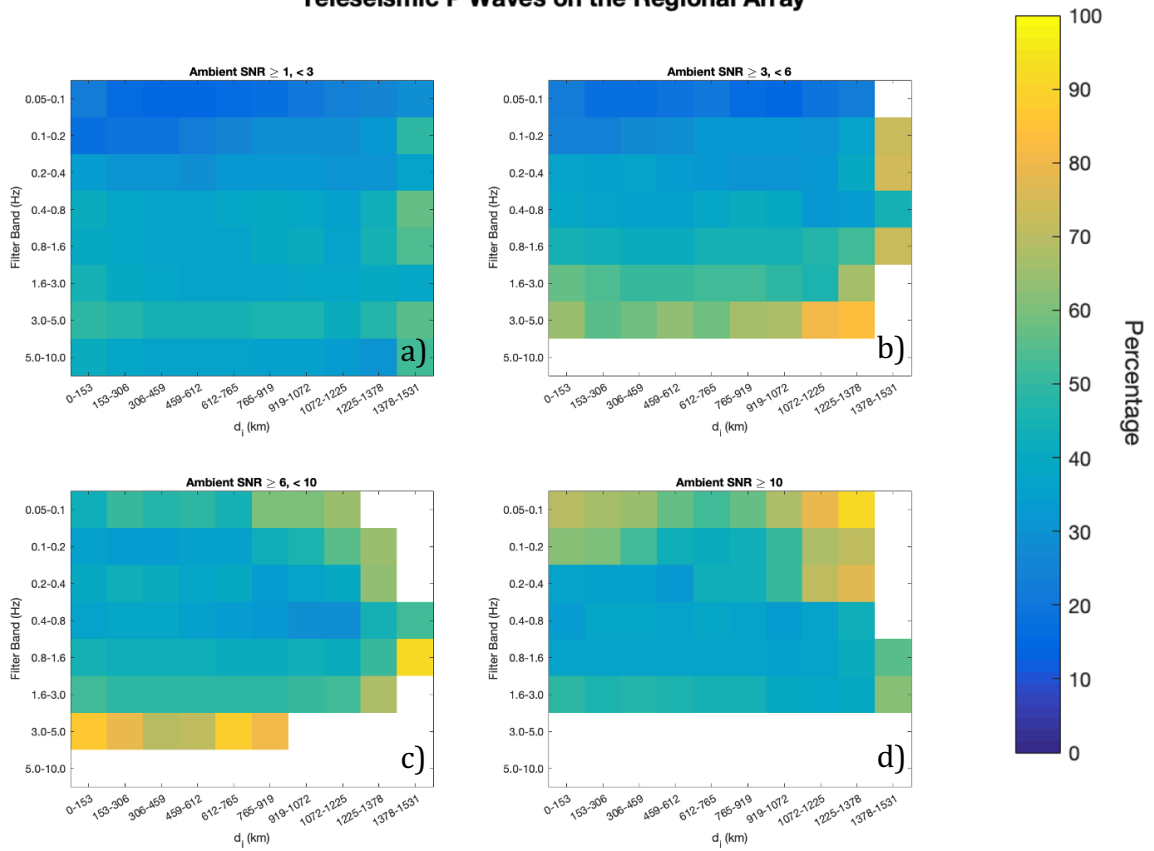


Figure 18: Coherent Body-Wave Percentages vs interstation distance bin and frequency for teleseismic P waves recorded on the regional array and ambient SNRs between a) 1-3, b) 3-6, c) 6-10 and d) 10 and above. White areas indicate interstation distances and filter bands where no coherence data were available for waveforms within the given bounds of ambient SNR.

**Percentage of Coherence Values Above Coherence Values of Noise:
Teleseismic S Waves on the Regional Array**

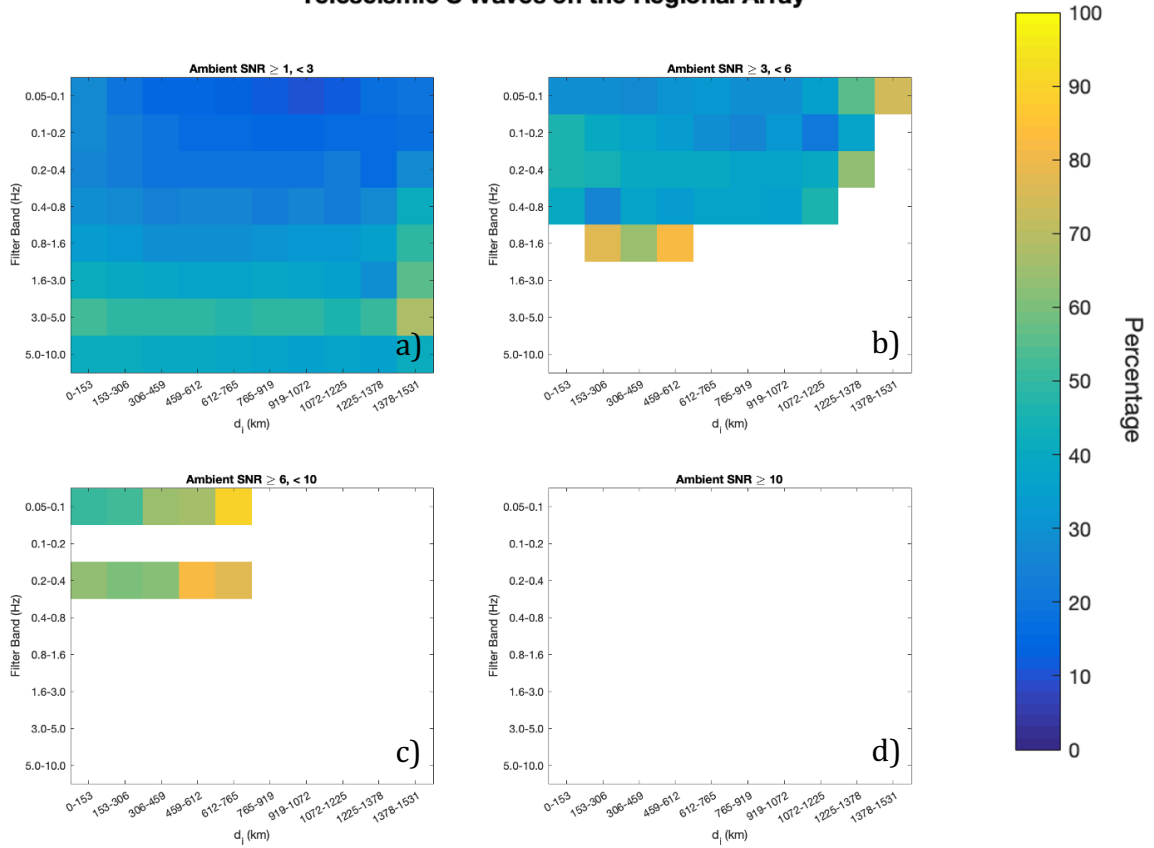


Figure 19: Coherent Body-Wave Percentages vs interstation distance bin and frequency for teleseismic S waves recorded on the regional array and ambient SNRs between a) 1-3, b) 3-6, c) 6-10 and d) 10 and above. White areas indicate interstation distances and filter bands where no coherence data were available for waveforms within the given bounds of ambient SNR.

**Percentage of Coherence Values Above Coherence Values of Noise:
Regional Pn Waves on the Regional Array**

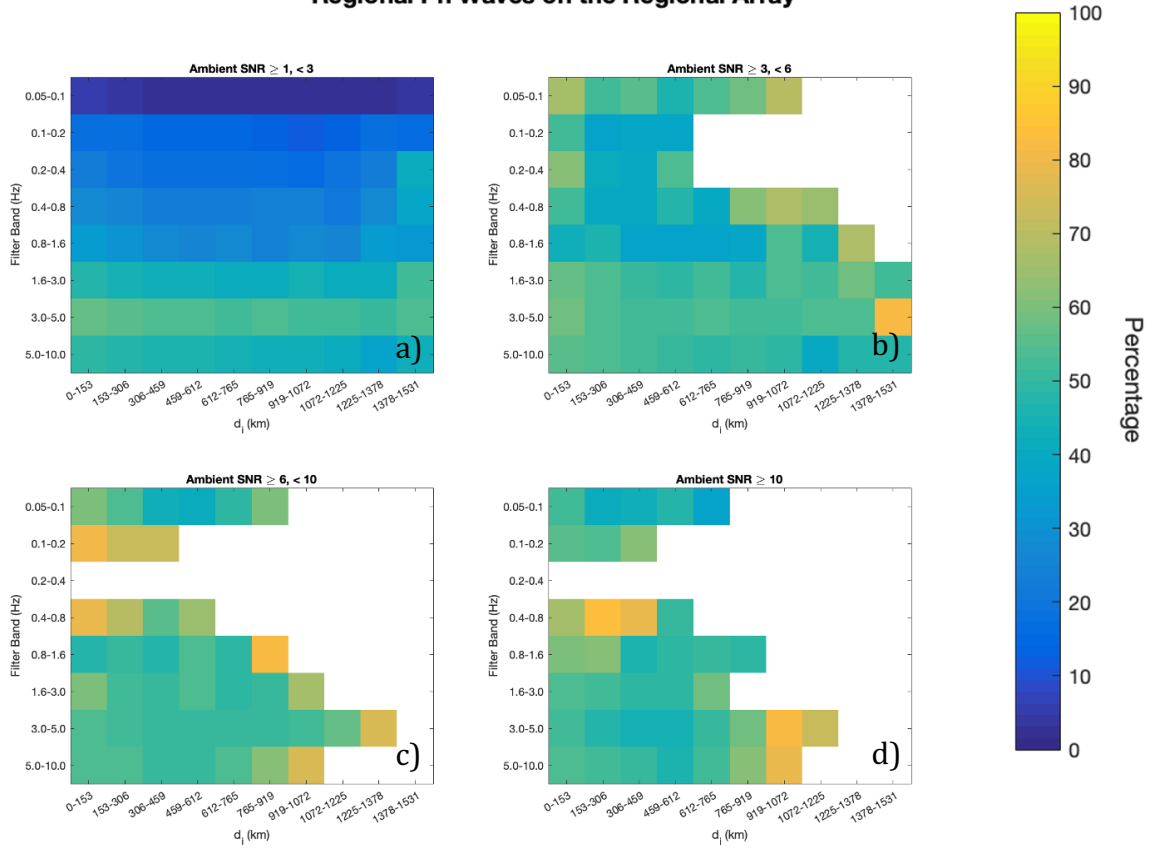


Figure 20: Coherent Body-Wave Percentages vs interstation distance bin and frequency for regional Pn waves recorded on the regional array and ambient SNRs between a) 1-3, b) 3-6, c) 6-10 and d) 10 and above. White areas indicate interstation distances and filter bands where no coherence data were available for waveforms within the given bounds of ambient SNR.

**Percentage of Coherence Values Above Coherence Values of Noise:
Regional Sn Waves on the Regional Array**

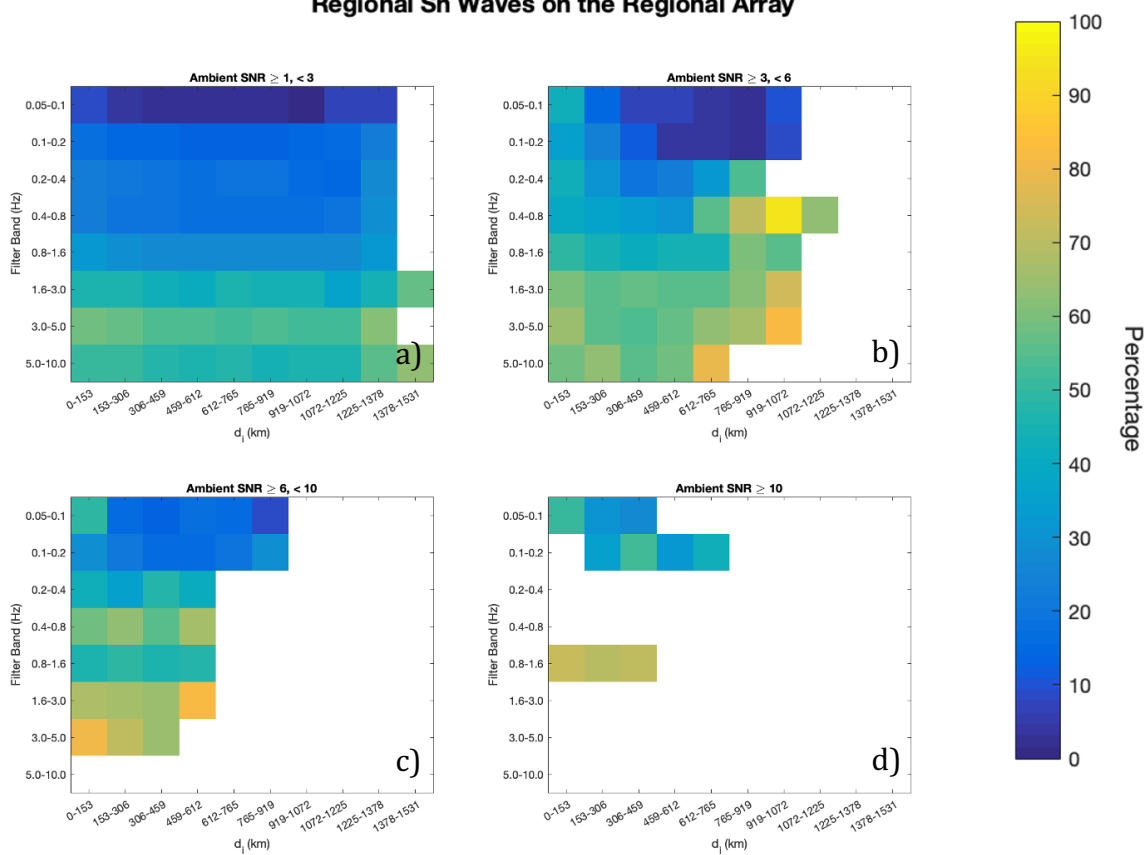


Figure 21: Coherent Body-Wave Percentages vs interstation distance bin and frequency for regional Sn waves recorded on the regional array and ambient SNRs between a) 1-3, b) 3-6, c) 6-10 and d) 10 and above. White areas indicate interstation distances and filter bands where no coherence data were available for waveforms within the given bounds of ambient SNR.

**Percentage of Coherence Values Above Coherence Values of Noise:
Teleseismic P Waves on the ALSA**

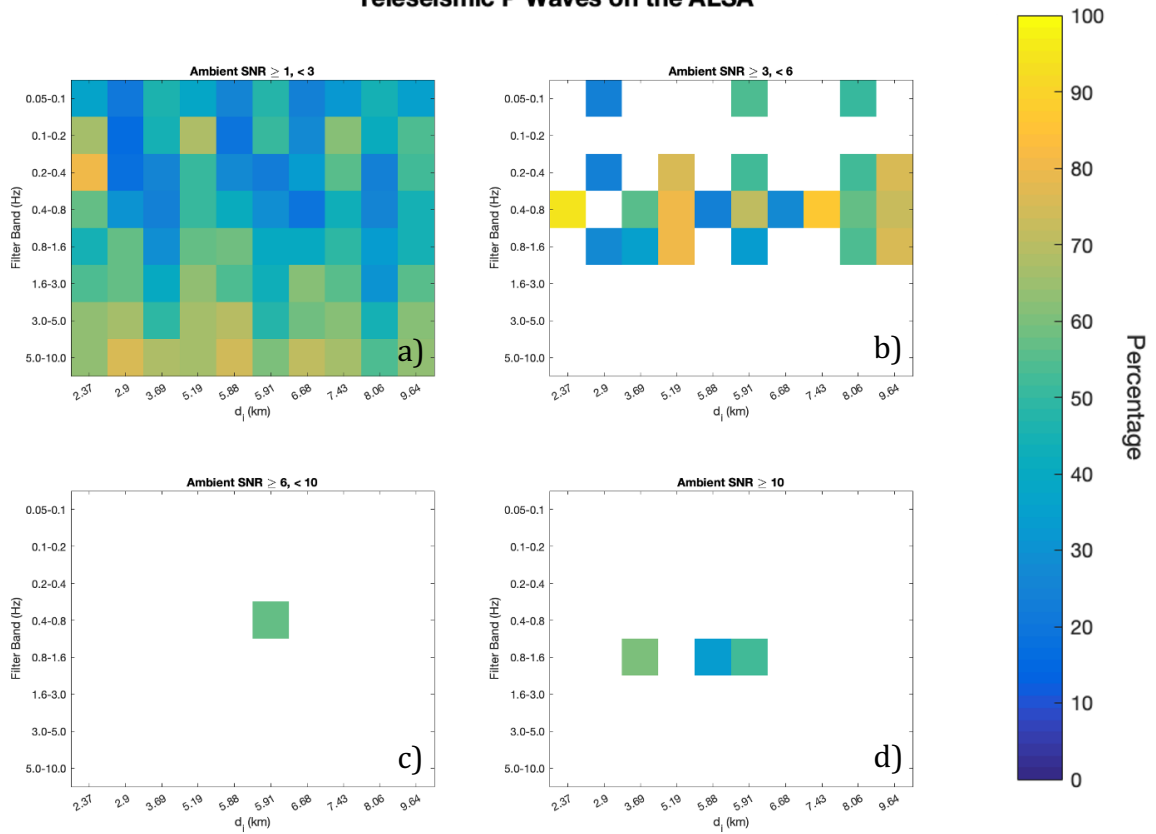


Figure 22: Coherent Body-Wave Percentages vs interstation distance bin and frequency for teleseismic P waves recorded on the ALSA and ambient SNRs between a) 1-3, b) 3-6, c) 6-10 and d) 10 and above. White areas indicate interstation distances and filter bands where no coherence data were available for waveforms within the given bounds of ambient SNR.

**Percentage of Coherence Values Above Coherence Values of Noise:
Teleseismic S Waves on the ALSA**

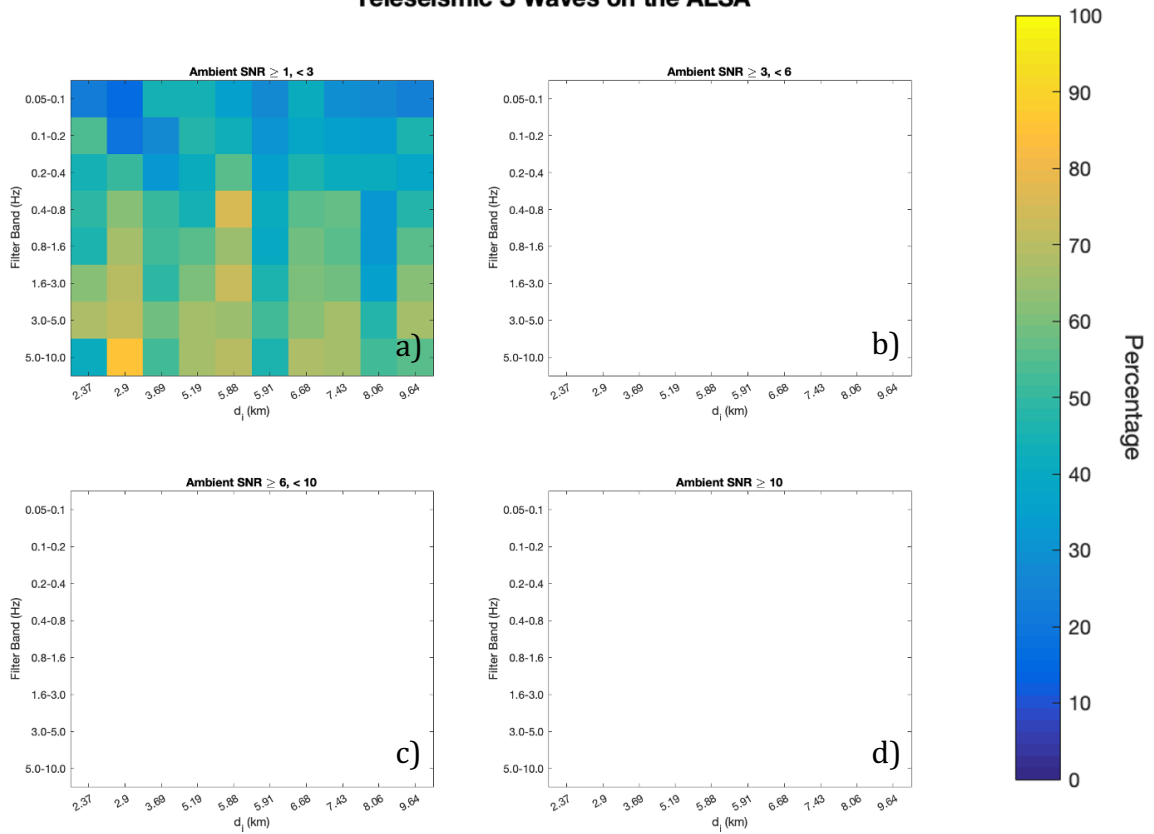


Figure 23: Coherent Body-Wave Percentages vs interstation distance bin and frequency for teleseismic S waves recorded on the ALSA and ambient SNRs between a) 1-3, b) 3-6, c) 6-10 and d) 10 and above. White areas indicate interstation distances and filter bands where no coherence data were available for waveforms within the given bounds of ambient SNR.

**Percentage of Coherence Values Above Coherence Values of Noise:
Regional Pn Waves on the ALSA**

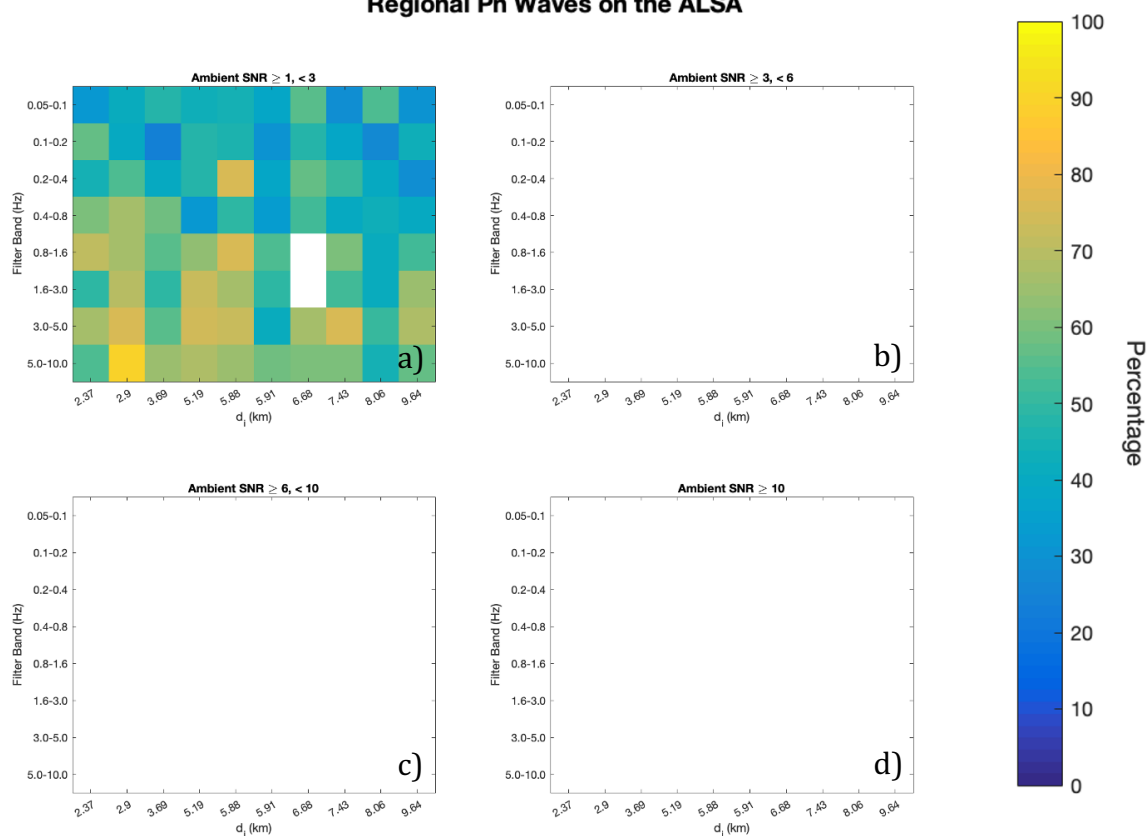


Figure 24: Coherent Body-Wave Percentages vs interstation distance bin and frequency for regional Pn waves recorded on the ALSA and ambient SNRs between a) 1-3, b) 3-6, c) 6-10 and d) 10 and above. White areas indicate interstation distances and filter bands where no coherence data were available for waveforms within the given bounds of ambient SNR.

**Percentage of Coherence Values Above Coherence Values of Noise:
Regional Sn Waves on the ALSA**

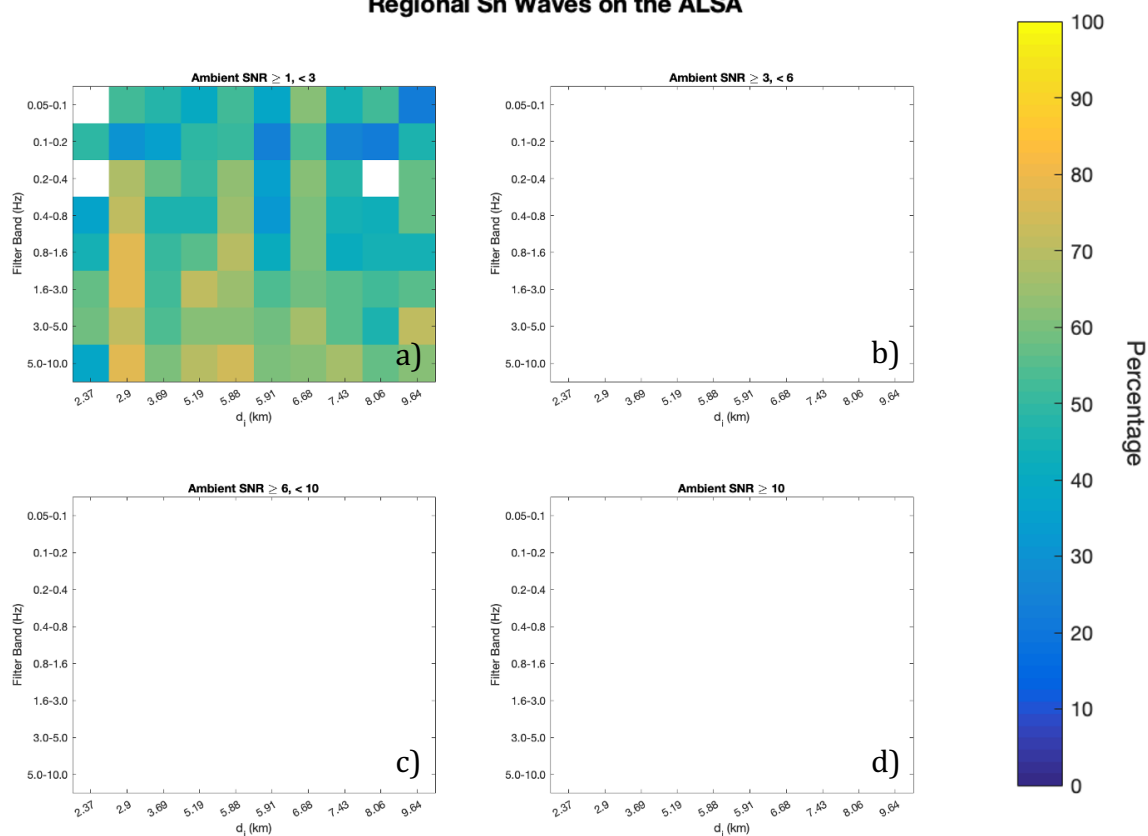


Figure 25: Coherent Body-Wave Percentages vs interstation distance bin and frequency for regional Sn waves recorded on the ALSA and ambient SNRs between a) 1-3, b) 3-6, c) 6-10 and d) 10 and above. White areas indicate interstation distances and filter bands where no coherence data were available for waveforms within the given bounds of ambient SNR.

Percent of Coherence Values Greater Than Noise Coherence Distribution vs Frequency

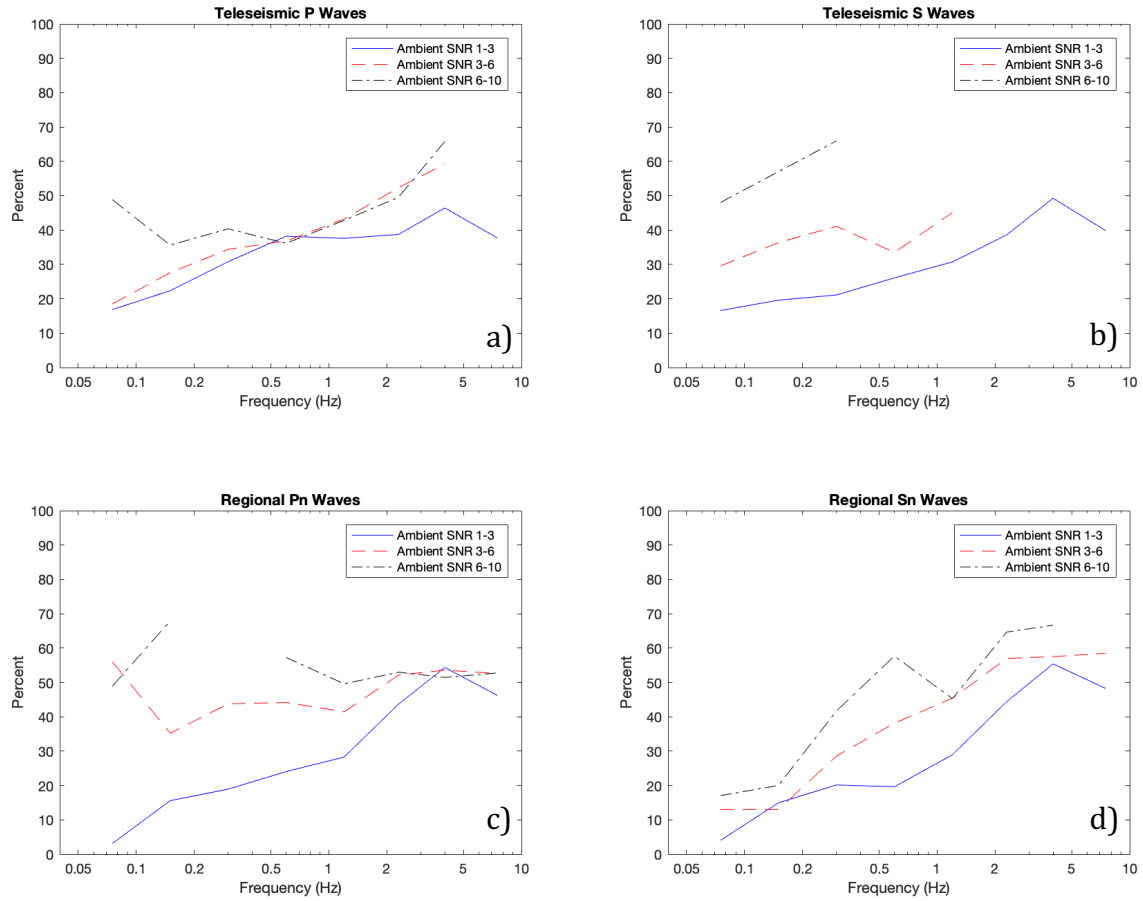


Figure 26: Coherent Body-Wave Percentages versus frequency and ambient SNR for a) teleseismic P waves, b) teleseismic S waves, c) regional Pn waves and d) regional Sn waves.

TABLES

	$f < 1$ Hz (km)	$f > 1$ Hz (km)
$m_n < 3$	0	100
$3 \leq m_n < 3.5$	80	200
$3.5 \leq m_n < 4$	100	400
$4 \leq m_n < 4.5$	200	800
$4.5 \leq m_n < 5$	800	2000

Table 1. Distance limits out to which NEUSSEC earthquake signal amplitudes are large enough to be recorded by receivers independent of noise levels. From Table 1 of Atkinson [2004].

Network	Station	Channel	Latitude	Longitude	Elevation	SampleRate	StartTime	EndTime
CN	A11	HHZ	47.243099	-70.1968	201	100	2000-09-16T16:33:00	2016-08-08T19:07:00
CN	A16	HHZ	47.467999	-70.009598	13	100	2000-09-13T00:00:00	2016-08-08T19:07:00
CN	A21	HHZ	47.704498	-69.689201	47	100	2000-09-10T00:01:00	2016-10-01T16:50:00
CN	A54	HHZ	47.456799	-70.413399	377	100	2000-10-08T16:21:00	2016-08-08T19:07:00
CN	A61	HHZ	47.6936	-70.0914	380	100	2000-10-08T16:21:00	2016-10-04T20:00:00
CN	A64	HHZ	47.8274	-69.891403	132	100	2000-10-11T18:46:00	2016-10-03T18:00:00
CN	BACQ	HHZ	49.291199	-68.163399	69	100	2015-10-24T13:40:00	2599-12-31T23:59:59
CN	BCLQ	HHZ	46.9263	-71.172798	167.6	100	2009-11-06T13:00:00	2017-06-28T17:38:00
CN	BECQ	HHZ	46.344898	-72.482903	24	100	2012-03-07T20:00:00	2599-12-31T23:59:59
CN	BSCQ	HHZ	48.123501	-69.7164	2	100	2015-10-20T17:30:00	2599-12-31T23:59:59
CN	FORQ	HHZ	48.7542	-69.113503	6	100	2015-10-22T19:26:00	2599-12-31T23:59:59
CN	GAC	BHZ	45.703201	-75.4776	167.2	40	2013-01-01T00:00:00	2016-01-01T00:00:00
CN	ICQ	BHZ	49.522301	-67.2715	58	40	2013-01-01T00:00:00	2016-01-01T00:00:00
CN	KILO	HHZ	48.4972	-79.723198	314	100	2009-05-29T17:28:00	2017-06-13T16:00:00
CN	KGNO	BHZ	44.2272	-76.493401	89	40	2013-01-01T00:00:00	2015-05-13T15:30:00
CN	LDSQ	HHZ	45.7127	-76.346901	257	100	2013-05-17T14:00:00	2013-11-01T17:00:00
CN	LESQ	HHZ	48.319901	-69.4132	17	100	2015-10-21T14:28:00	2599-12-31T23:59:59
CN	LMQ	HHZ	47.5485	-70.325798	455	100	2012-05-01T10:00:00	2016-10-04T13:20:00
CN	MCA4	HHZ	45.598301	-67.326698	90	100	2012-04-26T16:00:00	2013-01-11T22:00:00
CN	MGDQ	HHZ	45.718899	-75.485397	141	100	2011-11-22T18:17:00	2013-07-05T15:30:00
CN	MNTQ	BHZ	45.500301	-73.622803	112	40	2013-01-01T00:00:00	2016-01-01T00:00:00
CN	ORIO	HHZ	45.4515	-75.511002	74	100	2008-06-19T17:00:00	2016-12-01T16:12:00
CN	OTT	HHZ	45.394199	-75.716698	77	100	2002-04-23T18:05:00	2017-10-02T19:38:00
CN	SADO	BHZ	44.769501	-79.141098	228	40	2013-01-01T00:00:00	2016-01-01T00:00:00
CN	SMCQ	HHZ	46.670898	-72.055099	47	100	2009-11-04T15:00:00	2015-07-24T16:00:00
CN	STFQ	HHZ	46.553799	-71.543602	122.8	100	2011-12-13T20:44:00	2599-12-31T23:59:59
CN	STUQ	HHZ	46.301601	-73.094597	63.7	100	2011-12-18T10:27:00	2016-04-27T17:00:00
CN	TRQ	HHZ	46.217602	-74.5513	860	100	2015-09-02T20:45:00	2017-08-09T14:48:00
CN	VABQ	HHZ	45.904701	-75.607903	210	100	2010-11-29T10:00:00	2018-05-18T15:45:00
CN	VLDQ	BHZ	48.190102	-77.757202	316	40	2013-01-01T00:00:00	2016-01-01T00:00:00
IU	HRV	HHZ	42.506401	-71.558296	200	100	2009-12-17T06:02:00	2016-04-27T17:00:00
IU	SSPA	HHZ	40.635799	-77.887604	270	100	2012-08-31T05:59:00	2017-09-23T22:30:00
LD	ACCN	HHZ	43.3843	-73.667801	340	100	2010-12-03T00:00:00	2599-12-31T23:59:59

LD	BMNY	HHZ	44.83987	-74.5065	115	100	2011-07-29T00:00:00	2599-12-31T23:59:59
LD	BNY	HHZ	42.089321	-75.970894	292	100	2015-10-13T15:00:00	2599-12-31T23:59:59
LD	BRNJ	HHZ	40.682693	-74.565742	50	100	2010-12-29T00:00:00	2016-02-19T17:00:00
LD	BRNY	HHZ	41.414036	-74.011887	248	100	2010-12-29T20:15:00	2016-02-02T16:00:00
LD	CCNY	HHZ	42.927319	-78.855103	194	100	2013-12-05T00:00:00	2018-05-04T13:42:00
LD	CFNY	HHZ	44.16515	-75.051353	461	100	2015-10-08T00:00:00	2599-12-31T23:59:59
LD	CGNY	HHZ	42.81654	-75.532356	385	100	2015-12-09T00:00:00	2599-12-31T23:59:59
LD	CPNY	HHZ	40.7911	-73.960197	27	100	2011-01-14T00:00:00	2599-12-31T23:59:59
LD	CUNY	HHZ	40.734928	-73.817612	20	100	2010-11-23T15:30:00	2599-12-31T23:59:59
LD	FLET	HHZ	44.722504	-72.952148	336	100	2011-07-07T00:00:00	2599-12-31T23:59:59
LD	FMPA	HHZ	40.047798	-76.320801	121	100	2011-03-17T16:00:00	2016-09-30T00:00:00
LD	FOR	HHZ	40.860298	-73.885201	0	100	2010-11-19T20:00:00	2599-12-31T23:59:59
LD	FRNY	HHZ	44.834999	-73.588303	242	100	2010-10-27T11:00:00	2599-12-31T23:59:59
LD	HBVT	HHZ	44.36306	-73.063263	349	100	2011-07-19T00:00:00	2599-12-31T23:59:59
LD	HCNY	HHZ	42.6968	-74.398399	273	100	2011-02-17T17:00:00	2599-12-31T23:59:59
LD	KSCT	HHZ	41.72612	-73.484253	114	100	2011-11-16T00:00:00	2599-12-31T23:59:59
LD	KSPA	HHZ	41.557037	-75.768181	298	100	2012-05-02T00:00:00	2599-12-31T23:59:59
LD	LUPA	HHZ	40.598701	-75.371803	255	100	2011-11-30T00:00:00	2599-12-31T23:59:59
LD	MCVT	HHZ	43.953671	-72.991753	439	100	2011-08-04T00:00:00	2599-12-31T23:59:59
LD	MMNY	HHZ	42.731682	-77.906532	241	100	2010-11-16T00:00:00	2016-04-22T12:30:00
LD	MSNJ	HHZ	40.884106	-74.181534	132	100	2011-03-26T00:00:00	2599-12-31T23:59:59
LD	NCB	HHZ	43.9734	-74.222801	575	100	2011-05-03T22:00:00	2599-12-31T23:59:59
LD	NPNY	HHZ	41.754589	-74.143539	216	100	2010-12-29T00:00:00	2599-12-31T23:59:59
LD	ODNJ	HHZ	41.082901	-74.605598	187	100	2011-03-08T18:00:00	2599-12-31T23:59:59
LD	PAL	HHZ	41.0056	-73.907898	66	100	2009-04-24T00:00:00	2599-12-31T23:59:59
LD	PANJ	HHZ	40.3769	-74.702904	100	100	2010-12-29T00:00:00	2018-07-19T23:00:00
LD	POTS	HHZ	44.663399	-74.973198	112.1	100	2006-05-22T00:00:00	2015-07-15T00:00:00
LD	PRNY	HHZ	42.466537	-76.536079	248	100	2011-04-28T18:00:00	2016-01-14T17:00:00
LD	PTNY	HHZ	44.5578	-74.950798	275	100	2015-07-16T00:00:00	2599-12-31T23:59:59
LD	TRNY	HHZ	41.145	-74.224426	270	100	2014-09-04T00:00:00	2599-12-31T23:59:59
LD	TUPA	HHZ	40.166248	-75.186417	112	100	2011-03-10T21:00:00	2599-12-31T23:59:59
LD	UCCT	HHZ	41.794323	-72.225548	200	100	2010-10-06T00:00:00	2599-12-31T23:59:59
LD	UNH	HHZ	43.092651	-70.865028	5	100	2013-11-26T00:00:00	2599-12-31T23:59:59
LD	WCNY	HHZ	43.980999	-75.6549	245	100	2011-03-31T17:00:00	2599-12-31T23:59:59
LD	WVNY	HHZ	42.4062	-78.604202	490	100	2010-12-28T18:55:00	2599-12-31T23:59:59
N4	D62A	HHZ	47.081902	-69.050102	189	100	2015-09-10T16:39:48	2018-11-29T17:59:59
N4	E62A	HHZ	46.620098	-69.522697	356	100	2015-09-11T21:35:44	2018-11-02T20:59:59
N4	E63A	HHZ	46.422001	-68.462303	238	100	2015-09-08T15:33:28	2018-09-10T17:05:00
N4	F62A	HHZ	45.896801	-69.9664	331	100	2015-09-14T17:26:22	2018-09-12T19:05:00
N4	F63A	HHZ	45.702999	-69.102898	386	100	2015-09-08T15:33:26	2018-09-08T13:25:00
N4	F64A	HHZ	45.8633	-68.349602	179	100	2015-09-08T15:33:28	2019-03-12T15:27:00
N4	G62A	HHZ	45.218601	-70.531898	426	100	2015-09-15T15:51:50	2019-03-13T16:47:00
N4	G65A	HHZ	45.200199	-67.563202	78	100	2015-09-08T15:33:27	2016-06-14T15:42:59
N4	H62A	HHZ	44.574299	-71.155899	381	100	2015-08-31T16:14:48	2019-03-13T16:47:00
N4	I62A	HHZ	43.874298	-71.335899	264	100	2015-09-22T14:57:24	2019-03-13T16:47:00
N4	I63A	HHZ	44.050499	-70.580902	177	100	2015-09-17T16:32:14	2019-03-13T16:47:00
N4	J54A	HHZ	43.2728	-78.639198	112	100	2014-10-17T19:27:46	2018-08-28T15:15:00
N4	J55A	HHZ	43.265701	-77.816704	97	100	2014-10-10T19:26:06	2019-03-13T16:47:00
N4	J56A	HHZ	43.276001	-76.857903	93	100	2015-06-18T14:14:45	2018-09-01T18:40:00
N4	J57A	HHZ	43.409901	-75.996803	191	100	2015-06-22T14:39:27	2018-08-08T18:00:00
N4	J58A	HHZ	43.360298	-75.285202	436	100	2015-08-10T15:11:16	2018-08-30T16:45:00
N4	J59A	HHZ	43.464699	-74.504097	541	100	2015-06-15T16:16:00	2019-03-13T16:47:00
N4	J61A	HHZ	43.346199	-72.553497	253	100	2015-09-21T15:27:35	2019-03-14T05:26:00
N4	K57A	HHZ	42.7313	-76.516296	408	100	2015-05-23T15:01:04	2019-03-13T16:47:00
N4	K62A	HHZ	42.6651	-72.234497	289	100	2015-09-23T22:36:34	2019-03-13T16:47:00
N4	L56A	HHZ	42.136501	-77.559097	688	100	2015-06-15T14:38:46	2019-03-13T16:47:00
N4	L59A	HHZ	42.190201	-75.042603	677	100	2015-06-11T01:04:00	2019-03-13T16:47:00
N4	L64A	HHZ	41.935902	-70.839104	17	100	2015-09-26T16:54:42	2019-03-12T15:27:00
N4	M55A	HHZ	41.468601	-78.7649	531	100	2014-10-14T17:51:43	2018-08-03T16:05:00
N4	M57A	HHZ	41.3372	-77.127998	319	100	2015-05-18T15:02:39	2019-03-12T15:27:00
N4	M63A	HHZ	41.403801	-72.046402	44	100	2015-06-05T15:23:56	2019-03-12T15:27:00
N4	N58A	HHZ	40.8396	-76.715797	200	100	2015-05-14T15:29:18	2019-03-12T15:27:00
N4	N62A	HHZ	40.931301	-73.467697	34	100	2015-06-05T16:12:59	2017-12-04T17:59:59
NE	BCX	BHZ	42.334999	-71.170502	60	40	2013-01-01T00:00:00	2013-03-07T16:30:00
NE	BCX	HHZ	42.334999	-71.170502	60	100	2013-03-07T16:30:00	2599-12-31T23:59:59
NE	BRYW	BHZ	41.917	-71.537804	116	40	2013-01-01T00:00:00	2013-03-05T18:05:00
NE	BRYW	HHZ	41.917	-71.537804	116	100	2013-03-05T18:05:00	2018-01-14T00:00:00
NE	DUNH	BHZ	43.137001	-70.934799	53	40	2013-01-01T00:00:00	2016-01-01T00:00:00
NE	EMMW	BHZ	44.7075	-67.457298	35	40	2013-01-01T00:00:00	2013-03-04T18:49:00
NE	EMMW	HHZ	44.7075	-67.457298	35	100	2013-03-04T18:49:00	2599-12-31T23:59:59
NE	FFD	BHZ	43.4701	-71.653702	131	40	2013-01-01T00:00:00	2013-03-07T16:44:00

NE	FFD	HHZ	43.4701	-71.653702	131	100	2013-03-07T16:44:00	2017-12-01T18:09:00
NE	HNH	BHZ	43.705101	-72.286499	180	40	2013-01-01T00:00:00	2013-02-28T19:01:00
NE	HNH	HHZ	43.705101	-72.286499	180	100	2013-02-28T19:01:00	2599-12-31T23:59:59
NE	ORNO	BHZ	44.904499	-68.662201	40	40	2013-01-01T00:00:00	2016-01-01T00:00:00
NE	PQI	BHZ	46.671299	-68.018997	162	40	2013-01-01T00:00:00	2013-03-04T18:34:00
NE	PQI	HHZ	46.671299	-68.018997	162	100	2013-03-04T18:34:00	2599-12-31T23:59:59
NE	QUA2	BHZ	42.278999	-72.351997	168	40	2013-01-01T00:00:00	2013-03-04T19:30:00
NE	QUA2	HHZ	42.278999	-72.351997	168	100	2013-03-04T19:30:00	2599-12-31T23:59:59
NE	TRY	BHZ	42.7313	-73.666397	89	40	2013-01-01T00:00:00	2013-03-05T18:20:00
NE	TRY	HHZ	42.7313	-73.666397	89	100	2013-03-05T18:20:00	2599-12-31T23:59:59
NE	VT1	BHZ	44.320599	-72.751297	149	40	2013-01-01T00:00:00	2013-02-28T19:31:00
NE	VT1	HHZ	44.320599	-72.751297	149	100	2013-02-28T19:31:00	2599-12-31T23:59:59
NE	WES	BHZ	42.3848	-71.3218	60	40	2013-01-01T00:00:00	2013-01-23T19:00:00
NE	WES	HHZ	42.3848	-71.3218	60	100	2013-01-23T19:00:00	2599-12-31T23:59:59
NE	WSPT	BHZ	41.1712	-73.327797	91	40	2013-01-01T00:00:00	2013-03-07T16:14:00
NE	WSPT	HHZ	41.1712	-73.327797	91	100	2013-03-07T16:14:00	2016-11-02T15:04:00
NE	WVL	BHZ	44.564602	-69.661697	50	40	2013-01-01T00:00:00	2013-03-05T18:35:00
NE	WVL	HHZ	44.564602	-69.661697	50	100	2013-03-05T18:35:00	2599-12-31T23:59:59
NE	YLE	BHZ	41.314999	-72.936501	5	40	2013-01-01T00:00:00	2013-01-24T18:30:00
NE	YLE	HHZ	41.321098	-72.921997	41	100	2013-01-24T00:00:00	2018-07-11T00:00:00
TA	D50A	BHZ	47.166801	-79.841202	331	40	2013-01-01T00:00:00	2014-08-24T17:15:00
TA	D51A	BHZ	47.090401	-79.373299	282	40	2013-01-01T00:00:00	2014-08-25T15:35:00
TA	D52A	BHZ	46.976398	-78.411697	359	40	2013-01-01T00:00:00	2014-08-26T16:05:00
TA	D53A	BHZ	47.079498	-77.700104	347	40	2013-01-01T00:00:00	2014-09-16T15:45:00
TA	D54A	BHZ	47.152	-76.656998	415	40	2013-01-01T00:00:00	2014-09-17T15:30:00
TA	D55A	BHZ	47.019001	-75.473198	331	40	2013-08-09T00:00:00	2015-06-30T15:05:00
TA	D56A	BHZ	47.0485	-74.756798	421	40	2013-07-29T00:00:00	2015-07-02T15:55:00
TA	D57A	BHZ	47.0172	-73.887802	422	40	2013-08-18T00:00:00	2015-07-16T15:33:10
TA	D58A	BHZ	47.095402	-72.882599	398	40	2013-08-16T00:00:00	2015-07-22T16:00:00
TA	D59A	BHZ	47.007301	-71.8358	204	40	2013-07-31T00:00:00	2015-07-24T13:55:00
TA	D60A	BHZ	46.913898	-70.923698	40	40	2013-08-01T00:00:00	2015-07-23T18:25:00
TA	D61A	BHZ	47.202202	-70.186798	146	40	2013-08-02T00:00:00	2015-07-27T15:20:00
TA	D62A	BHZ	47.081902	-69.050102	189	40	2013-10-08T00:00:00	2015-09-10T16:39:48
TA	D63A	BHZ	47.036999	-68.106598	256	40	2013-09-19T00:00:00	2015-09-01T15:25:00
TA	E51A	BHZ	46.533298	-79.492401	369	40	2013-01-01T00:00:00	2014-08-24T13:30:00
TA	E52A	BHZ	46.285099	-78.656898	252	40	2013-01-01T00:00:00	2014-08-23T14:10:00
TA	E53A	BHZ	46.378399	-77.663803	355	40	2013-01-01T00:00:00	2014-09-11T16:25:00
TA	E54A	BHZ	46.433899	-77.186897	277	40	2013-01-01T00:00:00	2014-09-14T16:15:00
TA	E55A	BHZ	46.4538	-76.057198	180	40	2013-07-28T00:00:00	2015-07-06T13:15:00
TA	E56A	BHZ	46.543598	-75.034103	320	40	2013-07-30T00:00:00	2015-07-03T15:55:00
TA	E57A	BHZ	46.411701	-74.147102	572	40	2013-08-06T00:00:00	2015-07-02T16:25:00
TA	E58A	BHZ	46.372101	-73.2771	233	40	2013-07-30T00:00:00	2015-07-11T20:00:00
TA	E59A	BHZ	46.480301	-72.510803	62	40	2013-07-30T00:00:00	2015-07-23T13:45:00
TA	E60A	BHZ	46.3689	-71.446899	181	40	2013-08-07T00:00:00	2015-07-25T13:25:00
TA	E61A	BHZ	46.431198	-70.488998	527	40	2013-08-06T00:00:00	2015-07-25T13:55:00
TA	E62A	BHZ	46.620098	-69.522697	356	40	2013-10-09T00:00:00	2015-09-11T21:35:44
TA	E63A	BHZ	46.422001	-68.462303	238	40	2013-09-23T00:00:00	2015-09-08T15:33:28
TA	E64A	BHZ	46.4184	-67.828499	190	40	2013-09-18T00:00:00	2015-09-01T19:40:00
TA	F51A	BHZ	45.928398	-79.915001	239	40	2013-01-01T00:00:00	2014-08-19T14:00:00
TA	F52A	BHZ	45.795101	-79.322701	351	40	2013-01-01T00:00:00	2014-08-08T19:05:00
TA	F55A	BHZ	45.833801	-76.350998	218	40	2013-01-01T00:00:00	2014-09-29T16:10:00
TA	F57A	BHZ	45.812199	-74.692802	178	40	2013-07-27T00:00:00	2015-06-27T15:15:00
TA	F58A	BHZ	45.866299	-73.814499	73	40	2013-07-27T00:00:00	2015-07-11T13:35:00
TA	F59A	BHZ	45.851299	-72.783302	43	40	2013-08-08T00:00:00	2015-07-10T13:15:00
TA	F60A	BHZ	45.9688	-71.951401	229	40	2013-08-07T00:00:00	2015-07-12T18:30:00
TA	F61A	BHZ	45.9743	-70.992104	350	40	2013-08-05T00:00:00	2015-07-25T17:05:00
TA	F62A	BHZ	45.896801	-69.9664	331	40	2013-09-27T00:00:00	2015-09-14T17:26:22
TA	F63A	BHZ	45.702999	-69.102898	386	40	2013-09-24T00:00:00	2015-09-08T15:33:26
TA	F64A	BHZ	45.8633	-68.349602	179	40	2013-09-23T00:00:00	2015-09-08T15:33:28
TA	G53A	BHZ	45.1222	-78.623703	333	40	2013-01-01T00:00:00	2014-08-09T15:50:00
TA	G54A	BHZ	45.3979	-78.089798	465	40	2013-07-22T00:00:00	2015-06-24T14:55:00
TA	G55A	BHZ	45.253201	-76.718697	228	40	2013-01-01T00:00:00	2014-09-30T15:00:00
TA	G57A	BHZ	45.1036	-74.985497	96	40	2013-07-24T00:00:00	2015-07-08T14:35:00
TA	G58A	BHZ	45.1492	-74.054001	53	40	2013-07-25T00:00:00	2015-07-09T15:15:00
TA	G59A	BHZ	45.0807	-73.180901	36	40	2013-09-17T00:00:00	2015-07-14T14:00:00
TA	G60A	BHZ	45.097698	-72.333702	391	40	2013-08-10T00:00:00	2015-07-13T15:35:00
TA	G61A	BHZ	45.2827	-71.527298	378	40	2013-09-25T00:00:00	2015-07-28T15:15:00
TA	G62A	BHZ	45.218601	-70.531898	426	40	2013-09-20T00:00:00	2015-09-15T15:51:50
TA	G63A	BHZ	45.1147	-69.618599	363	40	2013-09-22T00:00:00	2015-08-31T13:50:00
TA	G64A	BHZ	45.252701	-68.755798	165	40	2013-09-22T00:00:00	2015-09-04T13:15:00
TA	G65A	BHZ	45.200199	-67.563202	78	40	2013-09-24T00:00:00	2015-09-08T15:33:27

TA	H52A	BHZ	44.6422	-79.888802	209	40	2013-01-01T00:00:00	2014-08-03T15:15:00
TA	H53A	BHZ	44.573601	-78.583199	292	40	2013-07-21T00:00:00	2015-06-24T20:20:00
TA	H55A	BHZ	44.550499	-77.182999	182	40	2013-01-01T00:00:00	2014-09-25T17:05:00
TA	H56A	BHZ	44.592999	-76.259399	137	40	2013-01-01T00:00:00	2014-09-27T14:20:00
TA	H57A	BHZ	44.462399	-75.390503	132	40	2013-08-25T00:00:00	2015-08-10T16:55:00
TA	H58A	BHZ	44.417599	-74.179802	537	40	2013-08-25T00:00:00	2015-08-17T15:10:00
TA	H59A	BHZ	44.6455	-73.690498	355	40	2013-08-24T00:00:00	2015-08-16T14:55:00
TA	H60A	BHZ	44.5606	-72.698601	459	40	2013-09-21T00:00:00	2015-08-24T17:20:00
TA	H61A	BHZ	44.523899	-71.927101	462	40	2013-09-21T00:00:00	2015-08-27T14:50:00
TA	H62A	BHZ	44.574299	-71.155899	381	40	2013-09-19T00:00:00	2015-08-31T16:14:48
TA	H63A	BHZ	44.661598	-70.035301	109	40	2013-09-20T00:00:00	2015-08-31T17:40:00
TA	H64A	BHZ	44.641201	-69.220299	158	40	2013-09-18T00:00:00	2015-09-05T13:45:00
TA	H65A	BHZ	44.696098	-68.246902	98	40	2013-09-16T00:00:00	2015-09-03T13:50:00
TA	H66A	BHZ	44.7859	-67.311501	55	40	2013-09-25T00:00:00	2015-09-03T17:10:00
TA	I53A	BHZ	43.823799	-79.591202	195	40	2013-01-01T00:00:00	2014-08-06T15:50:00
TA	I55A	BHZ	44.216099	-77.681702	132	40	2013-01-01T00:00:00	2014-09-26T15:45:00
TA	I57A	BHZ	43.937698	-75.659897	321	40	2013-08-26T00:00:00	2015-08-24T14:45:00
TA	I58A	BHZ	43.690102	-74.973297	599	40	2013-08-26T00:00:00	2015-08-12T15:30:00
TA	I59A	BHZ	43.7957	-73.874397	390	40	2013-09-18T00:00:00	2015-08-25T16:30:00
TA	I60A	BHZ	43.844002	-73.291603	101	40	2013-09-20T00:00:00	2015-09-20T17:50:00
TA	I61A	BHZ	43.932301	-72.208298	287	40	2013-09-20T00:00:00	2015-08-28T14:45:00
TA	I62A	BHZ	43.874298	-71.335899	264	40	2013-09-07T00:00:00	2015-09-22T14:57:24
TA	I63A	BHZ	44.050499	-70.580902	177	40	2013-09-27T00:00:00	2015-09-17T16:32:14
TA	I64A	BHZ	43.919701	-69.634697	17	40	2013-09-26T00:00:00	2015-09-07T15:15:00
TA	J54A	BHZ	43.2728	-78.639198	112	40	2013-01-01T00:00:00	2014-10-17T19:27:46
TA	J55A	BHZ	43.265701	-77.816704	97	40	2013-01-01T00:00:00	2014-10-10T19:26:06
TA	J56A	BHZ	43.276001	-76.857903	93	40	2013-08-18T00:00:00	2015-06-18T14:14:45
TA	J57A	BHZ	43.409901	-75.996803	191	40	2013-08-22T00:00:00	2015-06-22T14:39:27
TA	J58A	BHZ	43.360298	-75.285202	436	40	2013-08-27T00:00:00	2015-08-10T15:11:16
TA	J59A	BHZ	43.464699	-74.504097	541	40	2013-08-27T00:00:00	2015-06-15T16:16:00
TA	J60A	BHZ	43.243801	-73.421204	265	40	2013-09-17T00:00:00	2015-08-15T17:10:00
TA	J61A	BHZ	43.346199	-72.553497	253	40	2013-09-06T00:00:00	2015-09-21T15:27:35
TA	J62A	BHZ	43.2262	-71.812698	266	40	2013-09-07T00:00:00	2015-09-16T13:35:00
TA	J63A	BHZ	43.279202	-71.078102	142	40	2013-09-08T00:00:00	2015-09-16T18:00:00
TA	K54A	BHZ	42.609699	-78.690804	465	40	2013-05-15T00:00:00	2014-10-28T14:55:00
TA	K55A	BHZ	42.727798	-78.069603	482	40	2013-01-01T00:00:00	2014-10-10T16:05:00
TA	K56A	BHZ	42.698101	-77.324402	575	40	2013-08-18T00:00:00	2015-08-16T13:50:00
TA	K57A	BHZ	42.7313	-76.516296	408	40	2013-08-21T00:00:00	2015-05-23T15:01:04
TA	K58A	BHZ	42.763302	-75.647301	509	40	2013-08-29T00:00:00	2015-06-07T20:35:00
TA	K59A	BHZ	42.775002	-74.852501	570	40	2013-09-15T00:00:00	2015-06-07T15:40:00
TA	K60A	BHZ	42.616798	-73.888603	79	40	2013-09-13T00:00:00	2015-06-07T13:00:00
TA	K61A	BHZ	42.669498	-73.267601	391	40	2013-09-26T00:00:00	2015-09-25T16:20:00
TA	K62A	BHZ	42.6651	-72.234497	289	40	2013-09-09T00:00:00	2015-09-23T22:36:34
TA	K63A	BHZ	42.688801	-71.528297	68	40	2013-09-08T00:00:00	2015-09-08T13:35:00
TA	L54A	BHZ	42.234501	-79.3162	432	40	2013-03-26T00:00:00	2014-10-27T15:00:00
TA	L55A	BHZ	42.183102	-78.436798	633	40	2013-01-24T00:00:00	2014-10-14T15:10:00
TA	L56A	BHZ	42.136501	-77.559097	688	40	2013-08-17T00:00:00	2015-06-15T14:38:46
TA	L57A	BHZ	42.0005	-76.849197	546	40	2013-08-29T00:00:00	2015-05-19T18:50:00
TA	L58A	BHZ	42.044701	-75.850197	447	40	2013-07-03T00:00:00	2015-08-08T16:50:00
TA	L59A	BHZ	42.190201	-75.042603	677	40	2013-09-03T00:00:00	2015-06-11T01:04:00
TA	L60A	BHZ	41.988998	-74.222603	388	40	2013-09-04T00:00:00	2015-05-28T14:10:00
TA	L61A	BHZ	42.193401	-73.554298	275	40	2013-09-14T00:00:00	2015-06-06T16:35:00
TA	L61B	BHZ	42.449799	-72.680199	261	40	2013-09-10T00:00:00	2016-01-01T00:00:00
TA	L62A	BHZ	42.032799	-72.661697	49	40	2013-09-06T00:00:00	2015-06-06T14:10:00
TA	L63A	BHZ	41.863098	-71.609497	109	40	2013-09-11T00:00:00	2015-09-17T16:55:00
TA	L64A	BHZ	41.935902	-70.839104	17	40	2013-09-12T00:00:00	2015-09-26T16:54:42
TA	L65A	BHZ	42.029499	-70.052803	50	40	2013-09-27T00:00:00	2015-09-24T15:15:00
TA	M54A	BHZ	41.5079	-79.664703	488	40	2013-01-01T00:00:00	2016-01-01T00:00:00
TA	M55A	BHZ	41.468601	-78.7649	531	40	2013-01-26T00:00:00	2014-10-14T17:51:43
TA	M56A	BHZ	41.4837	-78.182602	493	40	2013-05-20T00:00:00	2015-05-14T16:00:00
TA	M57A	BHZ	41.3372	-77.127998	319	40	2013-08-30T00:00:00	2015-05-18T15:02:39
TA	M58A	BHZ	41.372101	-76.460297	529	40	2013-07-02T00:00:00	2015-05-20T13:10:00
TA	M59A	BHZ	41.541302	-75.432098	471	40	2013-06-12T00:00:00	2015-05-20T20:15:00
TA	M60A	BHZ	41.3265	-74.625	292	40	2013-08-31T00:00:00	2015-05-23T16:00:00
TA	M61A	BHZ	41.310398	-73.767303	190	40	2013-05-30T00:00:00	2015-05-25T14:20:00
TA	M62A	BHZ	41.442299	-72.893898	24	40	2013-09-12T00:00:00	2015-06-04T14:05:00
TA	M63A	BHZ	41.403801	-72.046402	44	40	2013-09-07T00:00:00	2015-06-05T15:23:56
TA	M64A	BHZ	41.5509	-71.210197	17	40	2013-09-12T00:00:00	2015-09-17T13:20:00
TA	M65A	BHZ	41.562	-70.646599	22	40	2013-01-01T00:00:00	2016-01-01T00:00:00
TA	M66A	BHZ	41.258999	-70.1353	9	40	2013-09-28T00:00:00	2015-09-26T13:35:00
TA	N54A	BHZ	40.9617	-79.989197	408	40	2013-01-01T00:00:00	2016-01-01T00:00:00

TA	N55A	BHZ	40.7808	-78.986198	559	40	2013-01-01T00:00:00	2014-11-05T15:50:00
TA	N56A	BHZ	40.917099	-78.295303	561	40	2013-05-21T00:00:00	2015-05-10T14:20:00
TA	N57A	BHZ	40.7556	-77.550903	306	40	2013-05-13T00:00:00	2015-05-10T15:45:30
TA	N58A	BHZ	40.8396	-76.715797	200	40	2013-07-04T00:00:00	2015-05-14T15:29:18
TA	N59A	BHZ	40.916801	-75.770302	508	40	2013-01-01T00:00:00	2016-01-01T00:00:00
TA	N60A	BHZ	40.870399	-75.099998	189	40	2013-06-12T00:00:00	2015-05-28T15:35:00
TA	N61A	BHZ	40.7519	-74.296898	108	40	2013-09-05T00:00:00	2015-05-27T15:00:00
TA	N62A	BHZ	40.931301	-73.467697	34	40	2013-09-09T00:00:00	2015-06-05T16:12:59
TA	N63A	BHZ	40.987801	-72.520599	8	40	2013-09-10T00:00:00	2015-06-05T15:35:00
TA	O55A	BHZ	40.2076	-79.3041	469	40	2013-01-01T00:00:00	2014-11-15T16:00:00
TA	O56A	BHZ	40.268299	-78.566299	684	40	2013-01-01T00:00:00	2016-01-01T00:00:00
TA	O57A	BHZ	40.2104	-77.635399	377	40	2013-05-22T00:00:00	2015-05-07T15:20:00
TA	O58A	BHZ	40.1231	-76.922798	321	40	2013-06-15T00:00:00	2015-05-07T18:10:00
TA	O59A	BHZ	40.311401	-76.185898	334	40	2013-04-28T00:00:00	2015-05-21T15:50:00
TA	O60A	BHZ	40.317699	-75.404999	70	40	2013-04-28T00:00:00	2015-05-22T14:30:00
TA	O61A	BHZ	40.093399	-74.553001	38	40	2013-05-29T00:00:00	2015-05-27T14:35:00
US	BINY	BHZ	42.199299	-75.986099	498	40	2013-01-01T00:00:00	2016-01-01T00:00:00
US	ERPA	BHZ	42.1175	-79.989098	306.3	40	2013-01-01T00:00:00	2016-01-01T00:00:00
US	LBNH	BHZ	44.240101	-71.925903	367	40	2013-01-01T00:00:00	2016-01-01T00:00:00
US	LONY	BHZ	44.619701	-74.582901	440	40	2013-01-01T00:00:00	2016-01-01T00:00:00
US	PKME	BHZ	45.2644	-69.291702	108.5	40	2013-01-01T00:00:00	2016-01-01T00:00:00

Table 2. All of the stations within the NEUSSEC that were recording between 1 January 2013 and 1 January 2016. StartTime and EndTime designate when the station started and ended recording data on that channel, respectively. Data from The International Federation of Digital Seismograph Networks.

Station ID	Latitude	Longitude	Elevation (M)	Sensor Type	Digitization Rate (Hz)	Start Date	Latest Date	Status
ACTN	42.49402N	71.46930W	163.1	CMG-40T	100	01-Sep-2017 (244d)	04-Jul-2018 (185d)	on
AWD	42.47723N	71.48711W	129.6	Trillium	100	31-Jan-2018 (031d)	03-Jul-2018 (184d)	on; gap March 7-27
HRVD	42.47983N	71.58527W	171.3	CMG-40T	100	19-Dec-2017 (353d)	04-Jul-2018 (185d)	on
STOW	42.46318N	71.51688W	164.9	Trillium	100	29-Dec-2017 (363d)	03-Jul-2018 (184d)	on
HRV	42.506401	-71.558296	200	Streckeisen STS-2 High-gain	100	2016-05-11T16:00:00	2018-08-24T00:00:00	on
HRV	42.506401	-71.558296	200	Streckeisen STS-2.5	100	2018-08-24T00:00:00	2599-12-31T23:59:59	on

Table 3. All of the stations that make up ALSA, including the IU HRV station. Data from Boston College's Weston Observatory and The International Federation of Digital Seismograph Networks.

YYYY-MM-DD	HH:MM:SS	Latitude (Degrees North)	Longitude (Degrees West)	Depth (km)	Magnitude (M)
2013-01-14	18:19:25	43.91	69.64	3.74	2.5
2013-01-16	13:46:38	44.49	74.07	5.16	2.2
2013-01-16	1:01:50	46.06	75.44	18.19	2.2
2013-01-16	0:53:06	46.05	75.44	19.06	2.7
2013-01-20	6:24:07	49.30	65.85	4.93	2.1
2013-02-07	5:30:20	45.41	71.47	6.41	2.7
2013-02-19	9:53:04	41.39	77.27	0.62	2.0
2013-02-19	4:59:45	48.45	83.32	12.00	3.4
2013-02-23	5:40:40	49.66	65.05	4.45	2.7
2013-03-04	6:42:18	47.24	77.30	20.69	2.0
2013-03-13	20:32:23	45.53	74.58	5.12	2.0
2013-03-14	0:01:53	43.85	74.22	0.03	2.1
2013-03-21	5:22:18	46.43	66.10	10.71	3.0
2013-04-03	8:13:42	48.87	67.71	20.04	2.3
2013-04-06	1:53:40	48.78	68.71	24.03	2.2
2013-04-15	13:32:27	45.79	74.46	4.34	2.5
2013-04-30	13:44:47	47.02	66.48	15.60	2.0
2013-05-06	7:29:50	49.42	66.84	19.11	3.0
2013-05-17	20:15:19	45.74	76.35	6.91	2.6
2013-05-17	13:43:24	45.75	76.34	13.00	4.7
2013-05-17	13:53:56	45.75	76.34	15.75	3.6
2013-05-21	20:43:02	45.43	74.22	0.03	3.0
2013-05-24	19:48:09	45.75	76.34	4.85	2.4
2013-05-24	7:08:34	47.04	76.74	23.46	2.9
2013-05-30	5:34:59	45.75	76.35	10.42	3.0
2013-06-05	13:16:17	42.35	65.10	5.30	2.1
2013-06-16	5:47:24	45.12	75.44	0.03	2.0
2013-06-20	1:37:21	46.51	66.21	5.93	2.6
2013-06-21	10:14:28	44.52	69.75	10.37	3.0
2013-06-29	6:29:30	49.00	66.65	16.84	2.3
2013-06-30	8:40:47	45.73	76.31	5.93	2.2
2013-07-01	7:48:48	41.68	81.31	5.00	2.6
2013-07-11	20:16:07	47.84	70.09	10.07	3.5
2013-07-11	20:58:12	47.74	70.09	17.69	2.2
2013-07-25	12:31:25	46.28	66.92	18.26	2.5
2013-07-27	4:50:44	43.27	75.13	0.02	2.6
2013-08-22	18:56:53	46.51	66.21	6.84	2.3
2013-08-24	7:51:25	47.05	65.29	1.42	2.6
2013-08-25	13:33:14	43.35	73.78	9.44	2.6
2013-08-28	10:02:15	47.00	66.60	5.28	2.1
2013-08-28	9:44:34	46.98	66.61	7.20	3.0
2013-08-29	10:24:13	48.57	68.21	21.53	2.2
2013-09-04	21:46:49	47.93	77.93	5.00	2.9
2013-09-04	1:52:13	46.68	75.60	17.67	2.5
2013-09-21	14:48:38	49.16	67.69	0.02	4.0
2013-09-25	16:17:30	48.96	66.62	13.65	2.7
2013-09-28	0:34:39	44.98	57.50	5.00	3.9
2013-09-29	11:32:18	49.26	67.15	36.78	2.4
2013-10-04	13:13:02	47.65	69.90	10.75	2.1
2013-10-04	22:04:43	46.93	71.10	17.89	2.0
2013-10-11	1:07:41	43.26	71.75	12.85	2.5
2013-10-15	3:44:21	48.61	67.39	12.33	2.0
2013-10-20	10:40:34	45.63	77.44	17.16	3.0
2013-10-24	8:45:33	45.14	59.80	5.00	3.4
2013-10-24	8:45:01	44.84	57.41	5.00	3.9
2013-11-30	4:07:12	47.51	66.42	0.02	2.3
2013-12-11	7:47:21	47.23	70.40	5.35	3.1
2013-12-21	15:21:15	45.11	74.00	10.94	2.2
2013-12-26	4:37:52	47.98	71.11	13.60	2.6
2014-01-28	11:32:03	44.11	72.04	7.57	2.2
2014-02-05	21:53:10	45.47	61.22	5.00	2.9
2014-02-05	21:52:25	44.61	58.06	5.00	3.6
2014-02-07	15:45:07	45.05	73.67	1.71	2.5
2014-02-11	22:46:34	41.69	70.93	3.05	2.3
2014-02-13	4:57:38	43.62	78.37	3.68	2.8
2014-03-25	19:51:10	45.44	74.19	3.26	2.3
2014-04-24	8:37:04	46.37	74.10	10.57	2.0
2014-04-28	14:52:55	46.97	66.61	8.35	3.0
2014-05-26	21:33:49	48.95	68.02	17.98	3.1

2014-05-31	21:45:27	47.09	66.68	6.13	2.0
2014-07-04	22:55:58	45.92	74.85	14.63	2.6
2014-07-05	14:46:40	41.35	73.94	5.74	2.3
2014-07-10	18:22:40	47.27	66.95	0.02	3.0
2014-07-10	19:19:18	47.26	66.96	0.08	2.1
2014-07-10	18:24:27	47.29	66.96	0.08	2.5
2014-07-11	4:34:54	47.24	66.97	0.02	2.2
2014-07-17	4:54:28	45.42	66.92	13.84	2.4
2014-07-26	19:50:52	46.88	72.01	5.24	2.3
2014-07-27	15:13:31	45.65	77.21	0.04	2.3
2014-08-01	17:50:44	45.03	75.70	0.04	2.1
2014-08-02	18:38:40	47.60	70.19	13.85	2.2
2014-08-14	7:09:15	41.38	72.52	8.90	2.6
2014-08-18	11:07:48	42.43	70.53	0.03	2.0
2014-09-17	13:21:55	45.07	66.86	0.03	2.0
2014-09-23	2:58:03	48.51	69.34	18.93	2.9
2014-11-02	1:58:09	46.94	67.02	0.02	2.6
2014-11-02	7:04:40	48.87	66.16	4.36	2.1
2014-11-17	0:24:59	45.86	75.01	4.35	2.7
2014-11-28	4:58:57	49.23	67.32	32.64	2.0
2014-12-30	2:44:51	45.13	74.24	0.38	2.4
2015-01-07	13:03:25	46.99	66.63	5.66	2.0
2015-01-08	14:28:01	41.77	71.90	5.89	2.0
2015-01-12	11:36:39	41.76	71.90	0.68	3.1
2015-01-12	11:50:06	41.76	71.89	3.59	2.0
2015-01-13	12:27:07	41.75	71.91	2.71	2.1
2015-01-16	13:05:29	49.36	66.80	13.08	3.7
2015-01-19	6:09:48	47.37	66.33	0.02	2.4
2015-01-19	16:35:15	45.17	74.19	0.03	2.0
2015-01-21	5:32:00	47.31	70.24	12.70	3.1
2015-01-25	23:25:11	39.97	75.66	0.03	2.7
2015-01-25	16:38:38	47.08	66.61	6.68	2.3
2015-02-08	9:34:30	44.76	74.60	2.34	2.5
2015-02-17	10:49:15	45.13	67.06	0.80	2.1
2015-03-11	23:45:54	44.61	70.90	5.80	2.2
2015-03-14	10:24:47	43.70	71.48	4.15	2.2
2015-04-10	23:28:27	47.71	70.20	10.79	2.4
2015-04-20	10:13:45	46.68	73.18	2.74	3.1
2015-04-21	11:16:47	47.44	70.19	6.46	2.4
2015-04-24	9:44:52	46.38	65.75	7.98	2.0
2015-04-29	8:11:23	43.49	71.58	8.83	2.0
2015-05-02	8:34:25	46.90	78.88	4.93	3.6
2015-05-22	4:45:01	44.50	70.29	10.58	2.4
2015-05-23	20:21:59	45.04	74.22	0.02	2.2
2015-05-24	18:12:28	43.29	71.69	8.61	2.3
2015-05-27	3:56:14	43.43	79.13	2.95	2.0
2015-06-20	14:40:30	44.44	65.43	10.97	2.2
2015-06-28	9:15:05	47.25	70.11	16.14	3.3
2015-07-01	18:32:57	44.18	66.35	25.67	3.4
2015-07-06	6:15:24	48.42	65.79	5.15	2.3
2015-07-06	2:14:51	46.58	72.54	18.84	2.9
2015-07-07	9:46:31	46.38	75.25	26.31	3.3
2015-07-12	4:17:41	47.38	69.92	8.25	2.2
2015-07-13	19:27:29	45.15	73.97	5.64	2.7
2015-07-15	22:00:20	45.44	74.52	6.33	3.7
2015-07-22	7:43:02	41.78	71.42	13.12	2.4
2015-07-26	22:36:14	46.93	75.80	34.71	3.3
2015-08-02	2:34:28	43.18	71.29	4.95	2.6
2015-08-14	7:41:25	40.75	74.58	5.36	2.7
2015-08-17	23:11:16	45.95	74.83	0.04	3.1
2015-08-21	23:49:15	47.15	66.38	4.83	2.6
2015-08-27	22:47:52	46.29	66.43	23.69	3.6
2015-08-30	20:27:45	46.10	75.14	0.02	2.3
2015-09-09	19:17:51	45.75	76.33	11.21	3.1
2015-09-13	0:45:19	47.33	70.29	0.43	2.4
2015-09-23	1:35:00	45.36	73.35	1.79	2.3
2015-09-27	3:16:23	42.45	74.42	6.63	3.0
2015-10-28	20:42:15	43.06	74.39	0.08	2.6
2015-11-01	22:20:33	44.32	67.98	6.96	2.3
2015-11-04	15:04:25	47.40	66.83	26.36	3.6

2015-11-16	8:23:36	49.10	66.47	5.24	2.4
2015-11-28	5:16:53	45.01	74.87	0.02	3.5
2015-12-07	16:15:02	45.54	67.39	1.29	2.2
2015-12-11	3:45:10	46.77	71.19	3.50	2.0
2015-12-14	4:30:30	47.35	74.48	34.01	2.0

Table 4: The 144 earthquakes of magnitude greater or equal to M2 that occurred within the NEUSSEC between 2013-2016, when the Earthscope Transportable Array was active in the region. Data from Boston College's Weston Observatory.

YYYY-MM-DD	HH:MM:SS	Latitude (Degrees North)	Longitude (Degrees East)	Depth (km)	Magnitude (M)
2015-12-17	19:49:53	15.80	-93.63	85	6.6
2015-12-09	10:21:49	-4.11	129.51	21	6.9
2015-12-07	7:50:06	38.21	72.78	22	7.2
2015-12-04	22:25:00	-47.62	85.09	35	7.1
2015-11-26	5:45:18	-9.18	-71.26	603	6.7
2015-11-24	22:50:54	-10.06	-71.02	621	7.6
2015-11-24	22:45:39	-10.54	-70.94	606	7.6
2015-11-18	18:31:05	-8.90	158.42	13	6.8
2015-11-17	7:10:07	38.67	20.60	11	6.5
2015-11-13	20:51:31	31.00	128.87	12	6.7
2015-11-11	2:46:20	-29.51	-72.06	10	6.9
2015-11-11	1:54:39	-29.51	-72.01	12	6.9
2015-11-09	16:03:46	51.64	-173.07	15	6.5
2015-11-08	16:47:02	6.84	94.65	10	6.6
2015-11-07	7:31:44	-30.88	-71.45	46	6.8
2015-11-04	3:44:15	-8.34	124.88	20	6.5
2015-10-26	9:09:43	36.52	70.37	231	7.5
2015-10-20	21:52:03	-14.86	167.30	135	7.1
2015-09-24	15:53:28	-0.62	131.26	18	6.6
2015-09-21	17:40:00	-31.73	-71.38	35	6.6
2015-09-17	4:10:28	-31.52	-71.80	23	6.7
2015-09-17	3:55:15	-31.42	-71.69	27	6.5
2015-09-16	23:18:42	-31.56	-71.43	28	7.0
2015-09-16	22:54:33	-31.57	-71.67	22	8.3
2015-09-13	8:14:09	24.91	-109.62	10	6.7
2015-08-12	18:49:24	-9.33	157.88	6	6.5
2015-08-10	4:12:16	-9.34	158.05	22	6.6
2015-07-27	21:41:22	-2.63	138.53	48	7.0
2015-07-27	4:49:46	52.38	-169.45	29	6.9
2015-07-18	2:27:34	-10.40	165.14	11	7.0
2015-07-16	15:16:34	13.87	-58.55	20	6.5
2015-07-10	4:12:43	-9.31	158.40	12	6.7
2015-06-23	12:18:30	27.74	139.73	460	6.5
2015-06-17	12:51:33	-35.36	-17.16	10	7.0
2015-05-30	11:23:02	27.84	140.49	664	7.8
2015-05-29	7:00:10	56.59	-156.43	73	6.8
2015-05-22	23:59:34	-11.11	163.22	10	6.8
2015-05-22	21:45:19	-11.06	163.70	11	6.9
2015-05-20	22:48:53	-10.88	164.17	11	6.8
2015-05-19	15:25:21	-54.33	-132.16	7	6.7
2015-05-12	21:12:59	38.91	142.03	35	6.8
2015-05-12	7:05:20	27.81	86.07	15	7.3
2015-05-07	7:10:20	-7.22	154.56	10	7.1
2015-05-05	1:44:06	-5.46	151.88	55	7.5
2015-05-01	8:06:03	-5.20	151.78	44	6.8
2015-04-30	10:45:03	-5.38	151.77	31	6.7
2015-04-26	7:09:11	27.77	86.02	23	6.7
2015-04-25	6:45:21	28.22	84.82	10	6.6
2015-04-25	6:11:26	28.23	84.73	8	7.8
2015-04-17	15:52:51	-15.88	-178.60	10	6.5
2015-03-30	8:48:25	-15.50	-173.03	11	6.5
2015-03-29	23:48:31	-4.73	152.56	41	7.5
2015-02-27	13:45:05	-7.30	122.53	552	7.0
2015-02-16	23:06:28	39.86	142.88	23	6.7

2015-02-13	18:59:12	52.65	-31.90	17	7.1
2015-02-11	18:57:22	-23.11	-66.69	223	6.7
2015-01-23	3:47:27	-17.03	168.52	220	6.8
2015-01-07	5:07:08	5.90	-82.66	8	6.5

Table 5: The 58 earthquakes of magnitude greater or equal to M6.5 that occurred throughout the world in 2015, when the Earthscope Transportable Array was active in the NEUSSEC. Data from Boston College's Weston Observatory.

YYYY-MM-DD	HH:MM:SS	Latitude (Degrees North)	Longitude (Degrees (West))	Depth (km)	Magnitude (M)
2019-06-28	1:16:34	47.67	70.00	18.84	2.2
2019-06-27	0:33:43	45.07	71.65	0.02	1.7
2019-06-15	4:15:15	47.51	69.96	9.55	2.5
2019-06-13	0:30:57	40.42	77.51	26.70	3.4
2019-06-02	20:19:22	45.41	73.31	16.45	1.6
2019-05-31	21:19:52	44.72	74.57	3.16	2.9
2019-04-27	2:17:43	42.83	70.45	13.20	1.8
2019-04-22	22:08:57	42.47	70.57	4.74	1.5
2019-04-15	7:26:50	45.05	70.68	7.36	0.9
2019-04-12	15:38:01	40.87	74.17	8.36	1.8
2019-04-09	11:22:45	40.53	72.05	26.02	2.9
2019-04-07	12:38:45	44.38	74.95	0.04	1.4
2019-03-16	1:23:21	43.34	71.61	5.66	2.1
2019-03-07	3:17:53	47.11	65.38	20.43	2.8
2019-03-01	9:17:58	41.22	71.69	10.97	2.2
2019-02-18	23:26:33	42.46	71.50	2.14	0.6
2019-02-08	18:30:49	42.43	70.83	5.00	1.4
2019-02-06	20:01:28	42.59	71.40	1.10	1.7
2019-02-04	2:01:38	47.57	70.36	18.34	2.1
2019-01-28	23:10:55	42.57	72.04	0.82	1.0
2019-01-16	16:17:14	45.05	70.77	0.43	2.4
2019-01-15	23:30:48	37.23	73.01	10.00	4.6
2019-01-10	13:49:00	45.29	66.18	4.89	3.7
2019-01-05	1:12:42	43.76	71.36	6.22	1.1
2019-01-03	11:07:13	50.56	65.24	15.00	2.9
2018-12-23	3:19:25	42.56	72.04	1.19	2.1
2018-12-21	23:08:38	42.57	72.05	1.21	1.0
2018-12-21	17:51:23	42.55	72.04	0.16	1.6
2018-12-06	14:30:50	43.66	72.38	13.46	1.6
2018-12-03	23:56:23	43.38	71.06	5.10	1.9
2018-11-25	13:34:09	45.21	73.89	10.50	2.2
2018-11-25	3:41:16	44.05	70.48	0.00	1.1
2018-11-22	1:59:00	43.51	71.60	8.50	1.5
2018-11-15	8:23:44	40.47	73.81	10.26	1.5
2018-11-09	4:12:13	47.59	70.19	15.55	2.7
2018-10-17	19:18:26	44.29	70.55	5.23	1.3
2018-10-15	0:49:48	43.27	71.64	5.14	1.0
2018-09-29	13:32:55	44.08	66.34	9.13	2.4
2018-09-22	6:35:58	43.66	72.36	9.51	1.4
2018-09-21	13:54:28	42.82	71.43	9.84	1.7
2018-09-02	22:06:35	44.28	71.02	3.10	1.9
2018-08-30	4:23:11	44.08	69.42	7.43	1.5
2018-08-27	2:24:15	44.23	72.35	0.16	0.9
2018-08-18	21:21:30	41.19	69.11	15.60	2.5
2018-08-06	8:52:14	44.90	75.15	13.44	0.9
2018-08-02	6:59:20	43.18	71.72	6.95	1.1
2018-07-29	20:09:08	45.07	74.71	7.01	1.6
2018-07-29	19:51:19	41.08	73.60	1.43	1.1
2018-07-23	15:17:34	41.09	73.82	2.37	1.6
2018-07-19	1:17:20	45.60	77.65	4.08	2.1
2018-07-16	17:43:55	43.19	70.71	5.00	2.1
2018-07-16	2:55:11	44.50	70.41	1.05	1.2
2018-07-14	6:53:22	41.47	72.65	1.10	1.1
2018-07-12	2:20:08	44.78	74.27	10.17	1.6
2018-07-11	3:32:14	41.72	71.79	2.62	1.1

2018-06-27	8:56:58	45.20	73.89	0.04	1.6
2018-06-27	6:37:25	43.25	71.66	14.46	0.9
2018-06-25	6:30:13	42.11	71.36	7.30	0.9
2018-06-20	16:15:10	45.76	74.45	5.73	2.8
2018-06-13	6:56:38	41.46	71.22	5.67	1.1
2018-06-04	3:04:52	43.97	70.45	10.02	1.4
2018-05-25	20:22:33	41.11	74.02	6.23	2.0
2018-05-23	17:50:10	41.65	74.64	0.00	1.8
2018-05-18	4:45:17	45.07	69.35	4.76	0.8
2018-05-06	1:08:53	44.27	69.45	5.00	1.3
2018-04-24	17:36:43	47.41	70.09	18.11	2.8
2018-04-22	21:35:51	46.92	66.63	12.22	2.3
2018-04-17	22:59:21	46.59	76.46	5.06	2.5
2018-04-07	3:25:19	41.68	71.36	4.64	0.9
2018-04-05	22:19:52	41.48	77.38	2.60	0.0
2018-04-03	16:09:07	43.53	71.53	5.50	1.4
2018-03-29	3:11:17	45.55	67.38	5.03	2.3
2018-03-21	4:59:13	44.75	74.63	0.02	2.7
2018-03-18	7:42:35	44.11	69.46	4.80	1.2
2018-03-14	22:19:51	45.52	66.57	0.92	2.9
2018-03-07	10:07:40	43.24	71.68	13.49	2.3
2018-02-27	11:06:23	41.34	73.01	8.23	1.3
2018-02-15	14:28:56	42.93	71.07	10.24	2.7
2018-02-15	1:34:25	45.07	70.91	12.30	1.6
2018-02-14	3:05:03	43.83	71.35	11.56	0.2
2018-02-13	23:44:22	43.47	71.57	5.79	2.0
2018-02-07	13:39:47	41.37	73.87	6.80	1.3
2018-02-07	11:15:43	41.36	73.87	4.10	1.3
2018-02-07	11:14:01	41.36	73.80	0.02	2.4
2018-02-02	5:45:49	46.20	65.87	12.66	2.4
2018-02-01	21:00:13	46.19	65.85	0.31	2.3
2018-01-29	22:04:08	46.38	75.41	4.89	2.4
2018-01-24	6:53:59	44.16	70.61	4.45	2.7
2018-01-24	6:05:46	43.82	71.02	10.29	0.4
2018-01-24	3:28:52	47.40	70.15	11.81	1.7
2018-01-19	6:24:35	44.60	69.68	0.49	0.7
2018-01-18	0:59:39	44.12	69.82	4.92	1.0
2018-01-18	0:47:40	44.15	69.80	1.25	1.7
2018-01-17	23:47:01	44.15	69.77	0.02	2.8
2018-01-04	15:42:27	46.87	70.82	11.88	3.0
2018-01-03	2:23:47	46.87	70.80	10.91	2.4

Table 6: The 96 earthquakes of magnitude greater or equal to M0.0 that occurred within the NEUSSEC and were recorded by one of more of the ALSA stations between January 2018 and July 2019. Data from Boston College's Weston Observatory.

YYYY-MM-DD	HH:MM:SS	Latitude (Degrees North)	Longitude (Degrees (West))	Depth (km)	Magnitude (M)
2019-06-26	5:23:51	8.46	-82.75	32.60	6.2
2019-06-26	2:18:07	56.18	164.09	10.00	6.3
2019-06-25	9:05:40	56.20	164.23	10.00	6.4
2019-06-22	8:50:24	39.22	-99.43	3.00	4.6
2019-06-18	13:22:19	38.64	139.48	12.00	6.4
2019-06-14	0:19:12	-30.06	-72.08	11.00	6.4
2019-05-30	9:03:32	13.20	-89.31	57.90	6.6
2019-05-26	7:41:15	-5.81	-75.27	122.60	8.0
2019-05-23	8:45:17	51.31	-178.24	30.00	6.0
2019-05-14	12:58:25	-4.05	152.60	10.00	7.6
2019-05-12	19:24:50	8.63	-82.83	19.00	6.0
2019-04-30	8:06:51	23.64	-63.08	10.00	4.6
2019-04-11	8:18:21	40.41	143.30	18.00	6.0
2019-04-09	18:08:46	44.70	-112.51	14.50	4.6
2019-04-02	21:35:30	52.17	178.07	8.00	6.4
2019-03-31	7:04:04	-1.95	-80.81	18.00	6.2
2019-03-28	22:06:49	50.50	159.94	9.00	6.2
2019-03-23	19:21:17	4.56	-76.22	122.00	6.1

2019-03-15	5:03:50	-17.87	-65.91	359.00	6.3
2019-03-01	8:50:42	-14.71	-70.16	267.00	7.0
2019-02-22	10:17:23	-2.19	-77.05	145.00	7.5
2019-02-14	19:57:04	35.43	-36.04	10.00	6.2
2019-02-01	16:14:12	14.68	-92.45	66.00	6.7
2019-01-20	1:32:52	-30.04	-71.38	63.00	6.7
2019-01-05	19:25:38	-8.14	-71.59	570.40	6.8
2018-12-31	2:35:37	54.43	-161.51	31.00	6.0
2018-12-24	12:41:19	55.34	164.51	10.00	6.1
2018-12-20	17:01:55	55.10	164.70	16.60	7.3
2018-12-19	1:37:40	-36.14	-101.07	10.00	6.3
2018-12-05	4:18:08	-21.95	169.43	10.00	7.5
2018-11-30	17:29:29	61.35	-149.96	46.70	7.1
2018-11-25	16:37:32	34.36	45.74	18.00	6.3
2018-11-25	3:40:50	13.18	-81.09	10.00	6.0
2018-11-14	21:21:50	55.64	161.99	49.00	6.1
2018-11-11	14:03:59	15.57	-49.87	10.00	6.3
2018-11-09	1:49:40	71.63	-11.24	10.00	6.7
2018-11-01	22:19:51	-19.58	-69.27	102.00	6.2
2018-10-28	22:23:53	13.04	-90.37	22.00	6.1
2018-10-25	22:54:52	37.52	20.56	14.00	6.8
2018-10-22	6:22:48	49.30	-129.72	10.00	6.5
2018-10-22	6:16:26	49.34	-129.29	10.00	6.8
2018-10-22	5:39:39	49.26	-129.41	10.00	6.5
2018-10-13	11:10:22	52.86	153.24	461.00	6.7
2018-10-10	23:16:02	49.29	156.30	20.00	6.5
2018-10-09	7:45:11	49.40	156.24	19.00	6.1
2018-10-07	20:00:18	20.04	-73.01	23.00	5.4
2018-10-07	0:11:51	20.03	-73.01	24.00	5.9
2018-09-28	10:02:45	-0.26	119.85	20.00	7.5
2018-09-07	2:12:06	-2.25	-78.79	110.50	6.2
2018-09-06	15:49:18	-18.47	179.35	670.80	7.9
2018-09-05	18:07:59	42.69	141.93	35.00	6.6
2018-08-25	22:13:25	34.61	46.24	10.00	6.0
2018-08-24	9:04:08	-11.04	-70.83	630.00	7.1
2018-08-23	3:35:12	51.35	-177.76	20.00	6.3
2018-08-22	19:47:19	52.45	-50.16	10.00	4.5
2018-08-22	9:31:45	43.56	-127.72	10.00	6.2
2018-08-21	21:31:47	10.77	-62.90	146.80	7.3
2018-08-19	0:19:40	-18.11	-178.15	600.00	8.2
2018-08-17	23:22:24	8.78	-83.15	15.00	6.1
2018-08-15	21:56:56	51.42	-178.03	33.90	6.5
2018-08-12	21:15:00	69.52	-144.34	16.20	6.0
2018-08-12	14:58:53	69.58	-145.29	15.80	6.4
2018-07-06	1:40:04	51.50	157.84	45.00	6.1
2018-05-09	10:41:45	36.99	71.38	116.00	6.2
2018-05-06	16:47:09	27.87	-88.68	10.00	4.6
2018-05-04	22:32:54	19.32	-155.00	5.80	6.9
2018-05-02	6:32:49	-24.27	-111.63	10.00	6.0
2018-04-10	10:19:34	-31.03	-71.53	66.00	6.2
2018-04-09	10:22:20	36.22	-97.57	4.90	4.6
2018-04-07	12:16:03	36.29	-97.52	5.80	4.6
2018-04-02	13:40:34	-20.66	-63.01	559.00	6.8
2018-02-25	17:44:44	-6.07	142.75	25.20	7.5
2018-02-16	23:39:39	16.39	-97.98	22.00	7.2
2018-01-31	7:07:00	36.53	70.85	193.70	6.2
2018-01-25	2:10:34	55.54	166.45	11.20	6.2
2018-01-24	10:51:19	41.10	142.43	31.00	6.3
2018-01-23	9:31:40	56.00	-149.17	14.10	7.9
2018-01-21	1:06:42	-18.88	-69.45	116.00	6.3
2018-01-19	16:17:44	26.69	-111.08	10.00	6.3
2018-01-14	9:18:45	-15.77	-74.71	39.00	7.1
2018-01-10	2:51:33	17.48	-83.52	19.00	7.5

Table 7: The 81 earthquakes of magnitude greater or equal to M4.6 that occurred outside the NEUSSEC and were recorded by one of more of the ALSA stations between January 2018 and July 2019. Data from Boston College's Weston Observatory.